



Benha University
Faculty of Engineering at Shoubra
Surveying Engineering Department

Accuracy Assessment and Enhancement of Rational Polynomial Coefficients of Satellite Imagery

A Thesis Submitted in Partial Fulfillment of the Requirements for the M.Sc.
Degree in Surveying Engineering (Photogrammetry and Remote Sensing)

Submitted By
Eng. Tamer Mohamed Ali Mohamed Saleh
Teaching Assistant at Shoubra Faculty of Engineering
B.Sc. in Surveying Engineering (2012)

Supervised By
Prof. Dr. Mohamed I. Zahran
Prof. of Surveying and Photogrammetry
Faculty of Engineering at Shoubra
Benha University

Dr. Ayman R. Al-Shehaby
Assoc. Prof. of Surveying
Faculty of Engineering at Shoubra
Benha University

Dr. Mahmoud Salah Gomaa
Assoc. Prof. of Surveying
Faculty of Engineering at Shoubra
Benha University

Cairo – Egypt
2018



Benha University
Faculty of Engineering at Shoubra
Surveying Engineering Department

APPROVAL SHEET

Accuracy Assessment and Enhancement of Rational Polynomial Coefficients of Satellite Imagery

Examiners Committee:

Prof. Dr. Mahmoud M. Hamed
Professor of Surveying & Photogrammetry,
Faculty of Engineering, Shoubra,
Benha University

Signature:

Prof. Dr. Ahmed M. Amin
Professor of Surveying & Photogrammetry,
Faculty of Engineering,
Suez Canal University

Signature:

Prof. Dr. Mohamed I. Zahran
Professor of Surveying & Photogrammetry,
Faculty of Engineering, Shoubra,
Benha University

Signature:

Assoc. Prof. Ayman R. Al-Shehaby
Assoc. Professor of Surveying,
Faculty of Engineering, Shoubra,
Benha University

Signature:

This research has been fully supported by the Surveying Engineering Department and data was made available courtesy of:

- Mr Elhadi Khalifa: IKONOS imagery.
- Department of Surveying Engineering: GeoEye-1 imagery.

The outcome of this research has been published and/or presented as below:

Journal publications:

- Saleh, T., Zahran, M.I., Al-Shehaby, A.R., and Gomaa, M.S. (2018) Performance enhancement of Rational Function Model (RFM) for improved geo-position accuracy of IKONOS stereo satellite imagery. Journal of Geomatics – ISG I Indian Society of Geomatics, Volume 12, No. 1 April 2018.

Disclaimer

This thesis describes work undertaken as part of a programme of study at the faculty of engineering for remote sensing and photogrammetry. All views and opinions expressed therein remain the sole responsibility of the author, and do not necessarily represent those of the college.

I hereby declare that all information in this document has been obtained and presented in accordance with academic rules and ethical conduct. I also declare that, as required, I have fully cited and referenced all material and results that are not original to this work.

The thesis is less than 14,200 words in length, exclusive of tables, figures, bibliographies and appendices (90 pages).

Name Lastname: Tamer Saleh

A handwritten signature in blue ink, appearing to read 'T. Saleh', with a stylized flourish at the end.

Signature:

To:

My parents;

My wife, Shimaa;

My son, Omar;

My brothers; and

Surveying Engineering Department

Acknowledgements

First of all, I would like to thank Allah, I would not be able to finish my study without his permission. All praise and glory to Almighty Allah who gave me courage and patience.

This thesis marks the end of a long and eventful journey for which there are many people whom I would like to acknowledge for their support along the way. Above all I would like to acknowledge the tremendous sacrifices that my parents made to ensure that I had an excellent education. For this and much more, I am forever in their debt. It is to them that I dedicate this dissertation.

I am deeply indebted to Prof. Dr. Mohamed I. Zahran my senior supervisor, for his direction and guidance on this research topic, for his excellent guidance, support, caring, patience, attention to details, and for his comments that improved the thesis and gave significance to the work. Whatever little has been done is because of his useful criticism and constructive suggestions from time to time. He has set an example I hope to match someday.

I am especially grateful to Assoc. Prof. Dr. Ayman R. Al-Shehaby for his support to the research topic at the early stage of the thesis and for his help at the material collecting stage. I would like to express my gratitude to my advisor, Assoc. Prof. Dr. Mahmoud Salah, for his excellent guidance, support, and caring.

Acknowledgements

A particular dept of gratitude to Prof. Dr. Abdel-Haleem M. Behairy for his continuous support and many invaluable numerous helpful suggestions.

And finally, thanks to my parents, wife, and all friends who endured this long process with me with their help, support, interest, valuable hints and encouraged me to work harder, always offering support and love.

Abstract

The physical and generic sensor models are two widely used imaging geometry models in photogrammetry and remote sensing. The physical sensor model requires the knowledge of sensor parameters that are often made unavailable due to various reasons. On the other hand, generic sensor models are expressed with a set of generic equations that describe the relationship between object space and image space. Utilizing the Rational Function Model (RFM) to replace physical sensor models in photogrammetric mapping is becoming a standard way for economical and fast mapping from high-resolution imagery. It is a general version of the polynomial model that can represent image to ground relationship and thus used as alternative solution for physical sensor model. Related Rational Polynomial Coefficients (RPCs), provided by the vendor, are calculated from the physical sensor model without the aid of ground control points. However, errors in sensor orientation parameters lead to biases in the RPCs mapping.

This thesis aims at evaluating the accuracy of RPCs provided with high-resolution satellite imagery and presents three mathematical models for performance enhancement of RFM utilizing ground control information, namely: 1) Bias-corrected image space; 2) Bias-corrected RPCs; and 3) Bias-corrected object space. The three models were compared with the well-known 3D-Affine and Direct Linear Transformation (DLT) models. The Least Squares Method (LSM) was applied to implement the different mathematical setups for estimating the correction parameters. In this thesis, the proposed methods were

applied with several setups on two different satellite stereo-pairs through a prototype software in a Matlab environment.

Attained results show that the accuracies of the three models are slightly variant for IKONOS-2. With five control points only, an accuracy of 0.8 m in X, 1.2 m in Y, and 1.3 m in height is achieved using the bias corrected image space, an accuracy of 0.9 m in X, 1.3 m in Y, and 1.5 m in height is reached using the bias corrected object space, and with the bias corrected RPCs, an accuracy of 0.9 m in X, 1.0 m in Y and 1.6 m in height is attainable. By increasing the number of control points sub-meter accuracy is attained. Regarding the GeoEye-1, it was observed that accuracy of less than a pixel can be achieved both in vertical and horizontal just by using 3 GCPs. On the other hand, the results indicate the effectiveness of 3D-Affine and DLT models especially when the RPCs and/or commercial software packages are not available for users.

Keywords: RFM, RPCs, Bias correction, 3D-Affine, DLT and Matlab.

Table of Contents

Preface.....	I
Disclaimer.....	II
Dedication.....	III
Acknowledgements	IV
Abstract.....	VI
Table of Contents.....	VIII
List of Tables.....	XII
List of Figures.....	XIV
List of Symbols, Acronyms and Nomenclature.....	XVI
 CHAPTER 1: INTRODUCTION.....	 1
1.1 Preamble.....	1
1.2 Problem Statement and Motivation.....	2
1.3 Research Objectives.....	3
1.4 Study Area and Dataset.....	4
1.5 Software Used.....	5
1.6 Scope of the Study.....	5
 CHAPTER 2: BACKGROUND AND MATHEMATICAL FORMULATION.....	 7
2.1 Introduction.....	8
2.1.1 Pixel Coordinate System.....	9
2.1.2 Image Coordinate System.....	9
2.1.3 Ground Coordinate System.....	10
2.1.4 Interior Orientation.....	11
2.1.5 Exterior Orientation.....	12
2.1.6 Photogrammetric Conditions.....	13
2.2 Geometric Distortion.....	14
2.2.1 Systematic Error.....	15
2.2.2 Non-Systematic Error.....	15
2.3 Geometric Correction Models.....	16
2.3.1 Physical Sensor Models (PSM)	17

2.3.1.1	Frame Cameras.....	18
2.3.1.2	Push-broom Sensors.....	19
2.3.2	Generalized Sensor Models (GSM).....	20
2.3.2.1	Rational Function Model (RFM)	21
2.3.2.2	Direct Linear Transformation (DLT) Model....	23
2.3.2.3	Projective Transformation Model (PTM)	24
2.3.2.4	Affine Model.....	25
2.4	RFM and RPCs Refinement Methods.....	26
2.4.1	Bias-Corrected Image Space.....	26
2.4.2	Bias-Corrected RPCs.....	28
2.4.3	Bias-Corrected Object Space.....	29
2.5	Literature Review.....	30
2.6	Summary.....	32
CHAPTER 3: METHODOLOGY FOR RFM MODIFICATION.....		34
3.1	Input Data Description.....	34
3.1.1	Characteristics of IKONOS.....	34
3.1.2	IKONOS Imagery Products.....	35
3.1.3	Characteristics of GeoEye-1.....	36
3.1.4	GeoEye-1 Imagery Products.....	36
3.2	Study Area.....	37
3.2.1	IKONOS-2 Data.....	37
3.2.2	GeoEye-1 Data.....	38
3.3	Strategy for RFM Modification.....	40
3.4	GCPs Collection.....	43
3.4.1	First Test Pair.....	43
3.4.2	Second Test Pair.....	46
3.5	Used Software.....	48
3.5.1	Digital Photogrammetric Software.....	48
3.5.2	Matlab Software Package.....	49
3.6	Rational Function Model.....	49
3.6.1	3D-Reconstruction using RFM.....	49
3.7	RFM and RPCs Refinement Methods.....	55
3.7.1	Bias-Corrected RPCs.....	55
3.7.1.1	Modelling with One Parameter.....	57

3.7.1.2	Modelling with Two Parameters.....	60
3.7.1.3	Modelling with Three Parameters.....	62
3.7.2	Bias-Corrected Image Space.....	63
3.7.3	Bias-Corrected Object Space.....	64
CHAPTER 4: RESULTS AND ANALYSIS.....		66
4.1	Performance Evaluation of RFM.....	66
4.1.1	Accuracy of IKONOS-2.....	66
4.1.2	Accuracy of GeoEye-1.....	68
4.2	Bias-Corrected RPCs.....	69
4.2.1	Modelling with One Parameter.....	69
4.2.1.1	Using IKONOS-2 Data.....	70
4.2.1.2	Using GeoEye-1 Data.....	71
4.2.2	Modelling with Two Parameters.....	72
4.2.2.1	Using IKONOS-2 Data.....	72
4.2.2.2	Using GeoEye-1 Data.....	73
4.2.3	Modelling with Three Parameters.....	73
4.2.3.1	Using IKONOS-2 Data.....	73
4.2.3.2	Using GeoEye-1 Data.....	74
4.2.4	Modelling with Four Parameters.....	75
4.2.4.1	Using IKONOS-2 Data.....	75
4.2.4.2	Using GeoEye-1 Data.....	76
4.3	Bias-Corrected Image Space.....	76
4.3.1	Using IKONOS-2 Data.....	76
4.3.2	Using GeoEye-1 Data.....	77
4.4	Bias-Corrected Object Space.....	78
4.4.1	Using IKONOS-2 Data.....	78
4.4.2	Using GeoEye-1 Data.....	79
4.5	3D-Affine Model.....	79
4.5.1	Using IKONOS-2 Data.....	80
4.5.2	Using GeoEye-1 Data.....	80
4.6	DLT Model.....	81
4.6.1	Using IKONOS-2 Data.....	81
4.6.2	Using GeoEye-1 Data.....	82
4.7	Analysis of the Results.....	82

CHAPTER 5: CONCLUSIONS AND RECOMMENDATIONS.....	87
5.1 Outline.....	87
5.2 Conclusions.....	88
REFERENCES.....	91
APPENDIX A: Basic Algorithm of Least-Squares Adjustment Method Used in the Research.....	96
A.1 Parametric Least-Squares Adjustment.....	96
A.1.1 Mathematical Model.....	96
A.1.2 Linearized Observation Equations.....	96
A.1.3 Normal Equations for the Solution Vector ΔX	96
A.1.4 Solution of the System of Normal Equations.....	97
A.1.5 Adjusted Values of the Unknown Parameters and Observations.....	97
A.1.6 Estimated Variance Factor.....	97
A.2 Combined Least-Squares Adjustment.....	97
A.2.1 Mathematical Model.....	97
A.2.2 Linearized form of the Model.....	98
A.2.3 Normal Equations for the Solution Vector ΔX	98
A.2.4 Solution of the System of Normal Equations.....	98
A.2.5 Adjusted Values of the Unknown Parameters and Observations.....	98
A.3 Calibration of DLT Model.....	98
APPENDIX B: Technical Information.....	101
B.1 GeoEye-1.....	101
B.1.1 Geo Imagery.....	101
B.1.2 Default Product Parameters.....	102
B.1.3 GeoEye-1 Parameters.....	103
B.2 IKONOS.....	104
B.2.1 IKONOS-2 Parameters.....	104
B.3 Detailed Descriptions of the Points.....	105
APPENDIX C: Mathematical Formulation of The Proposed Algorithm.....	107

List of Tables

Table (3-1) IKONOS Product Levels.....	36
Table (3-2) GeoEye-1 Product Levels.....	37
Table (3-3) Main Parameters of the Available IKONOS-2.....	38
Table (3-4) Specifications of the Available GeoEye-1.....	39
Table (3-5) GCPs with their 3D ground coordinates and 2D image coordinates over the study area of IKONOS-2 stereo-pair imagery.....	45
Table (3-6) Cairo GPS Fieldwork Information.....	46
Table (3-7) GCPs with their 3D ground coordinates and 2D image coordinates over the study area of GeoEye-1 stereo-pair imagery.....	48
Table (4-1) Object Coordinates of IKONOS-2.....	67
Table (4-2) RMS Value of ChkPs Using RPCs without GCPs for IKONOS-2...67	67
Table (4-3) Object Coordinates of GeoEye-1.....	68
Table (4-4) RMS Value of ChkPs Using RPCs without GCPs for GeoEye-1.....69	69
Table (4-5) RMS Value of ChkPs for IKONOS-2 Using One Parameter.....70	70
Table (4-6) RMS Value of ChkPs for GeoEye-1 Using One Parameter.....71	71
Table (4-7) RMS Value of ChkPs for IKONOS-2 Using Two Parameters.....72	72
Table (4-8) RMS Value of ChkPs for GeoEye-1 Using Two Parameters.....73	73
Table (4-9) RMS Value of ChkPs for IKONOS-2 Using Three Parameters...74	74
Table (4-10) RMS Value of ChkPs for GeoEye-1 Using Three Parameters...74	74
Table (4-11) RMS Value of ChkPs for IKONOS-2 Using Four Parameters...75	75
Table (4-12) RMS Value of ChkPs for GeoEye-1 Using Four Parameters.....76	76
Table (4-13) RMS Value of ChkPs for IKONOS-2 Using Bias-Corrected Image Space.....	77
Table (4-14) RMS Value of ChkPs for GeoEye-1 Using Bias-Corrected Image Space.....	77
Table (4-15) RMS Value of ChkPs for IKONOS-2 Using Bias-Corrected Object Space.....	78

Table (4-16) RMS Value of ChkPs for GeoEye-1 Using Bias-Corrected Object Space.....	79
Table (4-17) RMS Value of ChkPs for IKONOS-2 Using 3D-Affine Model.	80
Table (4-18) RMS Value of ChkPs for GeoEye-1 Using 3D-Affine Model...	81
Table (4-19) RMS Value of ChkPs for IKONOS-2 Using DLT Model.....	82
Table (4-20) RMS Value of ChkPs for GeoEye-1 Using DLT Model.....	82
Table (C-1) Results of the Positioning Accuracy Based on the Three Approaches with Two Bias Correction Models for the IKONOS-2 Case.....	111
Table (C-2) Results of the Positioning Accuracy Based on the Three Approaches with Two Bias Correction Models for the GeoEye-1 Case.....	112

List of Figures

Figure (2-1) Pixel Coordinates vs. Image Coordinates.....	9
Figure (2-2) Three-Dimensional System of Coordinates.....	10
Figure (2-3) Sensor Model to Reconstruct the Object Space Rays for (a) a Frame Camera and (b) a push-broom Linear Sensor.....	11
Figure (2-4) Exterior Orientation Elements.....	13
Figure (2-5) Imaging Geometry for a Single Point on a Frame Photograph...	14
Figure (2-6) Shows the Internal and External Distortions.....	16
Figure (3-1) IKONOS-2 Stereo-pair Imagery.....	38
Figure (3-2) GeoEye-1 Stereo-pair Imagery.....	40
Figure (3-3) The Strategy of Developing the RFM.....	42
Figure (3-4) An Example of the Selection of One GCP.....	44
Figure (3-5) GCPs and ChkPs Distribution Over the Study Area of IKONOS-2 Stereo-pair Imagery.....	44
Figure (3-6) Selection of One GCP Over the Study Area of GeoEye-1.....	47
Figure (3-7) GCPs Distribution Over the Study Area of GeoEye-1 Stereo-pair Imagery.....	47
Figure (3-8) Processing Steps of 3D-reconstruction Using Updated RPCs.....	60
Figure (4-1) Bias Errors of (a) Planimetry and (b) Elevation at 21 ChkPs Based on Vendor-supplied RPCs for IKONOS-2 Scenes.....	68
Figure (4-2) Bias Errors of (a) Planimetry and (b) Elevation at 12 ChkPs Based on Vendor-supplied RPCs for GeoEye-1 Scenes.....	69
Figure (4-3) Bias Errors of (a) Planimetry and (b) Elevation at ChkPs Using 3 GCPs and One Parameter for IKONOS-2 Imagery.....	71
Figure (4-4) Bias Errors of (a) Planimetry and (b) Elevation at ChkPs Using 3 GCPs and One Parameter for GeoEye-1 Imagery.....	71
Figure (4-5) Bias Errors in (a) Planimetry and (b) Elevation of ChkPs Using 5 GCPs and Two Parameters for IKONOS-2 Imagery.....	72

Figure (4-6) Bias Errors in (a) Planimetry and (b) Elevation of ChkPs Using 7 GCPs and Three Parameters for IKONOS-2 Imagery.....	74
Figure (4-7) Bias Errors in (a) Planimetry and (b) Elevation of ChkPs Using 9 GCPs and Four Parameters for IKONOS-2 Imagery.....	75
Figure (4-8) Planimetric and Vertical Accuracy of Object Coordinates of IKONOS-2 for RFM and RPCs Modification.....	83
Figure (4-9) Planimetric and Vertical Accuracy of Object Coordinates of GeoEye-1 for RFM and RPCs Modification.....	84
Figure (B-1) GeoEye-1 Satellite.....	101
Figure (B-2) Sample for Normalized RPCs of GeoEye-1 Imagery.....	103
Figure (B-3) IKONOS Satellite.....	104
Figure (B-4) Sample for Normalized RPCs of IKONOS-2 provided by the vendor.....	104

List of Symbols, Acronyms and Nomenclature

Most of the symbols used in this thesis are given in the following list. Where a symbol has only special localized meaning it is defined in the text and not included in this list.

2D	Two Dimensions
3D	Three Dimensions
ASTER	Advanced Spaceborne Thermal Emission and Reflection Radiometer
ChkPs	Check Points
CE90	Circular Error 90
DGPS	Differential Global Positioning Systems
DEM	Digital Elevation Model
DTM	Digital Terrain Model
DSM	Digital Surface Model
DLT	Direct Linear Transformation
EOE	Exterior Orientation Elements
FOV	Field Of View
GCPs	Ground Control Points
GIS	Geographic Information System
GPS	Global Positioning System
GSM	Generalized Sensor Models
HRSI	High-Resolution Satellite Imagery
IO	Interior Orientation
IPS	Imagine Photogrammetry Software
LPS	Leica Photogrammetry Suite
LSM	Least-Squares Method

List of Symbols, Acronyms and Nomenclature

LGO	Leica Geo-Office
LE90	Linear Error 90
MRSI	Multi Resolution Satellite Imagery
NMAS	National Map Accuracy Standard
OGC	Open Geospatial Consortium
PSM	Physical Sensor Models
PTM	Projective Transformation Model
RFM	Rational Function Model
RPCs	Rational Polynomial Coefficients
RMSE	Root Mean Square Error
RTK	Real Time Kinematic
SAR	Synthetic Aperture Radar
SRTM	Shuttle Radar Topography Mission
TBC	Trimble Business Center
TIFF	Tagged Image File Format
USA	United States of America
UTM	Universal Transverse Mercator
WGS84	World Geodetic System 1984 Model

Notations

A	Coefficient matrix of unknown parameters
B	Coefficient matrix of the observations
c-	Pixel column number
dd	Decimal degrees
f	Focal length
h	Ellipsoidal height
k	Scale factor

List of Symbols, Acronyms and Nomenclature

κ	Kappa rotation angle about Z-axis
K	Vector of known observations
Km	Kilometers
L	Left image
l	Line coordinates
ln	Normalized line coordinates
M	Rotation matrix
m	Meters
N	Number of points
N/A	Not Available
R	Right image
r-	Pixel row number
s	Sample coordinates
sn	Normalized sample coordinates
V	Vector of residual errors
X	Vector of unknown parameters
φ	Latitude
λ	Longitude
ω	Omega rotation angle about X-axis
ϕ	Phi rotation angle about Y-axis
ΔN	Numerator coefficient
ΔD	Denominator coefficient

CHAPTER 1

INTRODUCTION

1.1 Preamble

Sensor models are required to reconstitute the functional relationships between the image space and the ground space. They can be grouped into two classes, physical sensor models and generic sensor models. Physical sensor models are more rigorous and normally provide better accuracies since the model parameters employed represent the physical imaging process of sensors. However, building of a physical sensor model requires information of the physical sensor and its imaging geometry. It is realized that this information is not always available, especially for images from commercial satellites (e.g., IKONOS and GeoEye-1). The generic sensor models are independent on sensor platforms as well as sensor types. Such properties have made generic sensor models very popular in the remote sensing community. The typical generic sensor models are polynomial-based ones. Their capabilities have been widely tested and examined (Tao and Hu, 2000).

The Rational Function Model (RFM) is essentially a generic form of polynomial models. However, there are few studies that address its viability, accuracy and stability. Utilizing the RFM to replace physical sensor models in photogrammetric mapping is becoming a standard way for economical and fast mapping from high-resolution imagery. It

is a general version of the polynomial model that can represent image to ground relationship and thus used as alternative solution for physical sensor model. Related Rational Polynomial Coefficients (RPCs), provided by the vendor, are calculated from the physical sensor model without the aid of ground control points. However, errors in sensor orientation parameters lead to biases in the RPCs mapping (Singh et al., 2008).

This research aims at evaluating the accuracy of RPCs provided with high-resolution satellite imagery (80 per image) for the two high-resolution satellite sensors (IKONOS-2, GeoEye-1) and generating enhanced version of those coefficients utilizing ground control information.

1.2 Problem Statement and Motivation

RFM is becoming popular in today's world and is being used in a lot of photogrammetric applications such as creation of DEM, Orthophotos etc. Even the commercial digital photogrammetric software has also incorporated the RFM and related techniques. A number of photogrammetric systems such as ENVI, PCI Geomatica Ortho-Engine and ERDAS Imagine have incorporated RPCs. However, the RPCs provided by the vendors may not always represent the real imaging process well. This could be so due to various reasons such as the biases in the rigorous sensor model for generating RPCs, systematic errors or could also be marketing strategy from the image vendors, as they want to sell high precision products at relatively higher prices.

The RPCs may be modified using two general approaches, the direct approach or the indirect approach. The direct refining approach is used for updating the original RPCs themselves, but it uses more control points, while the indirect refining approach introduces complementary or concealed transformations in the image space or the object space and they do not change the original RPCs. Therefore, a model needs to be developed with which one can refine the existing RPCs values using few control points and mathematical modelling, which will enable the end users to get photogrammetry products with a higher geo-positional accuracy easily even without knowing the nuances of photogrammetric processing in detail.

1.3 Research Objectives

This research deals with the biases in the RPC mapping due to the errors in sensor orientation. The performance of bias-corrected image space, bias-corrected RPCs and bias-corrected object space will be further investigated with IKONOS-2 and GeoEye-1 stereo-pair imagery. The main objective is to find refined RFM and RPCs using least number of GCPs. The models described in this research were implemented through a prototype software developed by the author in a Matlab environment. In addition, 3D Affine and Direct Linear Transform (DLT) models are also applied and their accuracies are investigated for 3D positioning, compared with traditional and modified RFM.

In order to achieve the above objectives, the following key issues are included in this thesis:

- Data collection.
- GCPs collection.
- Image coordinates measurement.
- RPCs extraction.
- Mathematical model formulation.
- Least-squares adjustment of formulated mathematical models.
- RFM and RPCs modification.
- Accuracy evaluation.

1.4 Study Area and Dataset

To be able to fully evaluate the potential of RFM, two sets of IKONOS-2 and GeoEye-1 stereo-pair of high-resolution satellite imagery have been used, provided with related RPCs and metadata information. These datasets cover areas with different topographic features.

The first dataset is IKONOS-2 stereo pair of images, acquired of an area of Khartoum, *Sudan* about 16 km north of *Omdurman city* and belongs to a flat and moderately hilly terrain. The second dataset is the GeoEye-1 stereo pair of images covering the region of *Heliopolis* in the north-east of *Cairo*, which is an urban area. In addition, two sets of ground control and check points affixed and mapped by highly accurate GPS surveying.

1.5 Software Used

The software used in the research can be described as follows:

- IMAGINE photogrammetry software, namely LPS, for measuring the image coordinates of affixed control points in each of the two scenes of the test pair.
- Matlab software package, used for developing a prototype software utilizing least-squares adjustment to apply different developed models and to assess their accuracies.
- Microsoft Excel for statistical analysis.

1.6 Scope of the Study

The thesis comprises five chapters and is organized as follows:

Chapter 1 describes the problem statement, research objectives, study area, the data used and the software employed in RFM and RPCs modification using high-resolution satellite image data.

Chapter 2 presents background information and mathematical formulations related to the research. It also discusses the previous work that has been done in the related field.

Chapter 3 explains the proposed methods for the improvement of the RFM and RPCs. Tasks performed in this process are GCP collection, measurement of the image coordinates, 3D-reconstruction, bias-corrected RPCs, bias-corrected image space, and bias-corrected object space.

Chapter 4 discusses the results yielded by the proposed methods on image data available using different configurations of control points.

Chapter 5 presents conclusions related to the findings from the study and advises future work to extend the study.

The algorithm of least-squares method used in the research and calibration of DLT model are presented in Appendix (A). Appendix (B) describes the technical information of the image data used in this study. Finally, the mathematical formulation of the proposed algorithms is presented in Appendix (C).

CHAPTER 2

BACKGROUND AND MATHEMATICAL FORMULATION

With the availability of very high-resolution remote sensing satellites such as IKONOS and GeoEye-1, several researchers around the world have investigated the potential gain in large scale topographic map production, resource management, change detection, natural hazards monitoring, planning, 3D shoreline extraction, DTM and DSM generation from stereo images using different methods (Li, 1998; Toutin, 2001; Di et al., 2003; Poon et al., 2005; and Xu et al., 2005).

Spaceborne remote sensing data suffer from a variety of radiometric and geometric errors. These distortions would diminish the accuracy of the extracted information and thereby reduce the utility of the data, if the data is not precisely corrected (Nag and Kudrat, 1998). And here comes the major role of image processing techniques in correcting images from such errors and improving the quality of recorded images.

This chapter presents some photogrammetric basic, the sources of errors in satellite images, and the mathematical methods of corrections so as to get a final product of a corrected satellite image that can be used in a variety of applications. Finally, a review of relevant research is presented.

2.1 Introduction

Analytical photogrammetry is a term used to describe the physical mathematical calculation of coordinates of points in object space based upon camera parameters, measured image coordinates and GCPs. Generally, analytical photogrammetry involves the solution of large, complex systems of redundant equations by the method of least-squares adjustment. Analytical photogrammetry forms the basis of many modern hardware and software systems, including (analytical stereo-plotters, DTM generation, Ortho-photo production, rectification of digital image, and aero-triangulation, but also can be digital products, such as digital maps (Wolf and Dewitt, 2000).

Digital photogrammetry is sometimes called softcopy photogrammetry. The output products are in digital form, such as digital maps, DEMs, and digital Ortho-images saved on computer storage media. Therefore, they can be easily stored and managed by users. With the development of digital photogrammetry, photogrammetric techniques are more closely integrated into remote sensing and GIS. Conceptually, digital photogrammetry involves establishing the relationship between the camera or sensor used to capture the imagery, the imagery itself, and the ground. In order to understand and define this relationship, each of the all variables associated with the relationship must be defined with respect to image space and ground space (Leica Geosystems, 2006).

2.1.1 Pixel Coordinate System

The file coordinates of a digital image are defined in a pixel coordinate system, shown by c - and r - axes in the Figure (2-1). A pixel coordinate system is a coordinate system with its origin in the upper-left corner of the image, the c -axis pointing to the right, the r -axis pointing downward, and the units in pixels. These file coordinates (c , r) can also be thought of as the pixel column number and pixel row number, respectively (Leica Geosystems, 2006).

2.1.2 Image Coordinate System

An image coordinate system is defined as a 2D coordinate system existing on the image plane with its origin usually at the image center, shown by x - and y - axes in the Figure (2-1). On aerial photographs, the axes are determined by fiducial lines joining opposite fiducial marks. If the principal point does not coincide with the fiducial center, the system is shifted to bring its origin at that point. Image coordinates are used to describe positions on the photo plane. Image coordinate units are usually millimeters or microns (Wolf and Dewitt, 2000).

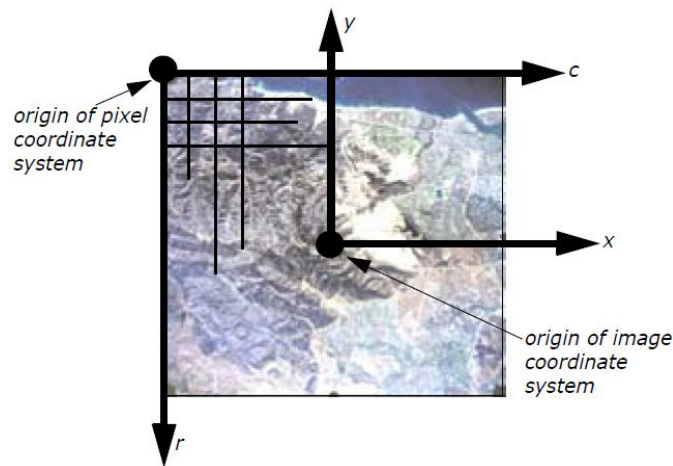


Figure (2-1) Pixel Coordinates vs. Image Coordinates (Leica Geosystems, 2006).

2.1.3 Ground Coordinate System

In addition to measurement of image coordinates, a certain number of control points in object space is required. Object space coordinates of these control points, which may be either image-identifiable features or exposure stations of the photographs themselves, are generally determined via some type of field survey technique such as GPS. The surveyor, geodesist, engineer, or cartographer who is the recipient of photogrammetrically compiled data or the supplier of control point coordinates may prefer to work in a longitude, latitude and height (λ , ϕ , h) system or in a map projection system (E , N , H), but these would have to be transformed into a rectangular coordinate system to serve as the object space coordinate system for photogrammetry. Figure (2-2) shows three mutually perpendicular axes intersecting in the origin point O . So, a point P can be defined in the 3D system of coordinates as (X_P, Y_P, Z_P) . Ground coordinates (X, Y, Z) are expressed in usually feet or meters. The Z value is elevation above M.S.L for a given vertical datum (Mikhail et al., 2001).

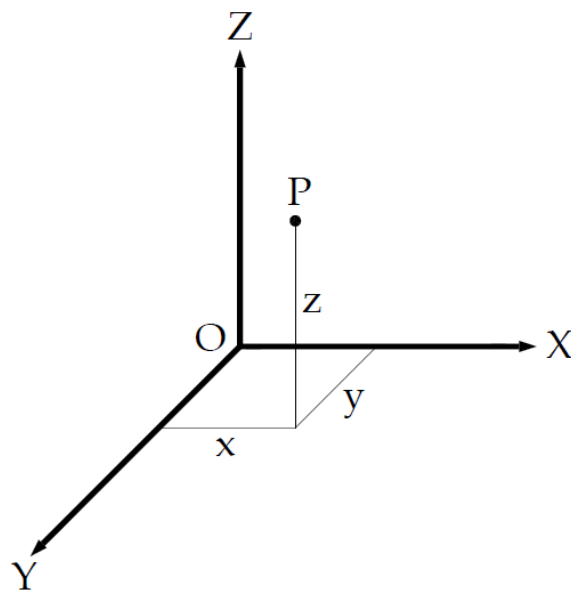


Figure (2-2) Three-Dimensional System of Coordinates (Mikhail et al., 2001).

2.1.4 Interior Orientation

The sensor model or (interior orientation), defines the internal geometry of a camera or sensor as it existed at the time of image capture. In a frame camera, these parameters would include the focal length (f) or principle distance, the location of the principle point in the image plane, and a description of the lens distortion at least. These elements are shown in Figure (2-3) for both a frame camera and a push-broom linear sensor. So, knowledge of the parameters of inner orientation allows correction of the raw image measurements for all known systematic errors or displacements, and, with a properly reconstructed bundle, the determination of valid imaging condition equations with the object point coordinates and the exterior orientation parameters (Mikhail et al., 2001).

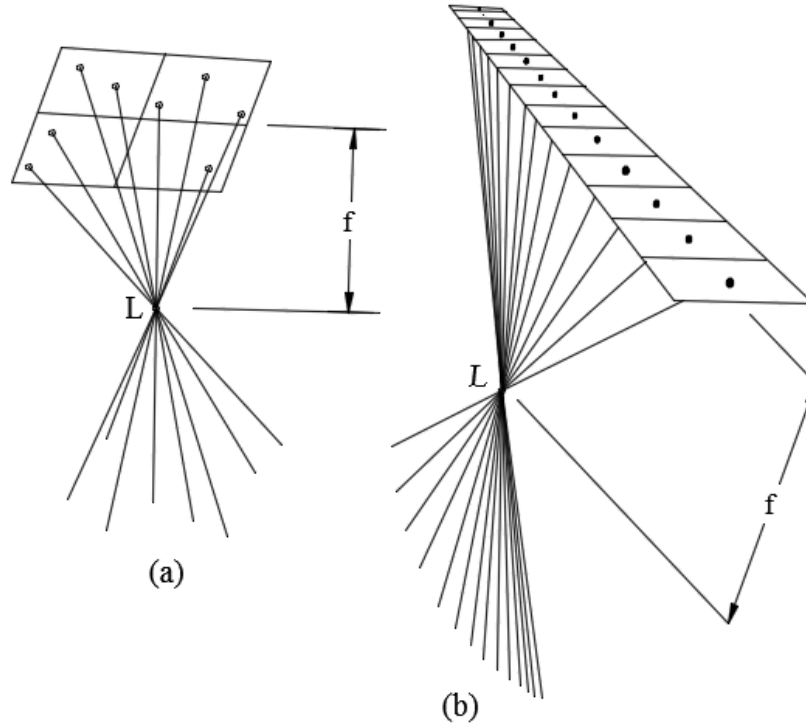


Figure (2-3) Sensor Model to Reconstruct the Object Space Rays for (a) a Frame Camera and (b) a Push-broom Linear Sensor (Mikhail et al., 2001).

2.1.5 Exterior Orientation

The sensor model, described above, establishes the bundle of rays from the image points. The platform model or (exterior orientation), establishes the position and orientation of the bundle of rays with respect to the object space coordinate system. Each bundle requires six independent elements (three for position and three for orientation). In the case of a frame camera, one bundle represents the entire image. On the other hand, each line defines a new bundle with its own six elements of exterior orientation in a linear sensor. Figure (2-4) shows the elements of exterior orientation. The exterior orientation defines the relationship between the object and image space coordinate system by the Equation (2-1) (Moffitt and Mikhail, 1980).

$$\begin{bmatrix} x \\ y \\ -f \end{bmatrix} = kM \begin{bmatrix} X - X_L \\ Y - Y_L \\ Z - Z_L \end{bmatrix} \quad (2-1)$$

Where $(x, y, -f)$ are the image space coordinates; k is a scale factor; M is a 3x3 matrix containing the rotation parameters; (X, Y, Z) represent the object space coordinate; and (X_L, Y_L, Z_L) are object space coordinates of the exposure station. The standard approach to constructing M is by using three sequential rotations: ω (Omega) rotation angle about X-axis, ϕ (Phi) rotation angle about Y-axis, and κ (Kappa) rotation angle about Z-axis. Figure (2-4) shown the individual angles $(\omega, \phi, \text{ and } \kappa)$ of exterior orientation.

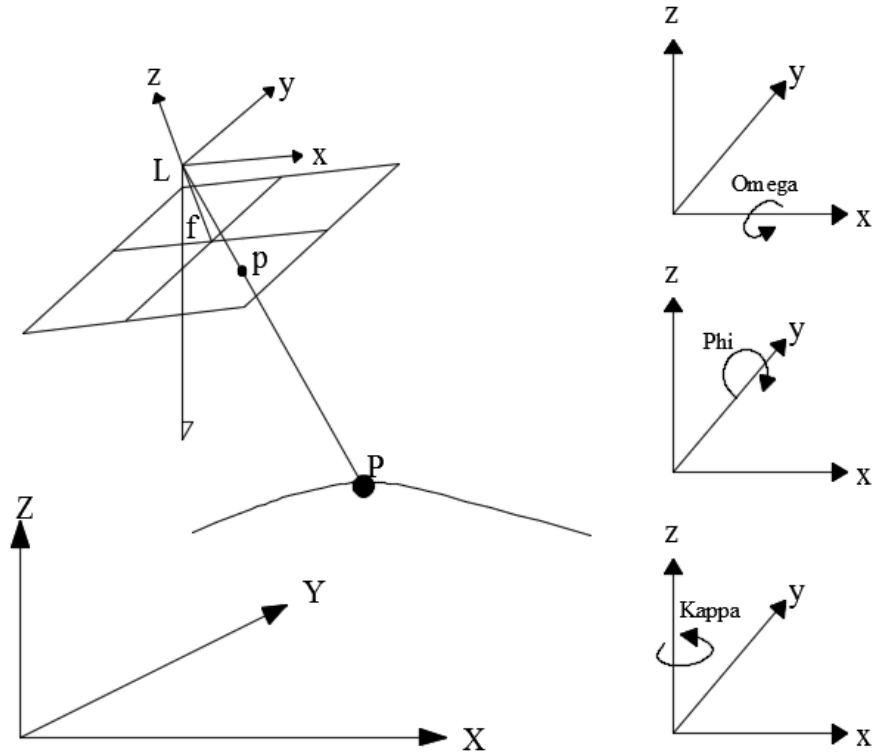


Figure (2-4) Exterior Orientation Elements (Moffitt and Mikhail, 1980).

2.1.6 Photogrammetric Conditions

The functional model of the imaging system will be realized in the condition equations, which relate image points, object points, and the imaging system parameters. A given condition equation may be used for different purposes, depending on which variables are considered observables, known, or unknowns in the stochastic model. Collinearity, is the condition that the camera/sensor, the ground, and the image all lie along a straight line in 3D space. Figure (2-5) shown the imaging geometry of a single point in a frame photograph (Mikhail et al., 2001).

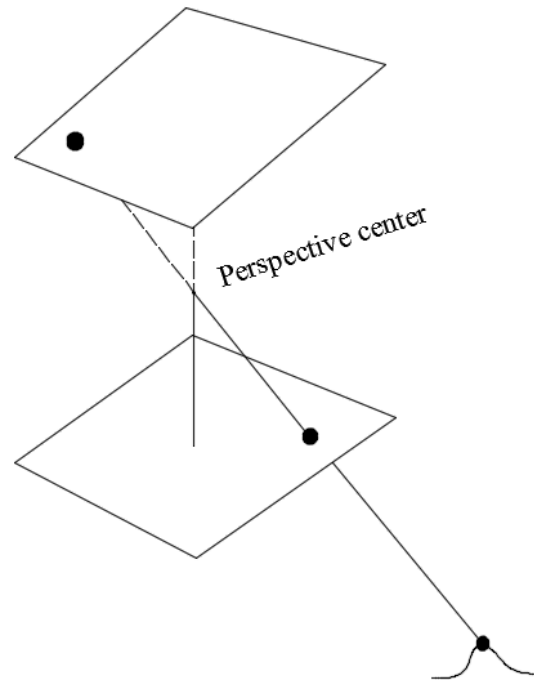


Figure (2-5) Imaging Geometry for a Single Point on a Frame Photograph (Mikhail et al., 2001).

2.2 Geometric Distortion

Geometric distortion is an error on an image, between the undeniable image coordinates and the supreme image coordinates which would be predicted theoretically with a supreme sensor and under supreme conditions. Satellite images are mostly contorted due to, Camera and Sensor orientation, Systematic error, Topographic relief displacement, Earth curvature, Motion of earth. Geometric distortions can be grouped into two broad categories: (1) internal distortion resulting from the geometry of the sensor; and (2) external distortions resulting from the attitude of the sensor or the form of the object (Devangi et al., 2016).

Geometric distortion may cause changes of scale over the image, irregularities in the angular relationships among the image elements,

displacement of objects in an image and occlusion of one image element by another. There are two types of geometric error occurrences, as described in the following subsections (Devi and Santosh, 2011).

2.2.1 Systematic Error

Systematic errors are due to image motion caused by Scan skew, mirror scans, panoramic distortions, variations in platform velocity and distortions due to the earth curvature (Khorram et al., 2012). Usually, these errors can be corrected at the satellite ground stations before distributing remotely sensed data to the public using information from platform ephemeris (information about the geometric characteristics of sensor and the earth at data acquisition) and knowledge of internal sensor distortion (Jaber, 2006).

2.2.2 Non-Systematic Error

Generally caused by variation through time in the position and attitude angles of the satellite platform. Without accurate sensor platform orientation parameters, these errors can only be corrected with the use of GCPs and a suitable precision photogrammetric or empirical model (Finkl, 2013). Figure (2-6) shows the various effects generated during image distortions.

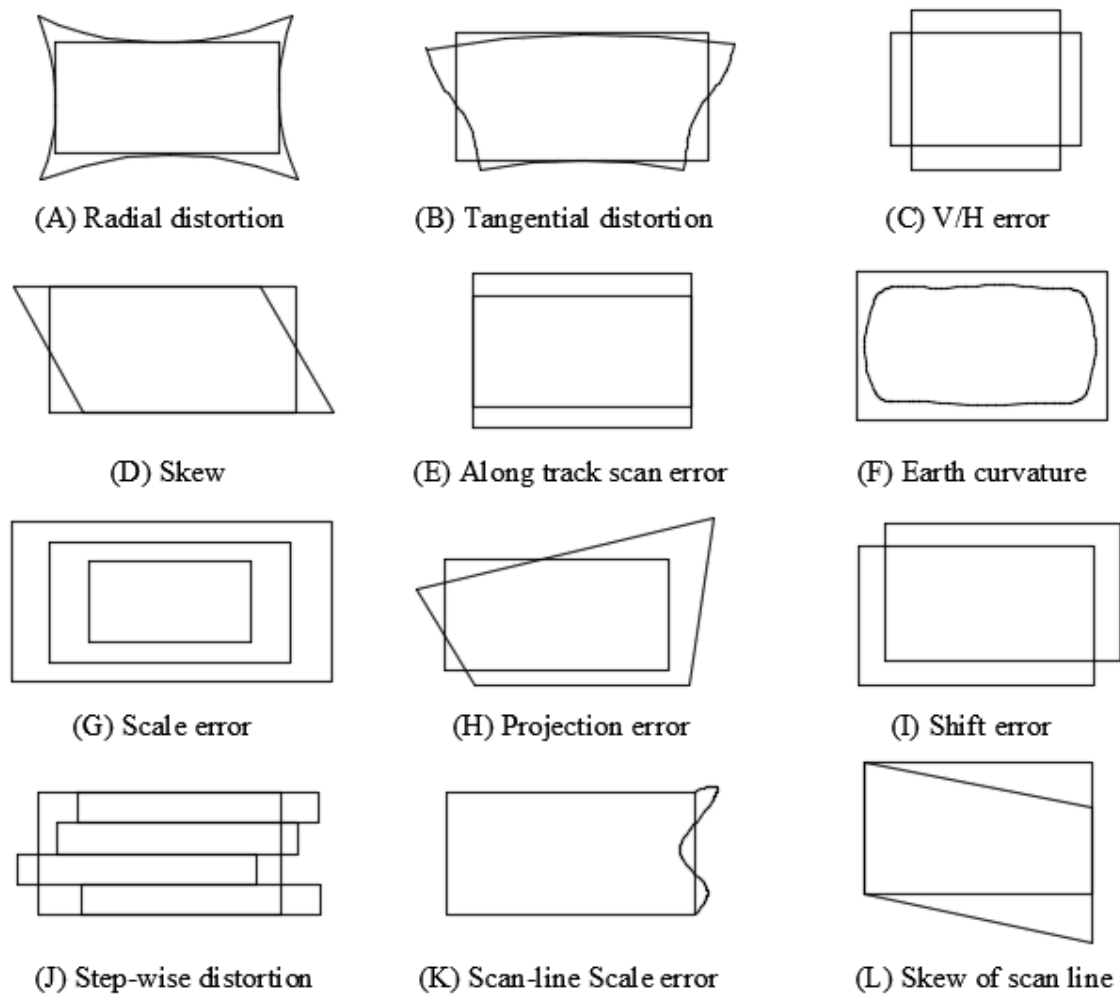


Figure (2-6) Shows the Internal and External Distortions (Dave et al., 2015).

2.3 Geometric Correction Models

Geometric corrections are made to correct the inconsistency between the location coordinates of the raw image data, and the actual location coordinates on the ground or base image. They are necessary to preprocess remotely sensed data and remove geometric distortion (Dave et al., 2015).

One of the primary barriers to a wider adaptation and utilization of satellite imagery is the sensor model being able to provide a high-level geometric correction through the image direction. Sensor models of satellite imagery are a key component to represent the functional relationships between the image space and the object space, and are essential for mono/stereo imagery orientation (Li et al., 2007). Sensor models are grouped with two classes, physical sensor models and generic sensor models (Tao and Hu, 2000). The choice of a sensor model depends primarily on the accuracy required, and the sensor and control information available (Tao and Hu, 2001).

2.3.1 Physical Sensor Models (PSM)

A physical (or exact) sensor model represents the physical imaging process. The elements involved describe the position and orientation of a sensor with respect to an object space coordinate system. Physical models fully reflect the geometry of viewing (Tao and Hu, 2001). Such models are based on platform-specific data, which are the satellite orbital elements, the attitude angles and the inner orientation elements of the sensor. The initial values, possibly provided as metadata file, must be refined by estimating their corrections using a suitable number of GCPs (Giannone, 2006). This method provides the most accurate and complete Geo-location data and has a great robustness over the full image with the use of only a few GCPs (Aguilar et al., 2007). One of the difficulties of physical models is their dependency to sensor.

In other words, these models change for different sensors. Because the number of different aerial and satellite sensors like frame camera,

push-broom scanner and their applications are increasing, it is necessary that existed software be changed for the analysis of their different data. Also, for using physical models it is necessary that imaging elements like orbital elements, satellite ephemeris, atmospheric refraction, earth curvature and lens distortion be known (Hosseini, 2008).

2.3.1.1 Frame Cameras

Physical models are based on collinearity condition equations that are adapted to frame acquisition technique which is used by all high-resolution satellites (Boccardo et al., 2004). In physical models, the object coordinates (X_A, Y_A, Z_A) , the image coordinates (x_a, y_a) of the GCPs and the inner orientation elements (x_o, y_o, f) are known. With the collinearity equations, the six Exterior Orientation Elements (EOE) $(X_S, Y_S, Z_S, \omega, \phi, k)$ can be calculated. Collinear equations are exact models available for frame images, it is described as (Tao and Hu, 2000).

$$\begin{aligned} x_a - x_o &= -f \left[\frac{m_{11}(X_A - X_s) + m_{12}(Y_A - Y_s) + m_{13}(Z_A - Z_s)}{m_{31}(X_A - X_s) + m_{32}(Y_A - Y_s) + m_{33}(Z_A - Z_s)} \right] \\ y_a - y_o &= -f \left[\frac{m_{21}(X_A - X_s) + m_{22}(Y_A - Y_s) + m_{23}(Z_A - Z_s)}{m_{31}(X_A - X_s) + m_{32}(Y_A - Y_s) + m_{33}(Z_A - Z_s)} \right] \end{aligned} \quad (2-2)$$

The inverse collinearity equations transform the image coordinates (x_a, y_a) and the height Z_A into the ground coordinates (X_A, Y_A) , i.e.

$$\begin{aligned} X_A - X_s &= (Z_A - Z_s) \left[\frac{m_{11}(x_a - x_0) + m_{21}(y_a - y_0) + m_{31}f}{m_{13}(x_a - x_0) + m_{23}(y_a - y_0) + m_{33}f} \right] \\ Y_A - Y_s &= (Z_A - Z_s) \left[\frac{m_{12}(x_a - x_0) + m_{22}(y_a - y_0) + m_{32}f}{m_{13}(x_a - x_0) + m_{23}(y_a - y_0) + m_{33}f} \right] \end{aligned} \quad (2-3)$$

These equations can be used for simple applications in their present form when quantities on the right are known and the quantities on the left are unknown. For instance, Equations (2-2) may be used when the inner and external elements are known and an object point is known in order to compute the corresponding image coordinates. Equations (2-3) may be used when the interior and exterior orientations are known and an image coordinate is known, along with one component of the object space point coordinate, in order to obtain the remaining two components of the object space point position (Yi and Jue, 2008).

For applications with more unknown variables to be solved for from a series of minimally sufficient or redundant observations, the nonlinearity of the equations forces us to use Taylor series approximation.

2.3.1.2 Push-broom Sensors

For a frame camera, one image has one set of EOE while, for linear array (line scanning) sensors such as the SPOT and IRS-1C imaging systems, each scan line has its own EOE. In this case a generic push-broom sensor model will be used, which still describes each scan line with collinearity equation, and the EOE will change with time in polynomial form. For line scanning sensors the mathematical model has to be modified to line-perspective geometry (Tao and Hu, 2001).

$$\begin{aligned}
 x_a^i &= -f \left[\frac{m_{11}^i (X_A - X_{si}) + m_{12}^i (Y_A - Y_{si}) + m_{13}^i (Z_A - Z_{si})}{m_{31}^i (X_A - X_{si}) + m_{32}^i (Y_A - Y_{si}) + m_{33}^i (Z_A - Z_{si})} \right] \\
 0 &= -f \left[\frac{m_{21}^i (X_A - X_{si}) + m_{22}^i (Y_A - Y_{si}) + m_{23}^i (Z_A - Z_{si})}{m_{31}^i (X_A - X_{si}) + m_{32}^i (Y_A - Y_{si}) + m_{33}^i (Z_A - Z_{si})} \right]
 \end{aligned} \tag{2-4}$$

Where x_a^i is the coordinate in scan-line i , orthogonal to the direction of travel and $x_o, y_o = 0$; i is the image number (which is directly related to the time of exposure; (X_{si}, Y_{si}, Z_{si}) are the spatial location of the exposure station of image i ; and $(m_{11}, m_{12}, m_{13}, \dots, m_{33})$ are the rotation matrix of image i .

2.3.2 Generalized Sensor Models (GSM)

These models are generic, i.e., their model parameters do not carry physical meanings of the imaging process. A GSM does not include sensor position and orientation information (Hu et al., 2004). Generally, it is not essential to know sensor's geometry for using generic models and it is possible to use them for different types of sensors (Hosseini, 2008). Although physical sensor models are more accurate, the development of GSM independent of sensor platforms and sensor types becomes attractive. In a GSM, the transformation between the image and the object space is represented as some general function without modeling the physical imaging process. The function can be of several different forms, such as polynomials or rational functions (Tao and Hu, 2001).

This class of models include RFM, DLT, and 3D-Affine transformation models etc. These kinds of models are further explained in the following subsections.

2.3.2.1 Rational Function Model (RFM)

The rational function model based on Rational Polynomial Coefficients (RPCs) is one of the generic models in use in place of physical models (Volpe and Rossi, 2003). Mathematically, the disadvantage of using polynomials for approximation is their tendency for oscillation. This often causes error bounds in polynomial approximation to significantly exceed the average approximation error. The RFM has better interpolation properties. It is typically smoother and can spread the approximation error more evenly between exact fit points. The RFM has the added advantage of permitting efficient approximation of functions that have infinite discontinuities near, but outside, the interval of fitting, while a polynomial approximation is generally unacceptable in this situation (Grodecki and Dial, 2003).

The RFM is independent of sensors and platforms. It also has coordinate system flexibility. It can accommodate object coordinates in any system such as geocentric, geographic, or any map projection coordinate system. With adequate control information, the RFM can achieve a very high fitting accuracy. This is the primary reason why the RFM has been used as a replacement sensor model (Tao and Hu, 2002).

The major drawbacks of the RFM are the necessity of a large number of GCPs (as they have to guarantee a sufficient redundancy), its high sensitivity to GCPs distribution, and its lack of reliability in the presence of outliers and the possibility of heavy distortions in areas distant from GCPs (Giannone, 2006). RFM performs transformations

between the image and object spaces through a ratio of two polynomials (Di et al., 2003).

The validation of this model has been tested in several researches with aerial photography data and satellite imageries (Tao and Hu, 2002). It takes the following general form (Di et al., 2003 and Hu et al., 2004):

$$l_n = \frac{P_1(X_n, Y_n, Z_n)}{P_2(X_n, Y_n, Z_n)} = \frac{\sum_{i=0}^{m_1} \sum_{j=0}^{m_2} \sum_{k=0}^{m_3} a_{ijk} X_n^i Y_n^j Z_n^k}{\sum_{i=0}^{n_1} \sum_{j=0}^{n_2} \sum_{k=0}^{n_3} b_{ijk} X_n^i Y_n^j Z_n^k}$$

$$s_n = \frac{P_3(X_n, Y_n, Z_n)}{P_4(X_n, Y_n, Z_n)} = \frac{\sum_{i=0}^{m_1} \sum_{j=0}^{m_2} \sum_{k=0}^{m_3} c_{ijk} X_n^i Y_n^j Z_n^k}{\sum_{i=0}^{n_1} \sum_{j=0}^{n_2} \sum_{k=0}^{n_3} d_{ijk} X_n^i Y_n^j Z_n^k} \quad (2-5)$$

Polynomial functions included in the model can be expressed as:

$$P_1(X_n, Y_n, Z_n) = a_0 + a_1 X_n + a_2 Y_n + a_3 Z_n + \dots + a_{19} Z_n^3$$

$$P_2(X_n, Y_n, Z_n) = b_0 + b_1 X_n + b_2 Y_n + b_3 Z_n + \dots + b_{19} Z_n^3$$

$$P_3(X_n, Y_n, Z_n) = c_0 + c_1 X_n + c_2 Y_n + c_3 Z_n + \dots + c_{19} Z_n^3$$

$$P_4(X_n, Y_n, Z_n) = d_0 + d_1 X_n + d_2 Y_n + d_3 Z_n + \dots + d_{19} Z_n^3 \quad (2-6)$$

Where l_n , and s_n are the normalized line and sample coordinates in the image space; X_n , Y_n , and Z_n are the normalized geodetic longitude, latitude and height in the object space; a_i , b_i , c_i and d_i are the polynomial coefficients RPCs (Total of 80); i , j and k are the increment values; m_1 , m_2 , m_3 , n_1 , n_2 , n_3 are the order of the polynomial model (0–3), where $i + j + k \leq 3$. The normalization of the coordinates is computed by (OGC, 1999):

$$l_n = \frac{\text{Line} - \text{Line_OFF}}{\text{Line_Scale}} ; s_n = \frac{\text{Sample} - \text{Sample_OFF}}{\text{Sample_Scale}}$$

$$X_n = \frac{\lambda - \text{Long_OFF}}{\text{Long_Scale}} ; Y_n = \frac{\varphi - \text{Lat_OFF}}{\text{Lat_Scale}} ; Z_n = \frac{h - \text{Height_OFF}}{\text{Height_Scale}} \quad (2-7)$$

Where Line and Sample are the image coordinates; Line_OFF and Sample_OFF are the offset values for the two image coordinates; Line_Scale and Sample_Scale are the scale factors for the two image coordinates; Similarly, φ , λ , and h are the geodetic latitude, longitude, and height in the object space; Lat_OFF, Long_OFF, and Height_OFF are the offset values for the three ground coordinates; Lat_Scale, Long_Scale, and Height_Scale are the corresponding scale factors.

Usually, the RFM is generated based on a physical sensor model. After a physical sensor bundle adjustment is performed, multiple evenly distributed image/object grid points can be generated and used as GCPs. Then, the RPCs are calculated by these GCPs (Xutong et al., 2004). A least-squares solution is used to estimate the RFM coefficients RPCs from a three-dimensional pseudo grid of points and orientation parameters. Since sensor orientation is directly observed, there would be some systematic error in orientation parameters. Thus, the refinement of RFM is required (Wu et al., 2008).

2.3.2.2 Direct Linear Transformation (DLT) Model

The DLT model was developed by Abdel Aziz and Karara (1971) for close range photogrammetry applications and can also be used for image rectification (Tao and Hu, 2000). The DLT represents a special

case of the RFM, with first degree polynomials and common denominators (Abdel-Aziz, 1982; Karara, 1985):

$$\begin{aligned} x &= \frac{L_1X + L_2Y + L_3Z + L_4}{L_9X + L_{10}Y + L_{11}Z + 1} \\ y &= \frac{L_5X + L_6Y + L_7Z + L_8}{L_9X + L_{10}Y + L_{11}Z + 1} \end{aligned} \quad (2-8)$$

Where x , y are the image coordinates; X , Y , Z are the ground coordinates; and L_1 , L_2 , L_3 , L_4 , L_5 , L_6 , L_7 , L_8 , L_9 , L_{10} and L_{11} are polynomial coefficients. Implementation of calibration and locate points of unknown position are provided in Appendix (A).

Variations of the DLT have been modified to incorporate corrections for self-calibration (Wang, 1999) and adapted to piece-wise functions (Yang, 2000). Both approaches have been tested in Multi Resolution Satellite Imagery (MRSI) with reasonable success. However, the DLT has not been used extensively as a sensor orientation model (camera or ephemeris data) for HRSI. The main reason is the requirement for a greater number of GCPs to obtain comparable geo-location accuracy as alternative methods, for example the affine model requires less GCPs but attains pixel level accuracy equivalent or better to that achieved using the DLT (Fraser et al., 2002). Thus, there are no compelling reasons in the use of the DLT with HRSI.

2.3.2.3 Projective Transformation Model (PTM)

The projective transform describes the relationship between two planes. It is defined by eight parameters, which can be derived from

four object points lying in a plane and their corresponding image coordinates (Novak, 1992).

$$\begin{aligned} x &= \frac{a_1x' + a_2y' + a_3}{c_1x' + c_2y' + 1} \\ y &= \frac{b_1x' - b_2y' - b_3}{c_1x' + c_2y' + 1} \end{aligned} \quad (2-9)$$

Where x, y are coordinates of the original image; x', y' are coordinates of the rectification; and $a_1, a_2, a_3, b_1, b_2, b_3, c_1, c_2$ are projective parameters. For the images of push-broom sensors the projective transformation can be modified as (Novak, 1992):

$$\begin{aligned} x &= \frac{a_1x' + a_2y' + a_3}{c_1x' + c_2y' + 1} \\ y &= b_1x' - b_2y' - b_3 \end{aligned} \quad (2-10)$$

where y is given in the flying direction and x represents the pixel in a scan line. Compared to (1), the elements of exterior and interior orientations are implicit in these parameters. Also, this method has little practical significance for satellite sensors, but could be applied for airborne line scanners (Tao and Hu, 2000).

2.3.2.4 Affine Model

Since 2D Polynomial models do not take into account the heights of the GCPs, these models can be efficiently used when the image is not influenced by the topographic effects. In this case, low order polynomials can provide accurate results. The model can be

represented as follow (Dare, 2004; Yamakawa and Fraser, 2004; El-Ashmawy et al., 2005):

$$\begin{aligned} x &= a_0 + a_1X + a_2Y \\ y &= b_0 + b_1X + b_2Y \end{aligned} \quad (2-11)$$

Where x , y are the image coordinates; X , Y are the 2D ground coordinates; and a_0 , a_1 , a_2 , b_0 , b_1 , b_2 are polynomial coefficients. Some studies have shown that the use of low-order polynomial 3D models for images of hilly and mountainous areas can reach the accuracy level that is close to the rigorous models (Fraser et al., 1999). A typical formula can be expressed as follow:

$$\begin{aligned} x &= a_0 + a_1X + a_2Y + a_3Z + a_4XY + a_5YZ + a_6XZ \\ y &= b_0 + b_1X + b_2Y + b_3Z + b_4XY + b_5YZ + b_6XZ \end{aligned} \quad (2-12)$$

Where X , Y , Z are the 3D ground coordinates.

2.4 RFM and RPCs Refinement Methods

The RPCs may be refined directly or indirectly. Direct refining methods calculate the RPCs and thus requires a large number (more than 39) of GCPs for the third order RFM, while indirect refining methods introduce complementary transformations in image or object space, and do not change the original RPCs directly (Hu et al., 2004). In this research, indirect method is adopted using three different approaches, as described in the following subsections.

2.4.1 Bias-Corrected Image Space

This bias correction method proposes a polynomial model defined in image space, in which Δl and Δs are added to the rational functions to

capture the differences between the nominal and the measured image space coordinates (Fraser and Hanley, 2003; Fraser and Hanley, 2005; Grodecki and Dial, 2003a). The following equations provide the form of the refined RFM using first order polynomials transformation (Hanley and Fraser, 2004):

$$\begin{aligned} l + \Delta l &= \frac{P_1(X_n, Y_n, Z_n)}{P_2(X_n, Y_n, Z_n)} * \text{Line_Scale} + \text{Line_OFF} \\ s + \Delta s &= \frac{P_3(X_n, Y_n, Z_n)}{P_4(X_n, Y_n, Z_n)} * \text{Sample_Scale} + \text{Sample_OFF} \end{aligned} \quad (2-13)$$

Where l and s are line and sample coordinates; Δl and Δs represent the differences between the measured and the calculated line and sample coordinates, which can be generally described as polynomials of the image line and sample coordinates as follows (Grodecki and Dial, 2003a; Gong and Fritsch, 2016):

$$\begin{aligned} \Delta l &= A_0 + A_1 l + A_2 s + A_3 l^2 + A_4 l.s + A_5 s^2 + \dots \\ \Delta s &= B_0 + B_1 l + B_2 s + B_3 l^2 + B_4 l.s + B_5 s^2 + \dots \end{aligned} \quad (2-14)$$

Where A_i and B_i ($i = 1, 2, 3, \dots$) are the correction parameters. By using affine transformation, sub-pixel accuracy can be obtained (Fraser and Hanley, 2003). However, the method is effective only when the camera FOV is narrow and the position and attitude errors are small (Grodecki and Dial, 2003).

The affine parameters in Equations (2-14) can be resolved based on the control points using the Least-Squares Method (LSM). If the shift bias [A_0 and B_0] are the only factors taken into account, the correction can be made by improving the original RPCs. As detailed in (Fraser

and Hanley, 2005), only the parameters in numerator need to be updated, and the refined RPC model becomes:

$$l_n = \frac{(a_0 - b_0 \Delta l_n) + (a_1 - b_1 \Delta l_n) X_n + \dots + (a_{19} - b_{19} \Delta l_n) Z_n^3}{b_0 + b_1 X_n + b_2 Y_n + b_3 Z_n + \dots + b_{19} Z_n^3}$$

$$s_n = \frac{(c_0 - d_0 \Delta s_n) + (c_1 - d_1 \Delta s_n) X_n + \dots + (c_{19} - d_{19} \Delta s_n) Z_n^3}{d_0 + d_1 X_n + d_2 Y_n + d_3 Z_n + \dots + d_{19} Z_n^3} \quad (2-15)$$

Where a_i , b_i , c_i , and d_i are the original vendor-provided RPCs; Δl_n and Δs_n are the normalized values of the image shift bias parameters.

Effectively, all original terms in the numerator of each expression in Equations (2-5) are modified; each coefficient a_i is replaced by $(a_i - b_i \Delta l_n)$.

2.4.2 Bias-Corrected RPCs

This approach is implemented by adding a set of new adjustable functions ΔN (numerator coefficient) and ΔD (denominator coefficient) for both line and sample equations based on the known GCPs to correct the RPCs (Singh et al., 2008). The new adjustable functions can be defined as follows:

$$l_n = \frac{P_1 (X_n, Y_n, Z_n) + \Delta P_1}{P_2 (X_n, Y_n, Z_n) + \Delta P_2}$$

$$s_n = \frac{P_3 (X_n, Y_n, Z_n) + \Delta P_3}{P_4 (X_n, Y_n, Z_n) + \Delta P_4} \quad (2-16)$$

Where ΔP_1 , ΔP_2 , ΔP_3 , and ΔP_4 are the differences between the original and the adjustable, which can be generally described as (Singh et al., 2008):

$$\begin{aligned}
\Delta P_1 &= A_0 + A_1 X_n + A_2 Y_n + A_3 Z_n + \dots + A_{19} Z_n^3 \\
\Delta P_2 &= B_0 + B_1 X_n + B_2 Y_n + B_3 Z_n + \dots + B_{19} Z_n^3 \\
\Delta P_3 &= C_0 + C_1 X_n + C_2 Y_n + C_3 Z_n + \dots + C_{19} Z_n^3 \\
\Delta P_4 &= D_0 + D_1 X_n + D_2 Y_n + D_3 Z_n + \dots + D_{19} Z_n^3
\end{aligned} \tag{2-17}$$

A_i , B_i , C_i and D_i are the correction parameters in the correction model. The resulted estimates of correction parameters are added to the original coefficients to get refined RPCs. Chapters 3 and 4 will give the details on the methodology used and its implementation.

2.4.3 Bias-Corrected Object Space

A polynomial model defined in the domain of object space to correct the ground coordinates derived from the vendor-provided RPCs as in Equations (2-18) (Di et al., 2003; Xiong and Zhang, 2009). In this method, the polynomial correction parameters are determined by the GCPs as follows:

$$\begin{aligned}
X^{GPS} &= a_0 + a_1 X^{RF} + a_2 Y^{RF} + a_3 Z^{RF} \\
Y^{GPS} &= b_0 + b_1 X^{RF} + b_2 Y^{RF} + b_3 Z^{RF} \\
Z^{GPS} &= c_0 + c_1 X^{RF} + c_2 Y^{RF} + c_3 Z^{RF}
\end{aligned} \tag{2-18}$$

Where X^{GPS} , Y^{GPS} , Z^{GPS} are the observed ground coordinates; X^{RF} , Y^{RF} , Z^{RF} are the ground coordinates derived from the RPCs; and a_i , b_i , c_i are the correction parameters.

2.5 Literature Review

The physical sensor model and the rational function model are the two main sensor models to describe the geometrical relationships between image points and their corresponding ground points (Fraser et al., 1999; Tao and Hu, 2001; Grodecki and Dial, 2003). However, the (PSMs) for commercial satellite imagery may not be computationally efficient due to their complexity, also may not even be available to general users (Habib et al., 2007). Instead, the (RFMs) are provided by the image vendors. RFMs have served as alternative sensor models and have been widely used to derive 3D spatial information from various types of satellite images (Fraser et al., 2006).

Traditional methods to improve the geo-positioning accuracy of satellite images simply use GCPs to compensate the bias in RPCs through mathematical functions.

In 2003, Fraser and Hanley developed a method for the removal of exterior orientation biases in RPCs of IKONOS imagery. According to the performed experimentation it was found that only bias corrected RPCs of IKONOS is capable of generating high accuracies and with just one good ground control point.

In their research, Di et al. (2003) conducted experiments on aerial and satellite imagery. They stated that the rational function coefficients are scene specific because IO and EO parameters are merged together and they use the control points.

Fraser and Hanley (2005) recognized the notable positioning accuracy attained with the RPC bundle adjustment with bias compensation. Furthermore, Fraser et al. (2006) gave an overview of the RPC model for high resolution satellite imagery, tried to highlight the practicability and accuracy potential of RPC block adjustment. It has been demonstrated that bias compensated RPC block adjustment can yield sub-pixel positioning accuracy and highly accurate orthoimages and digital surface models.

Tong et al. (2010), which presented the two schemes: RPCs modification; and RPCs regeneration for orientation bias correction based on Quick-Bird stereo images in Shanghai. Four cases of bias correction were tested including: shift bias correction, shift and drift bias correction, affine model bias correction, and second-order polynomial bias correction. A least-squares adjustment method is adopted for correction parameter estimation. The modified RPCs improved the accuracy from 23 m to 3 m in planimetry and from 17 m to 4 m in height. With the shift and drift bias correction method, the regenerated RPCs achieved a further improved positioning accuracy of 0.6 m in planimetry and 1 m in height with minimal two GCPs.

Zhang et al. (2011) studied comprehensively the feasibility and methodology of rational function modeling for Spaceborne SAR datasets, and possible applications of SAR RFM are discussed briefly. The RFM are successfully applied to Spaceborne SAR datasets of different processing levels acquired by various SAR satellites.

Kumar (2006) first analyzed the DEM generated from the CARTOSAT-1 stereo image over Dehradun and says that while using only RPC information for CARTOSAT –1 stereo data, the error in height was in the range 100 to 200 m. While using eight GCP's for CARTOSAT –1 stereo data, the error was reduced to 2 to 13 m. It was found that accuracy of contours generated from CARTOSAT –1 stereo data was very accurate and close to ground height.

Chen et al. (2006) in this investigation, he provides a least squares collocation procedure for the RSM and RFM. The study compares the RSM and RFM error of the RFM. Experiment was conducted on FORMOSAT-2 satellite images and results indicate that the RSM performs just slightly better than the RFM in this study. For a standard scene, the model error between the physical sensor model and the rational function model is 0.01 pixels. For a strip with 15 scenes, the model error increases to 0.15 pixels.

2.6 Summary

In most studies mentioned above, biases in the image space or in the object space were modelled and corrected to refine RPCs-derived ground coordinates, while the original RPCs remained unchanged. Few studies were conducted to take the original set of coefficients from the RPC model and add new adjustable functions for both line and sample to the normal equations based on the known GCPs (Singh et al., 2008). For IKONOS stereo images, the sensor physical parameters are derived from the satellite ephemeris and attitude data

without using GCPs. The satellite ephemeris data are determined using on-board GPS receivers and sophisticated ground processing of the GPS data. The satellite attitude is determined by optimally combining star tracker data with measurements taken by the on-board gyros. Since the IKONOS satellite imagery vendor, Space Imaging Company, has not released the satellite ephemeris data, no physical mathematical model can be established. This causes a major problem in the process of geo-positioning from IKONOS stereo imagery with high precision. Therefore, some generalized generic mathematical models are needed to substitute the physical models for IKONOS imagery restitution (Hu et al., 2004).

CHAPTER 3

METHODOLOGY FOR RFM MODIFICATION

This chapter describes the methodology used in steps of the RFM modification of IKONOS-2 and GeoEye-1 stereo-pair imagery. Sections 3.1 and 3.2 describe the specifications of satellite image data and nature of study area used in this thesis. Section 3.3 describes the methodology for RFM enhancement from stereo-pair imagery. GCP collection, software used, 3D-reconstruction computation, bias-corrected RPCs, bias-corrected image space, and bias-corrected object space are detailed in Sections 3.4 to 3.7.

3.1 Input Data Description

For this work, two satellite datasets of IKONOS-2 and GeoEye-1 were used. The following subsections present a brief overview of these datasets as well as some of the associated metadata.

3.1.1 Characteristics of IKONOS

The IKONOS satellite is the world's first commercial satellite to collect panchromatic images with 1 m resolution and multispectral imagery with 4 m resolution. Imagery from the panchromatic and multispectral sensors can be merged to create 1 m color imagery (pan-sharpened), providing the commercial and scientific communities with a dramatic improvement in spatial resolution over previously available remote sensing satellites (e.g., Landsat, SPOT, IRS, and MOMS) (Grodecki and Dial, 2003).

IKONOS imagery is being used for national security, military mapping, air and marine transportation, and by regional and local governments. The IKONOS satellite sensor was successfully launched as the first commercially available high-resolution satellite sensor on September 24, 1999 at Vandenberg Air Force Base, California, USA. From a 682-km-high synchronous orbit, orbit that is inclined 98.10 to the equator and with an equatorial crossing time of 10:30 A.M, IKONOS has a revisit time of once every three days for panchromatic data and downlinks directly to more than a dozen ground stations around the globe (www.spaceimaging.com).

3.1.2 IKONOS Imagery Products

There are a number of IKONOS image products with several processing levels containing the Geo, Reference, Map, Pro, Precision, and Precision Plus products that have corresponding absolute positioning accuracy (RMSE) of 25.3, 11.8, 5.7, 4.8, 1.9, and 0.9 m, respectively. The 1 m panchromatic resolution IKONOS stereo-pair imagery is offered by Space Imaging, Inc. (hereinafter called the vendor) to commercial users only as Reference Stereo and Precision Stereo products. They are distributed in an 8 or 11bit Geo-Tiff and NITF 2.0 format with a text metadata file (RPCs of the RFM, source image descriptions and products are included in the metadata file). Table (3-1) shows the description of the different levels of IKONOS products (Gerlach, 2000).

Table (3-1) IKONOS Product Levels (Xu et al., 2004)

Product	Positional Accuracy (m)		NMAAS	Stereo option
	CE90	RMSE		
Geo	50.0	25.3	1:100000	No
Reference	25.4	11.8	1:50000	Yes (RPC*)
Map	12.2	5.70	1:24000	No (RPC*)
Pro	10.2	4.80	1:12000	No
Precision	4.10	1.90	1:4800	Yes (RPC*)
Precision Plus	2.00	0.90	1:2400	No

* Provides RPC with imagery

3.1.3 Characteristics of GeoEye-1

GeoEye-1, the world's highest-resolution commercial color imaging satellite, was launched on September 6, 2008 from Vandenberg Air Force Base in California. The satellite offers extraordinary detail, high accuracy and enhanced stereo for DEM generation. GeoEye-1 will simultaneously collect Panchromatic imagery at 0.41 m and Multispectral imagery at 1.65 m. Due to U.S. Government Licensing, the imagery will be made available commercially as 0.50 m imagery. GeoEye-1 orbits the Earth every 98 minutes at an altitude of approximately 681 kilometers. The satellite travels a sun-synchronous orbit, passing the equator at about 10:30 A.M local time, it also features a revisit time of less than three days (www.digitalglobe.com).

3.1.4 GeoEye-1 Imagery Products

GeoEye's imagery product line consists of three core product offerings: Geo, Geo-professional, and Geo-stereo. Geo products are low cost, geometrically corrected images. Geo-professional products are orthorectified (terrain corrected) to specified map accuracy. Geo-stereo products provide stereo imagery for 3-dimensional viewing and feature extraction. All products are available in pansharpened color in

either 0.50 m and 1 m resolution. Table (3-2) shows the description of the different levels of GeoEye-1 products (GeoEye, 2009). For more information about GeoEye-1 imagery products are shown in Appendix (B).

Table (3-2) GeoEye-1 Product Levels (GeoEye, 2009)

0.5 m Resolution				
Product	Positional Accuracy (m)		NMAAS	Stereo Option
	CE90	RMSE		
Geo	5.0	3.0	N/A	Yes (RPC*)
Geo-professional	10	5.0	1:12000	No (RPC*)
Geo-stereo	4.0	2.0	1:5000	Yes (RPC*)
1 m Resolution				
Geo	15	8.0	N/A	Yes (RPC*)
Geo-professional	10	5.0	1:12000	No (RPC*)
Geo-stereo	15	8.0	1:20000	Yes (RPC*)

* Provides RPC with imagery

3.2 Study Area

3.2.1 IKONOS-2 Data

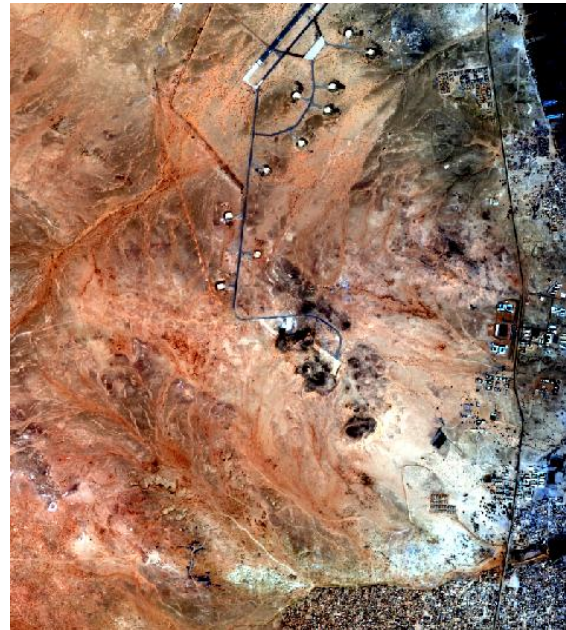
It consists of a pan-sharpened stereo pair of IKONOS-2 imagery, covering an area in the *north of Khartoum in Sudan* about 16 km north of Omdurman city. The study area covers almost 6.115 km x 5.272 km. It includes various topographic features, moderately terrain and a part of *Wadi Sayidna Air Base* as shown in Figure (3-1). It was the first stereo-pair of IKONOS-2 images acquired over Sudan in December 27, 2003. The data are delivered in Geo-Tiff format with text files containing the RPCs for each image. The metadata associated with this dataset is provided in Table (3-3).

Table (3-3) Main Parameters of the Available IKONOS-2

Acquisition Date	27-12-2003
Time	08:41 GMT 27-12-2003 and 08:42 GMT
Sun Angle Azimuth	156.1241 and 156.3809 degrees
Sun Angle Elevation	47.42863 and 47.50945 degrees
Overlap	99%
Rows	5893 and 6004 pixels
Columns	5351 and 5357 pixels
Pixel Size X, Y	1.00 m * 1.00 m
Percent Cloud Cover	0
Size	6.115 Km * 5.272 Km
Area	32.31 Square Kilometers
Product Line	Reference Stereo



(a) Left Scene



(b) Right Scene

Figure (3-1) IKONOS-2 Stereo-pair Imagery (Edge Pro).

3.2.2 GeoEye-1 Data

The second acquired data are stereo GeoEye-1 panchromatic satellite images, with 0.5 m resolution, covering the area of study in the north-east part of *Cairo* that contains different ground features such as the

Ring Road and the *Autostrad*, urban area of *Heliopolis*, *Almaza Air Force Base Airport* and variety of topography as shown in Figure (3-2). It was the first stereo pair of GeoEye-1 images acquired over Egypt in November 21, 2013, as was shown in the satellite company archive at that time. The image is supplied in a product level Geo-Stereo and standard product type. This image is Geometrically Corrected by the producer before publishing, which is the least processed stereo images available by the satellite company (Space Imaging), and supplied in Geo-Tiff format with text files containing the RPCs for each image. These RPCs are important for rectifying GeoEye-1 satellite images using RFM instead of the rigorous models that require the ephemeris data of the satellite orbit, which have not been released yet by the satellite company. The specifications of these scenes are listed in Table (3-4).

Table (3-4) Specifications of the Available GeoEye-1

Acquisition Date	21-11-2013
Time	08:50 GMT 27-12-2003 and 08:51 GMT
Sun Angle Azimuth	165.1035 and 165.3520 degrees
Sun Angle Elevation	38.50654 and 38.55277 degrees
Overlap	99%
Rows	29848 and 29848 pixels
Columns	16628 and 16628 pixels
Pixel Size X, Y	0.5 m * 0.5 m
Percent Cloud Cover	0
Size (km)	14.702 Km * 7.642 Km
Area	113.7 Square Kilometers
Product Line	Geo-Stereo

The parameter meanings of IKONOS-2 and GeoEye-1 stereo-pair imagery provided by the vendor in the format of “image_name_rpc.txt” are described in Appendix (B).

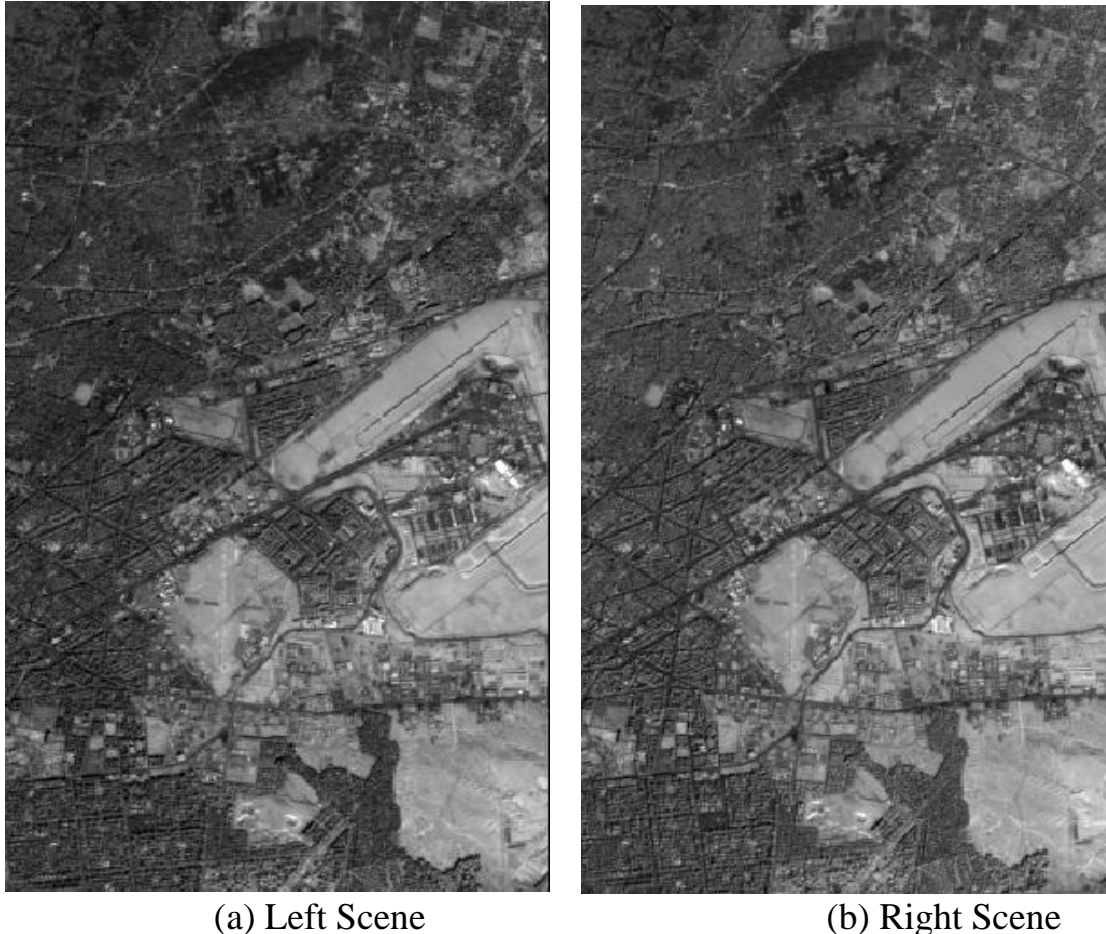


Figure (3-2) GeoEye-1 Stereo-pair Imagery (Edge Pro).

3.3 Strategy for RFM Modification

As mentioned earlier, the vendor does not provide the physical sensor model together with IKONOS-2 and GeoEye-1 image data. This causes a major problem in the process of geo-positioning with high precision. The methodology used focuses on achieving the main objective of the study, i.e. mathematical model is required to find the best set of parameters with least number of GCPs for refining the

RPCs provided by the vendors, which consist of, shown in Figure (3-3).

- (1) Affixing a set of distinct ground control and check points in the overlap area of the test image pair. The coordinates of those points are determined precisely, e.g. by using a static GPS positioning technique.
- (2) Measuring the image coordinates of affixed control points in each of the two images of the test pair.
- (3) Extracting RPCs provided with the metadata files associated with the test image pair.
- (4) Performing least-squares adjustment involving the provided RPCs and measured image coordinates of control points based on RFM as a mathematical model to get estimated coordinates of the control points.
- (5) Assessing the accuracy of provided RPCs by computing the differences between measured and estimated coordinates of control points.
- (6) Modelling biases in provided RPCs by modifying the traditional RFM to include additional parameters, using different control configurations.
- (7) Resolving the modified versions of RFM using least-squares method to get modelled parameters associated with each version.
- (8) Assessing the accuracy of modified RFM by computing the differences among measured values of check points and their corresponding values estimated by the modified RFM.

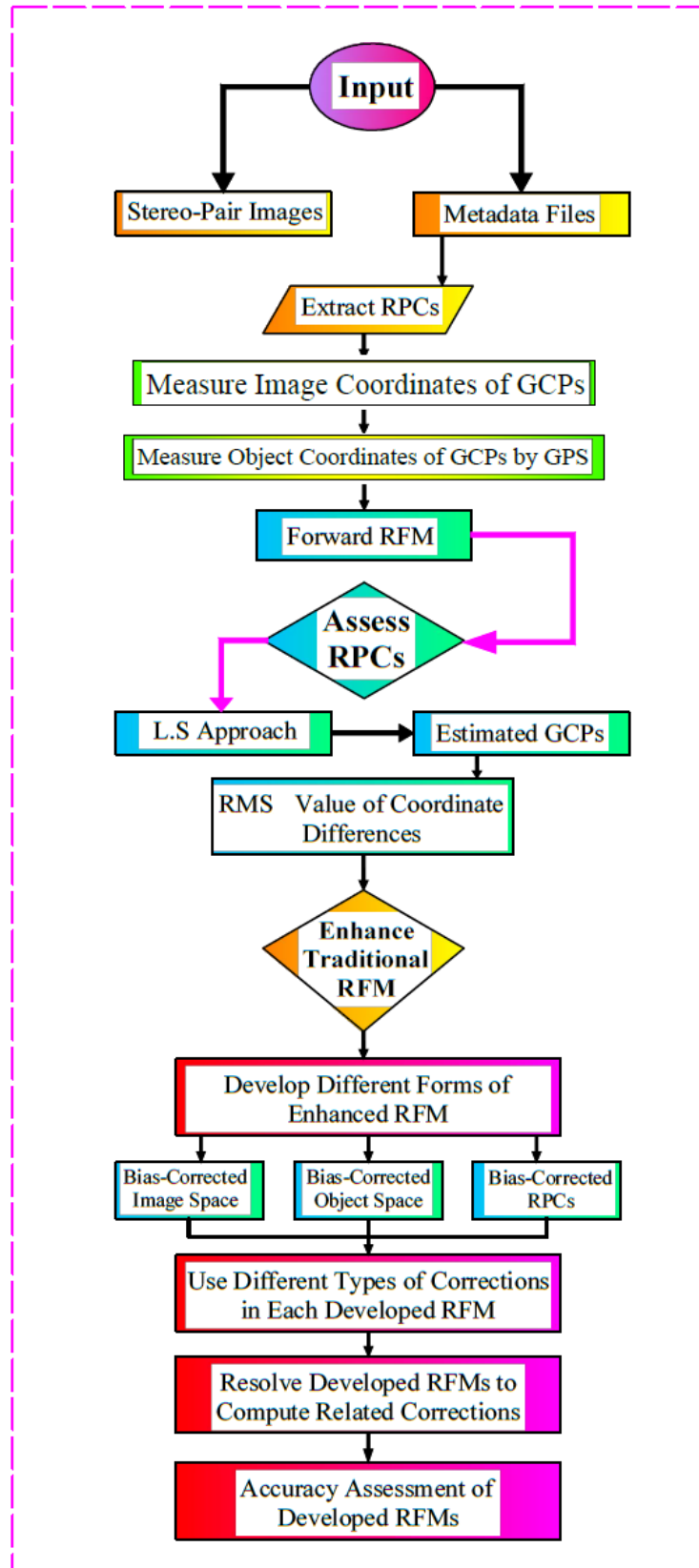


Figure (3-3) The Strategy of Developing the RFM.

3.4 GCPs Collection

High-resolution satellite imagery (HRSI) have to be geometrically and precisely processed with ground control information, such as GCPs to generate accurate map products and 3D geospatial information. Whatever the model used, even the RFM approach to eliminate the bias or refine RFM parameters, some GCPs have to be acquired to compute/refine the parameters of the mathematical functions in order to achieve a good accuracy. Generally, the number of GCPs is a function of different conditions; the method of collection, the sensor type and resolution, the image spacing, the geometric model, the study site, the physical environment, GCP definition and accuracy and the final expected accuracy (Toutin, 2004).

3.4.1 First Test Pair

For stereo IKONOS-2 satellite images restitution, GCPs were used only to compute the different sensor models which will be presented later, whereas Check Points (ChkPs) were only applied in the accuracy assessment. One of the fastest and accurate techniques is the Global Positioning System (GPS). A set of 21 well-identified and well distributed points on the images were selected. Mostly corners of buildings and fences/walls as well as road intersections were selected and surveyed using GPS in a static mode with about 5 mm accuracy. Leica Geo-office (LGO) software was used to process the data with survey positions being referenced to the UTM/WGS84 zone 36N.

A total of 21 GCPs and their corresponding image coordinates on both the left and right scene of the IKONOS-2 stereo-pair were measured in this study. Figure (3-4) shows an example of how a GCP was

determined and chosen. Figure (3-5) shows the distribution of the GPS points; GCP environment in red and ChkPs in green. Table (3-5) lists these GCPs with their 3D ground image coordinates.

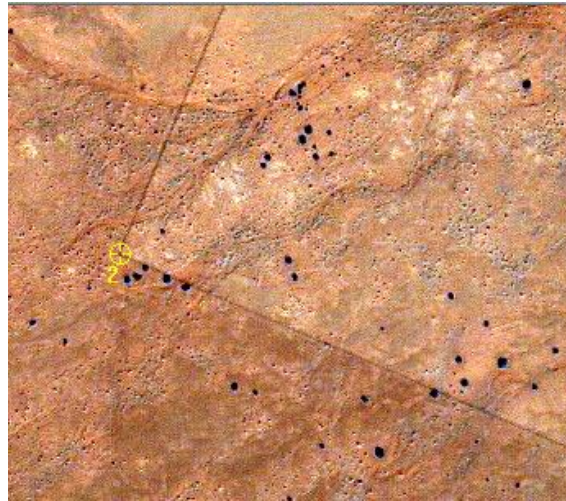


Figure (3-4) An Example of the Selection of One GCP.



Figure (3-5) GCPs and ChkPs Distribution Over the Study Area of IKONOS-2 Stereo-pair Imagery.

Table (3-5) GCPs with their 3D ground coordinates and 2D image coordinates over the study area of IKONOS-2 stereo-pair imagery

No.	Longitude (Degrees)	Latitude (Degrees)	Height (M)	Left		Right	
				Sample (Pixel)	Line (Pixel)	Sample (Pixel)	Line (Pixel)
1	32.52890754	15.80509391	381.72	5022.9	490.4	5021.6	489.9
2	32.48263749	15.80713589	404.44	0068.1	263.9	67.9	252.9
3	32.50904803	15.75861201	388.77	2885.4	5632.1	2883.1	5627.9
4	32.53038588	15.75707074	384.67	5167.4	5802.6	5164.4	5801.4
5	32.50136703	15.78488442	405.53	2066.9	2730.6	2067.1	2718.4
6	32.51027691	15.80592419	391.87	3026.6	399.6	3025.4	394.4
7	32.50390560	15.78782195	402.49	2341.6	2405.9	2341.1	2395.1
8	32.50825641	15.80470457	393.18	2810.8	534.8	2809.7	528.7
9	32.50441258	15.80403804	394.61	2398.9	608.2	2398	601.5
10	32.51034496	15.79368801	395.37	3030.9	1756.6	3031.6	1749.1
11	32.52953021	15.75995100	383.78	5077.1	5484.9	5074.6	5484.1
12	32.52548053	15.76750136	385.82	4644.6	4650.1	4642.4	4646.9
13	32.51313565	15.75775467	390.10	3319.4	5728.4	3318.4	5722.9
14	32.52829598	15.76548237	383.91	4946.4	4873.6	4944.4	4871.6
15	32.51747956	15.75897404	386.43	3785.6	5594.1	3783.9	5591.1
16	32.52472457	15.75721513	385.26	4561.6	5789.6	4560.1	5786.4
17	32.51972438	15.79319657	390.77	4036.4	1810.1	4035.1	1804.4
18	32.53028207	15.76482455	382.44	5158.7	4946.6	5156.4	4945.6
19	32.50406112	15.80195360	395.57	2360.8	839.2	2359.9	832
20	32.52955466	15.77724852	386.82	5084.4	3575.9	5082.9	3571.9
21	32.52641190	15.75676571	385.93	4741.9	5838.6	4739.9	5836.6

3.4.2 Second Test Pair

In this region, a reference receiver located over one of *El Nasr Sporting Club* buildings was used as a base station when a rover receiver was moved for collecting the GCPs. Twelve well-distributed GCPs were established by using two receivers (Trimble R8) and applying DGPS techniques in RTK mode with about 5-10 cm accuracy, were measured with reference to the WGS84. The natures of the observed points were road intersections, fences/walls, and some well-known features that can be identified easily on the image. Trimble Business Center (TBC) Software was used to process the data with survey positions being referenced to the UTM/WGS84 zone 36N. Table (3-6) present more details about the GPS field work.

A total of 12 GCPs and their corresponding image coordinates on both images of the GeoEye-1 stereo-pair were measured in this study. Figure (3-6) shows an example of how a GCP was determined in the field. The distribution of the GPS points as shown in Figure (3-7). Table (3-7) lists these GCPs with their 3D ground image coordinates.

Table (3-6) Cairo GPS Fieldwork Information

No. of points planned to collect	20 Points
No. of points collected	12 Points
No. of working days	6 Days
No. of points in Heliopolis District	4 Points
No. of points in El Marg District	5 Points
No. of points in Nasr City District	3 Points
Working Time	30 hours
Occupation time for each point	05-10 minutes
The longest base line	9.8 Km
The shortest base line	1.6 Km
Elevation Mask	13 Degrees
Intervals	5 Sec



Figure (3-6) Selection of One GCP Over the Study Area of GeoEye-1.



Figure (3-7) GCPs Distribution Over the Study Area of GeoEye-1 Stereo-pair Imagery.

Table (3-7) GCPs with their 3D ground coordinates and 2D image coordinates over the study area of GeoEye-1 stereo-pair imagery

No.	Longitude (Degrees)	Latitude (Degrees)	Height (M)	Left		Right	
				Sample (Pixel)	Line (Pixel)	Sample (Pixel)	Line (Pixel)
1	31.3918597	30.1766512	38.24	13053.8	2022.5	13034.2	2093.6
2	31.4030636	30.0520347	189.31	14916.4	29767.1	14943	29670
3	31.3298100	30.1058338	59.51	887.3	17560.2	874.1	17608.9
4	31.3782756	30.0572690	173.04	10143.1	28529.4	10163.4	28451.6
5	31.3614834	30.0798814	112.77	6939.1	23431.4	6941.6	23420.6
6	31.3305685	30.0616202	102.65	914.9	27387.1	914.9	27388.9
7	31.3312873	30.1624715	56.98	1353.7	5009.5	1339.9	5060.4
8	31.3805653	30.1485938	35.52	10787.1	8207.2	10767.9	8282.7
9	31.3638388	30.1783225	33.19	7658.9	1571.9	7638.4	1649.9
10	31.3301733	30.1445373	35.65	1068.1	8967.8	1048.4	9043.1
11	31.3457354	30.1110155	60.20	3972.9	16456.1	3959.1	16503.1
12	31.3819672	30.09400476	138.08	10948.2	20373.4	10959.1	20334.3

3.5 Used Software

3.5.1 Digital Photogrammetric Software

IMAGINE Photogrammetry Software (IPS) was used in the present research. This software runs on most computer platforms. IPS is significant because it is a leading commercial photogrammetric application that is used by numerous national mapping agencies, raster processing, GIS raster analysis, 3D visualization needs, regional mapping authorities as well as commercial mapping firms. Aside from commercial and government applications.

IMAGINE Photogrammetry is widely used in academic research such as full analytical triangulation, digital terrain model generation, Ortho-photo production, mosaicking, and 3D feature extraction, has been included in an easy-to-use environment. By automating precision measurement and including flexible operations such as terrain editing and feature extraction, IPS increases productivity while ensuring high accuracy.

In this research, IPS was used to measurement of GCPs and check points on multiple images.

3.5.2 Matlab Software Package

Matrix Laboratory (MATLAB) is a multi-paradigm numerical computing environment and fourth-generation programming language. A proprietary programming language developed by MathWorks, MATLAB allows matrix manipulations, plotting of functions and data, implementation of algorithms, creation of user interfaces, and interfacing with programs written in other languages, including C, C++, Java, Fortran and Python.

In this research, the models presented were implemented through a prototype software developed by the author in a Matlab package V.2015. In addition, statistical analysis, plotting graphs for errors, and their accuracies are investigated for 3D positioning, compared with traditional and modified RFM.

3.6 Rational Function Model

3.6.1 3D-Reconstruction using RFM

3D-reconstruction using various sensor models is one of the most important steps in accuracy assessment and enhancement of RPCs

from stereo-pair satellite imagery. 3D-reconstruction could be achieved using the vendor-supplied RPCs. To assess the accuracy and bias distribution of the results using the raw RPCs, all the ground points were used as check points. From the coordinates (ln , sn) in Equations (2-5) and (2-6), the following four equations can be derived for left (L) and right scenes (R):

$$\begin{aligned}
 F_1 = & (a_{1L} - l_{nL}b_{1L})X_n + (a_{2L} - l_{nL}b_{2L})Y_n + (a_{3L} - l_{nL}b_{3L})Z_n + (a_{4L} - l_{nL}b_{4L})X_nY_n \\
 & + (a_{5L} - l_{nL}b_{5L})X_nZ_n + (a_{6L} - l_{nL}b_{6L})Y_nZ_n + (a_{7L} - l_{nL}b_{7L})X_n^2 + (a_{8L} - l_{nL}b_{8L})Y_n^2 \\
 & + (a_{9L} - l_{nL}b_{9L})Z_n^2 + (a_{10L} - l_{nL}b_{10L})X_nY_nZ_n + (a_{11L} - l_{nL}b_{11L})X_n^3 + (a_{12L} - l_{nL}b_{12L})X_nY_n^2 \\
 & + (a_{13L} - l_{nL}b_{13L})X_nZ_n^2 + (a_{14L} - l_{nL}b_{14L})Y_nX_n^2 + (a_{15L} - l_{nL}b_{15L})Y_n^3 + (a_{16L} - l_{nL}b_{16L})Y_nZ_n^2 \\
 & + (a_{17L} - l_{nL}b_{17L})X_n^2Z_n + (a_{18L} - l_{nL}b_{18L})Y_n^2Z_n + (a_{19L} - l_{nL}b_{19L})Z_n^3 = l_{nL} - a_{0L}
 \end{aligned} \tag{3-1}$$

$$\begin{aligned}
 F_2 = & (c_{1L} - s_{nL}d_{1L})X_n + (c_{2L} - s_{nL}d_{2L})Y_n + (c_{3L} - s_{nL}d_{3L})Z_n + (c_{4L} - s_{nL}d_{4L})X_nY_n \\
 & + (c_{5L} - s_{nL}d_{5L})X_nZ_n + (c_{6L} - s_{nL}d_{6L})Y_nZ_n + (c_{7L} - s_{nL}d_{7L})X_n^2 + (c_{8L} - s_{nL}d_{8L})Y_n^2 \\
 & + (c_{9L} - s_{nL}d_{9L})Z_n^2 + (c_{10L} - s_{nL}d_{10L})X_nY_nZ_n + (c_{11L} - s_{nL}d_{11L})X_n^3 + (c_{12L} - s_{nL}d_{12L})X_nY_n^2 \\
 & + (c_{13L} - s_{nL}d_{13L})X_nZ_n^2 + (c_{14L} - s_{nL}d_{14L})Y_nX_n^2 + (c_{15L} - s_{nL}d_{15L})Y_n^3 + (c_{16L} - s_{nL}d_{16L})Y_nZ_n^2 \\
 & + (c_{17L} - s_{nL}d_{17L})X_n^2Z_n + (c_{18L} - s_{nL}d_{18L})Y_n^2Z_n + (c_{19L} - s_{nL}d_{19L})Z_n^3 = s_{nL} - c_{0L}
 \end{aligned} \tag{3-2}$$

$$\begin{aligned}
 F_3 = & (a_{1R} - l_{nR}b_{1R})X_n + (a_{2R} - l_{nR}b_{2R})Y_n + (a_{3R} - l_{nR}b_{3R})Z_n + (a_{4R} - l_{nR}b_{4R})X_nY_n \\
 & + (a_{5R} - l_{nR}b_{5R})X_nZ_n + (a_{6R} - l_{nR}b_{6R})Y_nZ_n + (a_{7R} - l_{nR}b_{7R})X_n^2 + (a_{8R} - l_{nR}b_{8R})Y_n^2 \\
 & + (a_{9R} - l_{nR}b_{9R})Z_n^2 + (a_{10R} - l_{nR}b_{10R})X_nY_nZ_n + (a_{11R} - l_{nR}b_{11R})X_n^3 + (a_{12R} - l_{nR}b_{12R})X_nY_n^2 \\
 & + (a_{13R} - l_{nR}b_{13R})X_nZ_n^2 + (a_{14R} - l_{nR}b_{14R})Y_nX_n^2 + (a_{15R} - l_{nR}b_{15R})Y_n^3 + (a_{16R} - l_{nR}b_{16R})Y_nZ_n^2 \\
 & + (a_{17R} - l_{nR}b_{17R})X_n^2Z_n + (a_{18R} - l_{nR}b_{18R})Y_n^2Z_n + (a_{19R} - l_{nR}b_{19R})Z_n^3 = l_{nR} - a_{0R}
 \end{aligned} \tag{3-3}$$

$$\begin{aligned}
F_4 = & (c_{1R} - s_{nR}d_{1R})X_n + (c_{2R} - s_{nR}d_{2R})Y_n + (c_{3R} - s_{nR}d_{3R})Z_n + (c_{4R} - s_{nR}d_{4R})X_nY_n \\
& + (c_{5R} - s_{nR}d_{5R})X_nZ_n + (c_{6R} - s_{nR}d_{6R})Y_nZ_n + (c_{7R} - s_{nR}d_{7R})X_n^2 + (c_{8R} - s_{nR}d_{8R})Y_n^2 \\
& + (c_{9R} - s_{nR}d_{9R})Z_n^2 + (c_{10R} - s_{nR}d_{10R})X_nY_nZ_n + (c_{11R} - s_{nR}d_{11R})X_n^3 + (c_{12R} - s_{nR}d_{12R})X_nY_n^2 \\
& + (c_{13R} - s_{nR}d_{13R})X_nZ_n^2 + (c_{14R} - s_{nR}d_{14R})Y_nX_n^2 + (c_{15R} - s_{nR}d_{15R})Y_n^3 + (c_{16R} - s_{nR}d_{16R})Y_nZ_n^2 \\
& + (c_{17R} - s_{nR}d_{17R})X_n^2Z_n + (c_{18R} - s_{nR}d_{18R})Y_n^2Z_n + (c_{19R} - s_{nR}d_{19R})Z_n^3 = s_{nR} - c_{0R}
\end{aligned} \tag{3-4}$$

Where n_L in l_{nL} , and s_{nL} represents the normalized image space for left scene; n_R in l_{nR} , and s_{nR} are the normalized image space for right scene; L in a_{1L} , b_{1L} , c_{1L} , and d_{1L} are the original coefficients of left scene; R in a_{1R} , b_{1R} , c_{1R} , and d_{1R} represents the original coefficients of right scene; and n in X_n , Y_n , and Z_n are the normalized object space for both images.

Because of non-linearity of the equations and by applying the Taylor series expansion, the following equations can be derived by linearizing Equations (3-1) – (3-4).

$$\begin{aligned}
F_1(X_n, Y_n, Z_n) &= F_1^0(X_n, Y_n, Z_n) + \frac{\partial F_1}{\partial X_n} \Big|_0 dX_n + \frac{\partial F_1}{\partial Y_n} \Big|_0 dY_n + \frac{\partial F_1}{\partial Z_n} \Big|_0 dZ_n = l_{nL} - a_{0L} \\
F_2(X_n, Y_n, Z_n) &= F_2^0(X_n, Y_n, Z_n) + \frac{\partial F_2}{\partial X_n} \Big|_0 dX_n + \frac{\partial F_2}{\partial Y_n} \Big|_0 dY_n + \frac{\partial F_2}{\partial Z_n} \Big|_0 dZ_n = s_{nL} - c_{0L} \\
F_3(X_n, Y_n, Z_n) &= F_3^0(X_n, Y_n, Z_n) + \frac{\partial F_3}{\partial X_n} \Big|_0 dX_n + \frac{\partial F_3}{\partial Y_n} \Big|_0 dY_n + \frac{\partial F_3}{\partial Z_n} \Big|_0 dZ_n = l_{nR} - a_{0R} \\
F_4(X_n, Y_n, Z_n) &= F_4^0(X_n, Y_n, Z_n) + \frac{\partial F_4}{\partial X_n} \Big|_0 dX_n + \frac{\partial F_4}{\partial Y_n} \Big|_0 dY_n + \frac{\partial F_4}{\partial Z_n} \Big|_0 dZ_n = s_{nR} - c_{0R}
\end{aligned} \tag{3-5}$$

The equations can be described in a matrix form as follow (Ghilani and Wolf, 2006).

$$AX + BV = K \tag{3-6}$$

(3-7)

The unknown object space coordinates are solved for iteratively. At the first iteration, initial values for coordinates are needed, which could be determined through linear equations such as 3D-Affine or DLT model.

The partial derivatives can be calculated similar to what follows:

$$\begin{aligned}
\left. \frac{\partial F_1}{\partial X_n} \right|_0 &= (a_{1L} - l_{nL} b_{1L}) + (a_{4L} - l_{nL} b_{4L}) Y_n + (a_{5L} - l_{nL} b_{5L}) Z_n + 2(a_{7L} - l_{nL} b_{7L}) X_n \\
&\quad + (a_{10L} - l_{nL} b_{10L}) Y_n Z_n + 3(a_{11L} - l_{nL} b_{11L}) X_n^2 + (a_{12L} - l_{nL} b_{12L}) Y_n^2 \\
&\quad + (a_{13L} - l_{nL} b_{13L}) Z_n^2 + 2(a_{14L} - l_{nL} b_{14L}) X_n Y_n + 2(a_{17L} - l_{nL} b_{17L}) X_n Z_n
\end{aligned} \tag{3-8a}$$

$$\begin{aligned}
\left. \frac{\partial F_1}{\partial Y_n} \right|_0 &= (a_{2L} - l_{nL} b_{2L}) + (a_{4L} - l_{nL} b_{4L}) X_n + (a_{6L} - l_{nL} b_{6L}) Z_n + 2(a_{8L} - l_{nL} b_{8L}) Y_n \\
&\quad + (a_{10L} - l_{nL} b_{10L}) X_n Z_n + 2(a_{12L} - l_{nL} b_{12L}) X_n Y_n + (a_{14L} - l_{nL} b_{14L}) X_n^2 \\
&\quad + 3(a_{15L} - l_{nL} b_{15L}) Y_n^2 + (a_{16L} - l_{nL} b_{16L}) Z_n^2 + 2(a_{18L} - l_{nL} b_{18L}) Y_n Z_n
\end{aligned} \tag{3-8b}$$

$$\begin{aligned}
\left. \frac{\partial F_1}{\partial Z_n} \right|_0 &= (a_{3L} - l_{nL} b_{3L}) + (a_{5L} - l_{nL} b_{5L}) X_n + (a_{6L} - l_{nL} b_{6L}) Y_n + 2(a_{9L} - l_{nL} b_{9L}) Z_n \\
&\quad + (a_{10L} - l_{nL} b_{10L}) X_n Y_n + 2(a_{13L} - l_{nL} b_{13L}) X_n Z_n + (a_{16L} - l_{nL} b_{16L}) Y_n Z_n \\
&\quad + (a_{17L} - l_{nL} b_{17L}) X_n^2 + 2(a_{18L} - l_{nL} b_{18L}) Y_n^2 + 3(a_{19L} - l_{nL} b_{19L}) Z_n^2
\end{aligned} \tag{3-8c}$$

$$\begin{aligned}
\left. \frac{\partial F_2}{\partial X_n} \right|_0 &= (c_{1L} - s_{nL} d_{1L}) + (c_{4L} - s_{nL} d_{4L}) Y_n + (c_{5L} - s_{nL} d_{5L}) Z_n + 2(c_{7L} - s_{nL} d_{7L}) X_n \\
&\quad + (c_{10L} - s_{nL} d_{10L}) Y_n Z_n + 3(c_{11L} - s_{nL} d_{11L}) X_n^2 + (c_{12L} - s_{nL} d_{12L}) Y_n^2 \\
&\quad + (c_{13L} - s_{nL} d_{13L}) Z_n^2 + 2(c_{14L} - s_{nL} d_{14L}) X_n Y_n + 2(c_{17L} - s_{nL} d_{17L}) X_n Z_n
\end{aligned} \tag{3-9a}$$

$$\begin{aligned}
\left. \frac{\partial F_2}{\partial Y_n} \right|_0 &= (c_{2L} - s_{nL} d_{2L}) + (c_{4L} - s_{nL} d_{4L}) X_n + (c_{6L} - s_{nL} d_{6L}) Z_n + 2(c_{8L} - s_{nL} d_{8L}) Y_n \\
&\quad + (c_{10L} - s_{nL} d_{10L}) X_n Z_n + 2(c_{12L} - s_{nL} d_{12L}) X_n Y_n + (c_{14L} - s_{nL} d_{14L}) X_n^2 \\
&\quad + 3(c_{15L} - s_{nL} d_{15L}) Y_n^2 + (c_{16L} - s_{nL} d_{16L}) Z_n^2 + 2(c_{18L} - s_{nL} d_{18L}) Y_n Z_n
\end{aligned} \tag{3-9b}$$

$$\begin{aligned}
\left. \frac{\partial F_2}{\partial Z_n} \right|_0 &= (c_{3L} - s_{nL} d_{3L}) + (c_{5L} - s_{nL} d_{5L}) X_n + (c_{6L} - s_{nL} d_{6L}) Y_n + 2(c_{9L} - s_{nL} d_{9L}) Z_n \\
&\quad + (c_{10L} - s_{nL} d_{10L}) X_n Y_n + 2(c_{13L} - s_{nL} d_{13L}) X_n Z_n + (c_{16L} - s_{nL} d_{16L}) Y_n Z_n \\
&\quad + (c_{17L} - s_{nL} d_{17L}) X_n^2 + 2(c_{18L} - s_{nL} d_{18L}) Y_n^2 + 3(c_{19L} - s_{nL} d_{19L}) Z_n^2
\end{aligned} \tag{3-9c}$$

$$\begin{aligned} \frac{\partial F_3}{\partial X_n} \Big|_0 = & (a_{1R} - l_{nR}b_{1R}) + (a_{4R} - l_{nR}b_{4R})Y_n + (a_{5R} - l_{nR}b_{5R})Z_n + 2(a_{7R} - l_{nR}b_{7R})X_n \\ & + (a_{10R} - l_{nR}b_{10R})Y_nZ_n + 3(a_{11R} - l_{nR}b_{11R})X_n^2 + (a_{12R} - l_{nR}b_{12R})Y_n^2 \\ & + (a_{13R} - l_{nR}b_{13R})Z_n^2 + 2(a_{14R} - l_{nR}b_{14R})X_nY_n + 2(a_{17R} - l_{nR}b_{17R})X_nZ_n \end{aligned} \quad (3-10a)$$

$$\begin{aligned} \frac{\partial F_3}{\partial Y_n} \Big|_0 = & (a_{2R} - l_{nR}b_{2R}) + (a_{4R} - l_{nR}b_{4R})X_n + (a_{6R} - l_{nR}b_{6R})Z_n + 2(a_{8R} - l_{nR}b_{8R})Y_n \\ & + (a_{10R} - l_{nR}b_{10R})X_nZ_n + 2(a_{12R} - l_{nR}b_{12R})X_nY_n + (a_{14R} - l_{nR}b_{14R})X_n^2 \\ & + 3(a_{15R} - l_{nR}b_{15R})Y_n^2 + (a_{16R} - l_{nR}b_{16R})Z_n^2 + 2(a_{18R} - l_{nR}b_{18R})Y_nZ_n \end{aligned} \quad (3-10b)$$

$$\begin{aligned} \frac{\partial F_3}{\partial Z_n} \Big|_0 = & (a_{3R} - l_{nR}b_{3R}) + (a_{5R} - l_{nR}b_{5R})X_n + (a_{6R} - l_{nR}b_{6R})Y_n + 2(a_{9R} - l_{nR}b_{9R})Z_n \\ & + (a_{10R} - l_{nR}b_{10R})X_nY_n + 2(a_{13R} - l_{nR}b_{13R})X_nZ_n + (a_{16R} - l_{nR}b_{16R})Y_nZ_n \\ & + (a_{17R} - l_{nR}b_{17R})X_n^2 + 2(a_{18R} - l_{nR}b_{18R})Y_n^2 + 3(a_{19R} - l_{nR}b_{19R})Z_n^2 \end{aligned} \quad (3-10c)$$

$$\begin{aligned} \frac{\partial F_4}{\partial X_n} \Big|_0 = & (c_{1R} - s_{nR}d_{1R}) + (c_{4R} - s_{nR}d_{4R})Y_n + (c_{5R} - s_{nR}d_{5R})Z_n + 2(c_{7R} - s_{nR}d_{7R})X_n \\ & + (c_{10R} - s_{nR}d_{10R})Y_nZ_n + 3(c_{11R} - s_{nR}d_{11R})X_n^2 + (c_{12R} - s_{nR}d_{12R})Y_n^2 \\ & + (c_{13R} - s_{nR}d_{13R})Z_n^2 + 2(c_{14R} - s_{nR}d_{14R})X_nY_n + 2(c_{17R} - s_{nR}d_{17R})X_nZ_n \end{aligned} \quad (3-11a)$$

$$\begin{aligned} \frac{\partial F_4}{\partial Y_n} \Big|_0 = & (c_{2R} - s_{nR}d_{2R}) + (c_{4R} - s_{nR}d_{4R})X_n + (c_{6R} - s_{nR}d_{6R})Z_n + 2(c_{8R} - s_{nR}d_{8R})Y_n \\ & + (c_{10R} - s_{nR}d_{10R})X_nZ_n + 2(c_{12R} - s_{nR}d_{12R})X_nY_n + (c_{14R} - s_{nR}d_{14R})X_n^2 \\ & + 3(c_{15R} - s_{nR}d_{15R})Y_n^2 + (c_{16R} - s_{nR}d_{16R})Z_n^2 + 2(c_{18R} - s_{nR}d_{18R})Y_nZ_n \end{aligned} \quad (3-11b)$$

$$\begin{aligned} \frac{\partial F_4}{\partial Z_n} \Big|_0 = & (c_{3R} - s_{nR}d_{3R}) + (c_{5R} - s_{nR}d_{5R})X_n + (c_{6R} - s_{nR}d_{6R})Y_n + 2(c_{9R} - s_{nR}d_{9R})Z_n \\ & + (c_{10R} - s_{nR}d_{10R})X_nY_n + 2(c_{13R} - s_{nR}d_{13R})X_nZ_n + (c_{16R} - s_{nR}d_{16R})Y_nZ_n \\ & + (c_{17R} - s_{nR}d_{17R})X_n^2 + 2(c_{18R} - s_{nR}d_{18R})Y_n^2 + 3(c_{19R} - s_{nR}d_{19R})Z_n^2 \end{aligned} \quad (3-11c)$$

The full set of unknowns in Equation (3-6) can be resolved by using the Least-squares adjustment method as follow (Mikhail and Gracie, 1981).

$$X = \left(A^T (BB^T)^{-1} A \right)^{-1} \left(A^T (BB^T)^{-1} K \right) \quad (3-12)$$

Solving the results literately until the difference between the nearly two consequent calculations are smaller than a threshold:

$$\begin{aligned} X_{h+1} &= X_h + \Delta X_h \\ Y_{h+1} &= Y_h + \Delta Y_h \\ Z_{h+1} &= Z_h + \Delta Z_h \end{aligned} \quad h = 0, 1, 2, 3, \dots \quad (3-13)$$

3.7 RFM and RPCs Refinement Methods

As mentioned earlier, the RPCs may be refined directly or indirectly. In this research, indirect method is adopted using three different approaches, as described in subsections 2.4.1, 2.4.2, and 2.4.3.

3.7.1 Bias-Corrected RPCs

The method aims to improve the RPCs that describe the perspective imaging geometry and then enhances the quality of the 3D-reconstructions. The new adjustable functions can be defined as follows:

$$l_n = \frac{P_1 (X_n, Y_n, Z_n) + \Delta P_1}{P_2 (X_n, Y_n, Z_n) + \Delta P_2} \quad (3-14)$$

$$s_n = \frac{P_3 (X_n, Y_n, Z_n) + \Delta P_3}{P_4 (X_n, Y_n, Z_n) + \Delta P_4} \quad (3-15)$$

Where ΔP_1 , ΔP_2 , ΔP_3 , and ΔP_4 are the differences between the original and the adjustable, which can be generally described as:

$$\begin{aligned}
\Delta P_1 &= A_0 + A_1 X_n + A_2 Y_n + A_3 Z_n + \dots + A_{19} Z_n^3 \\
\Delta P_2 &= B_0 + B_1 X_n + B_2 Y_n + B_3 Z_n + \dots + B_{19} Z_n^3 \\
\Delta P_3 &= C_0 + C_1 X_n + C_2 Y_n + C_3 Z_n + \dots + C_{19} Z_n^3 \\
\Delta P_4 &= D_0 + D_1 X_n + D_2 Y_n + D_3 Z_n + \dots + D_{19} Z_n^3
\end{aligned} \tag{3-16}$$

A_i , B_i , C_i and D_i are the correction parameters in the correction model. The resulted estimates of correction parameters are added to the original coefficients to get refined RPCs.

Based on the analysis of the studies in (Fraser and Hanley, 2003, 2005; Di et al., 2003; and Singh et al., 2008), four comparative choices of correction parameters are tested in this research, this can be summarized as follows:

Case One. It accounts only for the removal of shift or bias from the RPCs. And in this case, the line numerator coefficient A_0 , sample numerator coefficient C_0 , line denominator coefficient B_0 and sample denominator coefficient D_0 or shift parameters are modified for both the images.

Case Two. In addition to the parameters in Case one, the parameters A_1 , B_1 , C_1 , and D_1 which models the shift and scale.

Case Three. In addition to the parameters in Case two, the parameters A_2 , B_2 , C_2 and D_2 which models the bias using 2D first order Polynomials.

Case Four. $A_0 \approx A_3$, $B_0 \approx B_3$, $C_0 \approx C_3$, and $D_0 \approx D_3$ which models the bias using 3D first order Polynomials and requires greater number of GCPs, as the number of unknowns is more.

3.7.1.1 Modelling with One Parameter

According to the above description in Equations (3-14) and (3-15), this model in a total of eight unknowns, the following four equations can be derived:

$$\begin{aligned}
 F_1 = & (a_{1L} - l_{nL}b_{1L})X_n + (a_{2L} - l_{nL}b_{2L})Y_n + (a_{3L} - l_{nL}b_{3L})Z_n + (a_{4L} - l_{nL}b_{4L})X_nY_n \\
 & + (a_{5L} - l_{nL}b_{5L})X_nZ_n + (a_{6L} - l_{nL}b_{6L})Y_nZ_n + (a_{7L} - l_{nL}b_{7L})X_n^2 + (a_{8L} - l_{nL}b_{8L})Y_n^2 \\
 & + (a_{9L} - l_{nL}b_{9L})Z_n^2 + (a_{10L} - l_{nL}b_{10L})X_nY_nZ_n + (a_{11L} - l_{nL}b_{11L})X_n^3 + (a_{12L} - l_{nL}b_{12L})X_nY_n^2 \\
 & + (a_{13L} - l_{nL}b_{13L})X_nZ_n^2 + (a_{14L} - l_{nL}b_{14L})Y_nX_n^2 + (a_{15L} - l_{nL}b_{15L})Y_n^3 + (a_{16L} - l_{nL}b_{16L})Y_nZ_n^2 \\
 & + (a_{17L} - l_{nL}b_{17L})X_n^2Z_n + (a_{18L} - l_{nL}b_{18L})Y_n^2Z_n + (a_{19L} - l_{nL}b_{19L})Z_n^3 \\
 & - l_{nL}(1 + B_{0L}) + (A_{0L} - a_{0L}) = 0
 \end{aligned} \tag{3-17}$$

$$\begin{aligned}
 F_2 = & (c_{1L} - s_{nL}d_{1L})X_n + (c_{2L} - s_{nL}d_{2L})Y_n + (c_{3L} - s_{nL}d_{3L})Z_n + (c_{4L} - s_{nL}d_{4L})X_nY_n \\
 & + (c_{5L} - s_{nL}d_{5L})X_nZ_n + (c_{6L} - s_{nL}d_{6L})Y_nZ_n + (c_{7L} - s_{nL}d_{7L})X_n^2 + (c_{8L} - s_{nL}d_{8L})Y_n^2 \\
 & + (c_{9L} - s_{nL}d_{9L})Z_n^2 + (c_{10L} - s_{nL}d_{10L})X_nY_nZ_n + (c_{11L} - s_{nL}d_{11L})X_n^3 + (c_{12L} - s_{nL}d_{12L})X_nY_n^2 \\
 & + (c_{13L} - s_{nL}d_{13L})X_nZ_n^2 + (c_{14L} - s_{nL}d_{14L})Y_nX_n^2 + (c_{15L} - s_{nL}d_{15L})Y_n^3 + (c_{16L} - s_{nL}d_{16L})Y_nZ_n^2 \\
 & + (c_{17L} - s_{nL}d_{17L})X_n^2Z_n + (c_{18L} - s_{nL}d_{18L})Y_n^2Z_n + (c_{19L} - s_{nL}d_{19L})Z_n^3 \\
 & - s_{nL}(1 + D_{0L}) + (C_{0L} - c_{0L}) = 0
 \end{aligned} \tag{3-18}$$

$$\begin{aligned}
 F_3 = & (a_{1R} - l_{nR}b_{1R})X_n + (a_{2R} - l_{nR}b_{2R})Y_n + (a_{3R} - l_{nR}b_{3R})Z_n + (a_{4R} - l_{nR}b_{4R})X_nY_n \\
 & + (a_{5R} - l_{nR}b_{5R})X_nZ_n + (a_{6R} - l_{nR}b_{6R})Y_nZ_n + (a_{7R} - l_{nR}b_{7R})X_n^2 + (a_{8R} - l_{nR}b_{8R})Y_n^2 \\
 & + (a_{9R} - l_{nR}b_{9R})Z_n^2 + (a_{10R} - l_{nR}b_{10R})X_nY_nZ_n + (a_{11R} - l_{nR}b_{11R})X_n^3 + (a_{12R} - l_{nR}b_{12R})X_nY_n^2 \\
 & + (a_{13R} - l_{nR}b_{13R})X_nZ_n^2 + (a_{14R} - l_{nR}b_{14R})Y_nX_n^2 + (a_{15R} - l_{nR}b_{15R})Y_n^3 + (a_{16R} - l_{nR}b_{16R})Y_nZ_n^2 \\
 & + (a_{17R} - l_{nR}b_{17R})X_n^2Z_n + (a_{18R} - l_{nR}b_{18R})Y_n^2Z_n + (a_{19R} - l_{nR}b_{19R})Z_n^3 \\
 & - l_{nR}(1 + B_{0R}) + (A_{0R} - a_{0R}) = 0
 \end{aligned} \tag{3-19}$$

$$\begin{aligned}
F_4 = & (c_{1R} - s_{nR}d_{1R})X_n + (c_{2R} - s_{nR}d_{2R})Y_n + (c_{3R} - s_{nR}d_{3R})Z_n + (c_{4R} - s_{nR}d_{4R})X_nY_n \\
& + (c_{5R} - s_{nR}d_{5R})X_nZ_n + (c_{6R} - s_{nR}d_{6R})Y_nZ_n + (c_{7R} - s_{nR}d_{7R})X_n^2 + (c_{8R} - s_{nR}d_{8R})Y_n^2 \\
& + (c_{9R} - s_{nR}d_{9R})Z_n^2 + (c_{10R} - s_{nR}d_{10R})X_nY_nZ_n + (c_{11R} - s_{nR}d_{11R})X_n^3 + (c_{12R} - s_{nR}d_{12R})X_nY_n^2 \\
& + (c_{13R} - s_{nR}d_{13R})X_nZ_n^2 + (c_{14R} - s_{nR}d_{14R})Y_nX_n^2 + (c_{15R} - s_{nR}d_{15R})Y_n^3 + (c_{16R} - s_{nR}d_{16R})Y_nZ_n^2 \\
& + (c_{17R} - s_{nR}d_{17R})X_n^2Z_n + (c_{18R} - s_{nR}d_{18R})Y_n^2Z_n + (c_{19R} - s_{nR}d_{19R})Z_n^3 \\
& - s_{nR}(1 + D_{0R}) + (C_{0R} - c_{0R}) = 0
\end{aligned} \tag{3-20}$$

Where $_{0L}$ in A_{0L} , B_{0L} , C_{0L} , and D_{0L} are the shift parameters in left scene; $_{0R}$ in A_{0R} , B_{0R} , C_{0R} , and D_{0R} are the shift parameters in right scene.

In this case, the linearized format of Equations (3-17)–(3-20) are given as follows:

$$\begin{aligned}
\frac{\partial F_1}{\partial A_{0L}}dA_{0L} + \frac{\partial F_1}{\partial B_{0L}}dB_{0L} + \frac{\partial F_1}{\partial C_{0L}}dC_{0L} + \frac{\partial F_1}{\partial D_{0L}}dD_{0L} &= K_L + V_{\ln L} \\
\frac{\partial F_2}{\partial A_{0L}}dA_{0L} + \frac{\partial F_2}{\partial B_{0L}}dB_{0L} + \frac{\partial F_2}{\partial C_{0L}}dC_{0L} + \frac{\partial F_2}{\partial D_{0L}}dD_{0L} &= J_L + V_{\ln L} \\
\frac{\partial F_3}{\partial A_{0R}}dA_{0R} + \frac{\partial F_3}{\partial B_{0R}}dB_{0R} + \frac{\partial F_3}{\partial C_{0R}}dC_{0R} + \frac{\partial F_3}{\partial D_{0R}}dD_{0R} &= K_R + V_{\ln R} \\
\frac{\partial F_4}{\partial A_{0R}}dA_{0R} + \frac{\partial F_4}{\partial B_{0R}}dB_{0R} + \frac{\partial F_4}{\partial C_{0R}}dC_{0R} + \frac{\partial F_4}{\partial D_{0R}}dD_{0R} &= J_R + V_{\ln R}
\end{aligned} \tag{3-21}$$

Where

$$\begin{aligned}
K_L &= (A_{0L} - a_{0L}) - l_{nL}(1 + B_{0L}) - F_1^0(X_n, Y_n, Z_n) \\
J_L &= (C_{0L} - c_{0L}) - s_{nL}(1 + D_{0L}) - F_2^0(X_n, Y_n, Z_n) \\
K_R &= (A_{0R} - a_{0R}) - l_{nR}(1 + B_{0R}) - F_3^0(X_n, Y_n, Z_n) \\
J_R &= (C_{0R} - c_{0R}) - s_{nR}(1 + D_{0R}) - F_4^0(X_n, Y_n, Z_n)
\end{aligned} \tag{3-22}$$

The correction parameters are further computed based on the control points using the LSM. For clarity, assume that 3 GCPs are used for estimation of the shift parameters (A_0 , B_0 , C_0 , and D_0) for both left and right images. As a result, 12 observation equations in 8 unknowns are yielded. They can be described as in Equation (3-23). The unknown

shift parameters can be resolved by using the LSM, utilizing Equation (3-12).

$$\begin{bmatrix} \frac{\partial F_{11}}{\partial A_{0L}} & \frac{\partial F_{11}}{\partial B_{0L}} & 0 & 0 & 0 & 0 & 0 & 0 \\ 0 & 0 & \frac{\partial F_{21}}{\partial C_{0L}} & \frac{\partial F_{21}}{\partial D_{0L}} & 0 & 0 & 0 & 0 \\ 0 & 0 & 0 & 0 & \frac{\partial F_{31}}{\partial A_{0R}} & \frac{\partial F_{31}}{\partial B_{0R}} & 0 & 0 \\ 0 & 0 & 0 & 0 & 0 & 0 & \frac{\partial F_{41}}{\partial C_{0R}} & \frac{\partial F_{41}}{\partial D_{0R}} \\ \frac{\partial F_{12}}{\partial A_{0L}} & \frac{\partial F_{12}}{\partial B_{0L}} & 0 & 0 & 0 & 0 & 0 & 0 \\ 0 & 0 & \frac{\partial F_{22}}{\partial C_{0L}} & \frac{\partial F_{22}}{\partial D_{0L}} & 0 & 0 & 0 & 0 \\ 0 & 0 & 0 & 0 & \frac{\partial F_{32}}{\partial A_{0R}} & \frac{\partial F_{32}}{\partial B_{0R}} & 0 & 0 \\ 0 & 0 & 0 & 0 & 0 & 0 & \frac{\partial F_{42}}{\partial C_{0R}} & \frac{\partial F_{42}}{\partial D_{0R}} \\ \frac{\partial F_{13}}{\partial A_{0L}} & \frac{\partial F_{13}}{\partial B_{0L}} & 0 & 0 & 0 & 0 & 0 & 0 \\ 0 & 0 & \frac{\partial F_{23}}{\partial C_{0L}} & \frac{\partial F_{23}}{\partial D_{0L}} & 0 & 0 & 0 & 0 \\ 0 & 0 & 0 & 0 & \frac{\partial F_{33}}{\partial A_{0R}} & \frac{\partial F_{33}}{\partial B_{0R}} & 0 & 0 \\ 0 & 0 & 0 & 0 & 0 & 0 & \frac{\partial F_{43}}{\partial C_{0R}} & \frac{\partial F_{43}}{\partial D_{0R}} \end{bmatrix} \begin{bmatrix} A_{0L} \\ B_{0L} \\ C_{0L} \\ D_{0L} \\ A_{0R} \\ B_{0R} \\ C_{0R} \\ D_{0R} \end{bmatrix} + \begin{bmatrix} \frac{\partial F_{11}}{\partial l_{nL}^1} & 0 & 0 & 0 & 0 & 0 & 0 & 0 & 0 & 0 \\ 0 & \frac{\partial F_{21}}{\partial s_{nL}^1} & 0 & 0 & 0 & 0 & 0 & 0 & 0 & 0 \\ 0 & 0 & \frac{\partial F_{31}}{\partial l_{nR}^1} & 0 & 0 & 0 & 0 & 0 & 0 & 0 \\ 0 & 0 & 0 & \frac{\partial F_{41}}{\partial s_{nR}^1} & 0 & 0 & 0 & 0 & 0 & 0 \\ 0 & 0 & 0 & 0 & \frac{\partial F_{12}}{\partial l_{nL}^2} & 0 & 0 & 0 & 0 & 0 \\ 0 & 0 & 0 & 0 & 0 & \frac{\partial F_{22}}{\partial s_{nL}^2} & 0 & 0 & 0 & 0 \\ 0 & 0 & 0 & 0 & 0 & 0 & \frac{\partial F_{32}}{\partial l_{nR}^2} & 0 & 0 & 0 \\ 0 & 0 & 0 & 0 & 0 & 0 & 0 & \frac{\partial F_{42}}{\partial s_{nR}^2} & 0 & 0 \\ 0 & 0 & 0 & 0 & 0 & 0 & 0 & 0 & \frac{\partial F_{13}}{\partial l_{nL}^3} & 0 \\ 0 & 0 & 0 & 0 & 0 & 0 & 0 & 0 & 0 & \frac{\partial F_{23}}{\partial s_{nL}^3} \\ 0 & 0 & 0 & 0 & 0 & 0 & 0 & 0 & 0 & 0 \\ 0 & 0 & 0 & 0 & 0 & 0 & 0 & 0 & 0 & 0 \\ 0 & 0 & 0 & 0 & 0 & 0 & 0 & 0 & 0 & 0 \\ 0 & 0 & 0 & 0 & 0 & 0 & 0 & 0 & 0 & 0 \\ 0 & 0 & 0 & 0 & 0 & 0 & 0 & 0 & 0 & 0 \end{bmatrix} \begin{bmatrix} V_{lnL}^1 \\ V_{snL}^1 \\ V_{lnR}^1 \\ V_{snR}^1 \\ V_{lnL}^2 \\ V_{snL}^2 \\ V_{lnR}^2 \\ V_{snR}^2 \\ V_{lnL}^3 \\ V_{snL}^3 \\ V_{lnR}^3 \\ V_{snR}^3 \end{bmatrix} = \begin{bmatrix} -F_{11}^0 \\ -F_{21}^0 \\ -F_{31}^0 \\ -F_{41}^0 \\ -F_{12}^0 \\ -F_{22}^0 \\ -F_{32}^0 \\ -F_{42}^0 \\ -F_{13}^0 \\ -F_{23}^0 \\ -F_{33}^0 \\ -F_{43}^0 \end{bmatrix}$$

(3-23)

Where 1, 2, and 3 in a matrix form are the number of control points.

In essence, the original terms in the numerator and denominator in Equations (3-14) and (3-15) are modified. In the equation of l_{nL} , s_{nL} , coefficients a_{0L} , b_{0L} , c_{0L} , and d_{0L} are replaced by $(a_{0L}+dA_{0L})$, $(b_{0L}+dB_{0L})$,

$(c_{oL}+dC_{oL})$ and $(d_{oL}+dD_{oL})$ respectively. And the case for the right scene is similar. In this way, the vendor-supplied RPCs can be replaced using the method mentioned above. The bias inside the initial RPCs could be corrected. Figure (3-8) shows the 3D-reconstruction steps when using updated RPCs:

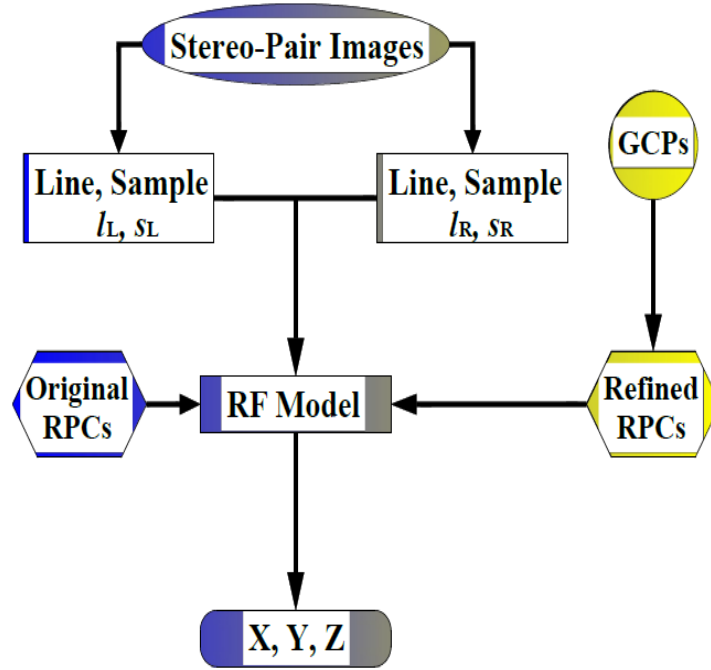


Figure (3-8) Processing Steps of 3D-reconstruction Using Updated RPCs.

3.7.1.2 Modelling with Two Parameters

If only two parameters are selected for refinement, the adjustment functions are;

$$\Delta P_1 = A_0 + A_1 X_n$$

$$\Delta P_2 = B_0 + B_1 X_n$$

$$\Delta P_3 = C_0 + C_1 X_n$$

$$\Delta P_4 = D_0 + D_1 X_n$$

(3-24)

For clarity, assume that 4 GCPs and two parameters are used for both

[illegible]

3.7.1.3 Modelling with Three Parameters

If only three parameters are selected for refinement, the adjustment functions are;

$$\begin{aligned}\Delta P_1 &= A_0 + A_1 X_n + A_2 Y_n \\ \Delta P_2 &= B_0 + B_1 X_n + B_2 Y_n \\ \Delta P_3 &= C_0 + C_1 X_n + C_2 Y_n \\ \Delta P_4 &= D_0 + D_1 X_n + D_2 Y_n\end{aligned}\quad (3-26)$$

For clarity, assume that 3 GCPs and three parameters are used for both left and right image. The observation equations ($AX + BV = K$) can be described in a matrix form as follow;

$$\begin{bmatrix} \frac{\partial F_{11}}{\partial A_{0L}} & \frac{\partial F_{11}}{\partial A_{1L}} & \frac{\partial F_{11}}{\partial A_{2L}} & \frac{\partial F_{11}}{\partial B_{0L}} & \frac{\partial F_{11}}{\partial B_{1L}} & \frac{\partial F_{11}}{\partial B_{2L}} & 0 & 0 & 0 & 0 & 0 & 0 & 0 & 0 & 0 & 0 & 0 & 0 & 0 & 0 & 0 \\ 0 & 0 & 0 & 0 & 0 & 0 & \frac{\partial F_{21}}{\partial C_{0L}} & \frac{\partial F_{21}}{\partial C_{1L}} & \frac{\partial F_{21}}{\partial C_{2L}} & \frac{\partial F_{21}}{\partial D_{0L}} & \frac{\partial F_{21}}{\partial D_{1L}} & \frac{\partial F_{21}}{\partial D_{2L}} & 0 & 0 & 0 & 0 & 0 & 0 & 0 & 0 \\ 0 & 0 & 0 & 0 & 0 & 0 & 0 & 0 & 0 & 0 & 0 & 0 & \frac{\partial F_{31}}{\partial A_{0R}} & \frac{\partial F_{31}}{\partial A_{1R}} & \frac{\partial F_{31}}{\partial A_{2R}} & \frac{\partial F_{31}}{\partial B_{0R}} & \frac{\partial F_{31}}{\partial B_{1R}} & \frac{\partial F_{31}}{\partial B_{2R}} & 0 & 0 & 0 & 0 \\ 0 & 0 & 0 & 0 & 0 & 0 & 0 & 0 & 0 & 0 & 0 & 0 & 0 & 0 & 0 & 0 & 0 & 0 & 0 & 0 \\ \frac{\partial F_{12}}{\partial A_{0L}} & \frac{\partial F_{12}}{\partial A_{1L}} & \frac{\partial F_{12}}{\partial A_{2L}} & \frac{\partial F_{12}}{\partial B_{0L}} & \frac{\partial F_{12}}{\partial B_{1L}} & \frac{\partial F_{12}}{\partial B_{2L}} & 0 & 0 & 0 & 0 & 0 & 0 & 0 & 0 & 0 & 0 & 0 & 0 & 0 & 0 \\ 0 & 0 & 0 & 0 & 0 & 0 & \frac{\partial F_{22}}{\partial C_{0L}} & \frac{\partial F_{22}}{\partial C_{1L}} & \frac{\partial F_{22}}{\partial C_{2L}} & \frac{\partial F_{22}}{\partial D_{0L}} & \frac{\partial F_{22}}{\partial D_{1L}} & \frac{\partial F_{22}}{\partial D_{2L}} & 0 & 0 & 0 & 0 & 0 & 0 & 0 & 0 \\ 0 & 0 & 0 & 0 & 0 & 0 & 0 & 0 & 0 & 0 & 0 & 0 & \frac{\partial F_{32}}{\partial A_{0R}} & \frac{\partial F_{32}}{\partial A_{1R}} & \frac{\partial F_{32}}{\partial A_{2R}} & \frac{\partial F_{32}}{\partial B_{0R}} & \frac{\partial F_{32}}{\partial B_{1R}} & \frac{\partial F_{32}}{\partial B_{2R}} & 0 & 0 & 0 & 0 \\ 0 & 0 & 0 & 0 & 0 & 0 & 0 & 0 & 0 & 0 & 0 & 0 & 0 & 0 & 0 & 0 & 0 & 0 & 0 & 0 \\ \frac{\partial F_{13}}{\partial A_{0L}} & \frac{\partial F_{13}}{\partial A_{1L}} & \frac{\partial F_{13}}{\partial A_{2L}} & \frac{\partial F_{13}}{\partial B_{0L}} & \frac{\partial F_{13}}{\partial B_{1L}} & \frac{\partial F_{13}}{\partial B_{2L}} & 0 & 0 & 0 & 0 & 0 & 0 & 0 & 0 & 0 & 0 & 0 & 0 & 0 & 0 \\ 0 & 0 & 0 & 0 & 0 & 0 & \frac{\partial F_{23}}{\partial C_{0L}} & \frac{\partial F_{23}}{\partial C_{1L}} & \frac{\partial F_{23}}{\partial C_{2L}} & \frac{\partial F_{23}}{\partial D_{0L}} & \frac{\partial F_{23}}{\partial D_{1L}} & \frac{\partial F_{23}}{\partial D_{2L}} & 0 & 0 & 0 & 0 & 0 & 0 & 0 & 0 \\ 0 & 0 & 0 & 0 & 0 & 0 & 0 & 0 & 0 & 0 & 0 & 0 & \frac{\partial F_{33}}{\partial A_{0R}} & \frac{\partial F_{33}}{\partial A_{1R}} & \frac{\partial F_{33}}{\partial A_{2R}} & \frac{\partial F_{33}}{\partial B_{0R}} & \frac{\partial F_{33}}{\partial B_{1R}} & \frac{\partial F_{33}}{\partial B_{2R}} & 0 & 0 & 0 & 0 \\ 0 & 0 & 0 & 0 & 0 & 0 & 0 & 0 & 0 & 0 & 0 & 0 & 0 & 0 & 0 & 0 & 0 & 0 & 0 & 0 \\ \frac{\partial F_{43}}{\partial C_{0R}} & \frac{\partial F_{43}}{\partial C_{1R}} & \frac{\partial F_{43}}{\partial C_{2R}} & \frac{\partial F_{43}}{\partial D_{0R}} & \frac{\partial F_{43}}{\partial D_{1R}} & \frac{\partial F_{43}}{\partial D_{2R}} & 0 & 0 & 0 & 0 & 0 & 0 & 0 & 0 & 0 & 0 & 0 & 0 & 0 & 0 \end{bmatrix} \begin{bmatrix} A_{0L} \\ A_{1L} \\ A_{2L} \\ B_{0L} \\ B_{1L} \\ B_{2L} \\ C_{0L} \\ C_{1L} \\ C_{2L} \\ D_{0L} \\ D_{1L} \\ D_{2L} \\ A_{0R} \\ A_{1R} \\ A_{2R} \\ B_{0R} \\ B_{1R} \\ B_{2R} \\ C_{0R} \\ C_{1R} \\ C_{2R} \\ D_{0R} \\ D_{1R} \\ D_{2R} \end{bmatrix} + \begin{bmatrix} \frac{\partial F_{11}}{\partial l_{nL}^1} & 0 & 0 & 0 & 0 & 0 & 0 & 0 & 0 & 0 & 0 & 0 & 0 & 0 & 0 & 0 & 0 & 0 & 0 & 0 \\ 0 & \frac{\partial F_{21}}{\partial s_{nL}^1} & 0 & 0 & 0 & 0 & 0 & 0 & 0 & 0 & 0 & 0 & 0 & 0 & 0 & 0 & 0 & 0 & 0 & 0 \\ 0 & 0 & \frac{\partial F_{31}}{\partial l_{nR}^1} & 0 & 0 & 0 & 0 & 0 & 0 & 0 & 0 & 0 & 0 & 0 & 0 & 0 & 0 & 0 & 0 & 0 \\ 0 & 0 & 0 & \frac{\partial F_{41}}{\partial s_{nR}^1} & 0 & 0 & 0 & 0 & 0 & 0 & 0 & 0 & 0 & 0 & 0 & 0 & 0 & 0 & 0 & 0 \\ 0 & 0 & 0 & 0 & \frac{\partial F_{12}}{\partial l_{nL}^2} & 0 & 0 & 0 & 0 & 0 & 0 & 0 & 0 & 0 & 0 & 0 & 0 & 0 & 0 & 0 \\ 0 & 0 & 0 & 0 & 0 & \frac{\partial F_{22}}{\partial s_{nL}^2} & 0 & 0 & 0 & 0 & 0 & 0 & 0 & 0 & 0 & 0 & 0 & 0 & 0 & 0 \\ 0 & 0 & 0 & 0 & 0 & 0 & \frac{\partial F_{32}}{\partial l_{nR}^2} & 0 & 0 & 0 & 0 & 0 & 0 & 0 & 0 & 0 & 0 & 0 & 0 & 0 \\ 0 & 0 & 0 & 0 & 0 & 0 & 0 & \frac{\partial F_{42}}{\partial s_{nR}^2} & 0 & 0 & 0 & 0 & 0 & 0 & 0 & 0 & 0 & 0 & 0 & 0 \\ 0 & 0 & 0 & 0 & 0 & 0 & 0 & 0 & \frac{\partial F_{13}}{\partial l_{nL}^3} & 0 & 0 & 0 & 0 & 0 & 0 & 0 & 0 & 0 & 0 & 0 \\ 0 & 0 & 0 & 0 & 0 & 0 & 0 & 0 & 0 & \frac{\partial F_{23}}{\partial s_{nL}^3} & 0 & 0 & 0 & 0 & 0 & 0 & 0 & 0 & 0 & 0 \\ 0 & 0 & 0 & 0 & 0 & 0 & 0 & 0 & 0 & 0 & \frac{\partial F_{33}}{\partial l_{nR}^3} & 0 & 0 & 0 & 0 & 0 & 0 & 0 & 0 & 0 \\ 0 & 0 & 0 & 0 & 0 & 0 & 0 & 0 & 0 & 0 & 0 & \frac{\partial F_{43}}{\partial s_{nR}^3} & 0 & 0 & 0 & 0 & 0 & 0 & 0 & 0 \end{bmatrix} \begin{bmatrix} V_{lnL}^1 \\ V_{snL}^1 \\ V_{lnR}^1 \\ V_{snR}^1 \\ V_{lnL}^2 \\ V_{snL}^2 \\ V_{lnR}^2 \\ V_{snR}^2 \\ V_{lnL}^3 \\ V_{snL}^3 \\ V_{lnR}^3 \\ V_{snR}^3 \end{bmatrix} = \begin{bmatrix} -F_{11}^0 \\ -F_{21}^0 \\ -F_{31}^0 \\ -F_{41}^0 \\ -F_{12}^0 \\ -F_{22}^0 \\ -F_{32}^0 \\ -F_{42}^0 \\ -F_{13}^0 \\ -F_{23}^0 \\ -F_{33}^0 \\ -F_{43}^0 \end{bmatrix}\quad (3-27)$$

3.7.2 Bias-Corrected Image Space

This bias correction method proposes a polynomial model defined in image space, in which Δl and Δs are added to the rational functions to capture the differences between the nominal and the measured image space coordinates. The new adjustable functions can be defined as follows, described in subsection 2.4.1.

$$\begin{aligned} l_n + \Delta l &= \frac{P_1(X_n, Y_n, Z_n)}{P_2(X_n, Y_n, Z_n)} \\ s_n + \Delta s &= \frac{P_3(X_n, Y_n, Z_n)}{P_4(X_n, Y_n, Z_n)} \end{aligned} \quad (3-28)$$

Where l_n and s_n are the normalized line and sample coordinates; Δl and Δs represent the differences between the measured and the calculated line and sample coordinates, which can be generally described as:

$$\begin{aligned} \Delta l &= A_0 + A_1 l + A_2 s + A_3 l^2 + A_4 l.s + A_5 s^2 + \dots \\ \Delta s &= B_0 + B_1 l + B_2 s + B_3 l^2 + B_4 l.s + B_5 s^2 + \dots \end{aligned} \quad (3-29)$$

Where A_i and B_i ($i = 1, 2, 3, \dots$) are the correction parameters. With an adequate provision of GCPs, the correction parameters are estimated by using the LSM. First, using the original vendor provided RPCs and measured object coordinates of control points based on RFM as a mathematical model to get the calculated image space (l_c, s_c) potentially containing inherent biases. The calculated image coordinates are compared with the measured image coordinates (l_m, s_m) to obtain the residuals ($\Delta l, \Delta s$). After that, the correction parameters are further computed based on the discrepancies on all the image control points using the LSM. For clarity, assume that 3 GCPs

exist for the affine parameter estimation. The observation equations ($AX + BV = K$) can be described in a matrix form as follow;

$$\begin{bmatrix} \frac{\partial F_{11}}{\partial A_{0L}} & \frac{\partial F_{11}}{\partial A_{1L}} & \frac{\partial F_{11}}{\partial A_{2L}} & 0 & 0 & 0 \\ 0 & 0 & 0 & \frac{\partial F_{21}}{\partial B_{0L}} & \frac{\partial F_{21}}{\partial B_{1L}} & \frac{\partial F_{21}}{\partial B_{2L}} \\ \frac{\partial F_{12}}{\partial A_{0L}} & \frac{\partial F_{12}}{\partial A_{1L}} & \frac{\partial F_{12}}{\partial A_{2L}} & 0 & 0 & 0 \\ 0 & 0 & 0 & \frac{\partial F_{22}}{\partial B_{0L}} & \frac{\partial F_{22}}{\partial B_{1L}} & \frac{\partial F_{22}}{\partial B_{2L}} \\ \frac{\partial F_{13}}{\partial A_{0L}} & \frac{\partial F_{13}}{\partial A_{1L}} & \frac{\partial F_{13}}{\partial A_{2L}} & 0 & 0 & 0 \\ 0 & 0 & 0 & \frac{\partial F_{23}}{\partial B_{0L}} & \frac{\partial F_{23}}{\partial B_{1L}} & \frac{\partial F_{23}}{\partial B_{2L}} \end{bmatrix} \begin{bmatrix} A_{0L} \\ A_{1L} \\ A_{2L} \\ B_{0L} \\ B_{1L} \\ B_{2L} \end{bmatrix} + \begin{bmatrix} \frac{\partial F_{11}}{\partial l_{nL}^1} & 0 & 0 & 0 & 0 & 0 \\ 0 & \frac{\partial F_{21}}{\partial s_{nL}^1} & 0 & 0 & 0 & 0 \\ 0 & 0 & \frac{\partial F_{12}}{\partial l_{nL}^2} & 0 & 0 & 0 \\ 0 & 0 & 0 & \frac{\partial F_{22}}{\partial s_{nL}^2} & 0 & 0 \\ 0 & 0 & 0 & 0 & \frac{\partial F_{13}}{\partial l_{nL}^3} & 0 \\ 0 & 0 & 0 & 0 & 0 & \frac{\partial F_{23}}{\partial s_{nL}^3} \end{bmatrix} \begin{bmatrix} V_{\ln L}^1 \\ V_{\text{sn } L}^1 \\ V_{\ln L}^2 \\ V_{\text{sn } L}^2 \\ V_{\ln L}^3 \\ V_{\text{sn } L}^3 \end{bmatrix} = \begin{bmatrix} -F_{11}^0 \\ -F_{21}^0 \\ -F_{12}^0 \\ -F_{22}^0 \\ -F_{13}^0 \\ -F_{23}^0 \end{bmatrix} \quad (3-30)$$

The six affine parameters in Equation (3-30) can be resolved by using the LSM, described in Equation (3-12). If the shift and scale bias [A_0 , A_1 , B_0 , and B_1] are the only factors taken into account, the correction can be made by improving the original RPCs.

3.7.3 Bias-Corrected Object Space

A polynomial model defined in the domain of object space to correct the ground coordinates derived from the vendor-provided RPCs as in Equation (3-31). In this method, the polynomial correction parameters are determined by the GCPs as follows:

$$\begin{aligned} X^{GPS} &= a_0 + a_1 X^{RF} + a_2 Y^{RF} + a_3 Z^{RF} \\ Y^{GPS} &= b_0 + b_1 X^{RF} + b_2 Y^{RF} + b_3 Z^{RF} \\ Z^{GPS} &= c_0 + c_1 X^{RF} + c_2 Y^{RF} + c_3 Z^{RF} \end{aligned} \quad (3-31)$$

Where X^{GPS} , Y^{GPS} , Z^{GPS} are the observed ground coordinates; X^{RF} , Y^{RF} , Z^{RF} are the ground coordinates derived from the RPC; and a_i , b_i , c_i are the correction parameters.

For clarity, assume that 4 GCPs are used for estimation of the first order polynomials ($a_0 \approx a_3$, $b_0 \approx b_3$, and $c_0 \approx c_3$). As a result, 12 observation equations in 12 unknowns are yielded. The observation equations ($AX + BV = K$) can be described in a matrix form as follow;

$$\begin{bmatrix}
 \frac{\partial F_{11}}{\partial a_0} & \frac{\partial F_{11}}{\partial a_1} & \frac{\partial F_{11}}{\partial a_2} & \frac{\partial F_{11}}{\partial a_3} & 0 & 0 & 0 & 0 & 0 & 0 & 0 & 0 \\
 0 & 0 & 0 & 0 & \frac{\partial F_{21}}{\partial b_0} & \frac{\partial F_{21}}{\partial b_1} & \frac{\partial F_{21}}{\partial b_2} & \frac{\partial F_{21}}{\partial b_3} & 0 & 0 & 0 & 0 \\
 0 & 0 & 0 & 0 & 0 & 0 & 0 & 0 & \frac{\partial F_{31}}{\partial c_0} & \frac{\partial F_{31}}{\partial c_1} & \frac{\partial F_{31}}{\partial c_2} & \frac{\partial F_{31}}{\partial c_3} \\
 \frac{\partial F_{12}}{\partial a_0} & \frac{\partial F_{12}}{\partial a_1} & \frac{\partial F_{12}}{\partial a_2} & \frac{\partial F_{12}}{\partial a_3} & 0 & 0 & 0 & 0 & 0 & 0 & 0 & 0 \\
 0 & 0 & 0 & 0 & \frac{\partial F_{22}}{\partial b_0} & \frac{\partial F_{22}}{\partial b_1} & \frac{\partial F_{22}}{\partial b_2} & \frac{\partial F_{22}}{\partial b_3} & 0 & 0 & 0 & 0 \\
 0 & 0 & 0 & 0 & 0 & 0 & 0 & 0 & \frac{\partial F_{32}}{\partial c_0} & \frac{\partial F_{32}}{\partial c_1} & \frac{\partial F_{32}}{\partial c_2} & \frac{\partial F_{32}}{\partial c_3} \\
 \frac{\partial F_{13}}{\partial a_0} & \frac{\partial F_{13}}{\partial a_1} & \frac{\partial F_{13}}{\partial a_2} & \frac{\partial F_{13}}{\partial a_3} & 0 & 0 & 0 & 0 & 0 & 0 & 0 & 0 \\
 0 & 0 & 0 & 0 & \frac{\partial F_{23}}{\partial b_0} & \frac{\partial F_{23}}{\partial b_1} & \frac{\partial F_{23}}{\partial b_2} & \frac{\partial F_{23}}{\partial b_3} & 0 & 0 & 0 & 0 \\
 0 & 0 & 0 & 0 & 0 & 0 & 0 & 0 & \frac{\partial F_{33}}{\partial c_0} & \frac{\partial F_{33}}{\partial c_1} & \frac{\partial F_{33}}{\partial c_2} & \frac{\partial F_{33}}{\partial c_3} \\
 \frac{\partial F_{14}}{\partial a_0} & \frac{\partial F_{14}}{\partial a_1} & \frac{\partial F_{14}}{\partial a_2} & \frac{\partial F_{14}}{\partial a_3} & 0 & 0 & 0 & 0 & 0 & 0 & 0 & 0 \\
 0 & 0 & 0 & 0 & \frac{\partial F_{24}}{\partial b_0} & \frac{\partial F_{24}}{\partial b_1} & \frac{\partial F_{24}}{\partial b_2} & \frac{\partial F_{24}}{\partial b_3} & 0 & 0 & 0 & 0 \\
 0 & 0 & 0 & 0 & 0 & 0 & 0 & 0 & \frac{\partial F_{34}}{\partial c_0} & \frac{\partial F_{34}}{\partial c_1} & \frac{\partial F_{34}}{\partial c_2} & \frac{\partial F_{34}}{\partial c_3}
 \end{bmatrix}
 \begin{bmatrix}
 a_0 \\
 a_1 \\
 a_2 \\
 a_3 \\
 b_0 \\
 b_1 \\
 b_2 \\
 b_3 \\
 c_0 \\
 c_1 \\
 c_2 \\
 c_3
 \end{bmatrix}
 +
 \begin{bmatrix}
 \frac{\partial F_{11}}{\partial X_1^{GPS}} & 0 & 0 & 0 & 0 & 0 & 0 & 0 & 0 & 0 & 0 & 0 \\
 0 & \frac{\partial F_{21}}{\partial Y_1^{GPS}} & 0 & 0 & 0 & 0 & 0 & 0 & 0 & 0 & 0 & 0 \\
 0 & 0 & \frac{\partial F_{31}}{\partial Z_1^{GPS}} & 0 & 0 & 0 & 0 & 0 & 0 & 0 & 0 & 0 \\
 0 & 0 & 0 & \frac{\partial F_{12}}{\partial X_2^{GPS}} & 0 & 0 & 0 & 0 & 0 & 0 & 0 & 0 \\
 0 & 0 & 0 & 0 & \frac{\partial F_{22}}{\partial Y_2^{GPS}} & 0 & 0 & 0 & 0 & 0 & 0 & 0 \\
 0 & 0 & 0 & 0 & 0 & \frac{\partial F_{32}}{\partial Z_2^{GPS}} & 0 & 0 & 0 & 0 & 0 & 0 \\
 0 & 0 & 0 & 0 & 0 & 0 & \frac{\partial F_{13}}{\partial X_3^{GPS}} & 0 & 0 & 0 & 0 & 0 \\
 0 & 0 & 0 & 0 & 0 & 0 & 0 & \frac{\partial F_{23}}{\partial Y_3^{GPS}} & 0 & 0 & 0 & 0 \\
 0 & 0 & 0 & 0 & 0 & 0 & 0 & 0 & \frac{\partial F_{33}}{\partial Z_3^{GPS}} & 0 & 0 & 0 \\
 0 & 0 & 0 & 0 & 0 & 0 & 0 & 0 & 0 & \frac{\partial F_{14}}{\partial X_4^{GPS}} & 0 & 0 \\
 0 & 0 & 0 & 0 & 0 & 0 & 0 & 0 & 0 & 0 & \frac{\partial F_{24}}{\partial Y_4^{GPS}} & 0 \\
 0 & 0 & 0 & 0 & 0 & 0 & 0 & 0 & 0 & 0 & 0 & \frac{\partial F_{34}}{\partial Z_4^{GPS}}
 \end{bmatrix}
 \begin{bmatrix}
 V_x^1 \\
 V_y^1 \\
 V_z^1 \\
 V_x^2 \\
 V_y^2 \\
 V_z^2 \\
 V_x^3 \\
 V_y^3 \\
 V_z^3 \\
 V_x^4 \\
 V_y^4 \\
 V_z^4
 \end{bmatrix}
 =
 \begin{bmatrix}
 -F_{11}^0 \\
 -F_{21}^0 \\
 -F_{31}^0 \\
 -F_{12}^0 \\
 -F_{22}^0 \\
 -F_{32}^0 \\
 -F_{13}^0 \\
 -F_{23}^0 \\
 -F_{33}^0 \\
 -F_{14}^0 \\
 -F_{24}^0 \\
 -F_{34}^0
 \end{bmatrix}$$

(3-32)

CHAPTER 4

RESULTS AND ANALYSIS

In this chapter, the original RPCs provided by the imagery vendors are firstly evaluated in Section 4.1. Second, the three proposed modified RFM models applied to the available satellite datasets, are provided in Sections 4.2 to 4.4. In addition, using the DLT and 3D-Affine models are tested against modified RFM models to check the accuracy of their output is outlined in Section 4.5 to 4.7.

4.1 Performance Evaluation of RFM

Several experiments were performed to apply the described mathematical models. Before testing and evaluating those models, the accuracy of the acquired IKONOS-2 and GeoEye-1 images was checked by locating all the ground points on the images, estimating their ground coordinates using RFM and comparing estimated coordinates to known coordinates.

4.1.1 Accuracy of IKONOS-2

The object coordinates files for IKONOS-2 image is shown in Table (4-1). The RMS value of differences between known and estimated coordinates were calculated and listed in Table (4-2) which significantly indicate the existence of large shift bias. Figure (4-1) show the planimetric and vertical accuracies at ChkPs based on vendor-supplied RPCs for IKONOS-2 stereo-pair imagery.

Table (4-1) Object Coordinates of IKONOS-2

ID	Object Space by GPS			Object Space by RPCs		
	LONG. (dd)	LAT. (dd)	Height (m)	LONG. (dd)	LAT. (dd)	Height (m)
1	32.52890754	15.80509391	381.723	32.52897244	15.80506047	403.721
2	32.4826375	15.80713589	404.44	32.48255604	15.80710324	434.238
3	32.50904803	15.75861201	388.7738	32.50911506	15.75859699	378.772
4	32.53038588	15.75707074	384.6726	32.53048621	15.75707048	367.378
5	32.50136704	15.78488443	405.533	32.50134718	15.78486181	415.141
6	32.51027692	15.8059242	391.8786	32.51026796	15.80588378	416.697
7	32.50390561	15.78782196	402.4994	32.50390937	15.78778856	413.943
8	32.50825642	15.80470458	393.1817	32.50825006	15.80466536	417.626
9	32.50441258	15.80403804	394.6192	32.50439581	15.80399964	419.149
10	32.51034496	15.79368801	395.3719	32.51035399	15.79364247	412.02
11	32.52953021	15.759951	383.786	32.52963454	15.75993661	369.146
12	32.52548054	15.76750137	385.8206	32.52555359	15.76749097	380.042
13	32.51313566	15.75775467	390.105	32.51318211	15.75774539	379.894
14	32.52829598	15.76548237	383.9102	32.52838964	15.76546775	376.041
15	32.51747957	15.75897404	386.4392	32.51754572	15.75894639	375.304
16	32.52472458	15.75721513	385.2694	32.52481595	15.75719498	372.91
17	32.51972438	15.79319658	390.7714	32.51976533	15.79316076	405.613
18	32.53028207	15.76482455	382.444	32.53038107	15.76480343	373.135
19	32.50406112	15.8019536	395.5754	32.50404545	15.80191632	418.549
20	32.52955466	15.77724853	386.8266	32.52963639	15.77721066	388.183
21	32.52641191	15.75676571	385.9385	32.5265062	15.75674515	369.838

Table (4-2) RMS Value of ChkPs Using RPCs Without GCPs for IKONOS-2

Stereo-pair	Object Space (m)		
	ΔX	ΔY	ΔZ
IKONOS-2	7.2	3.1	16.7

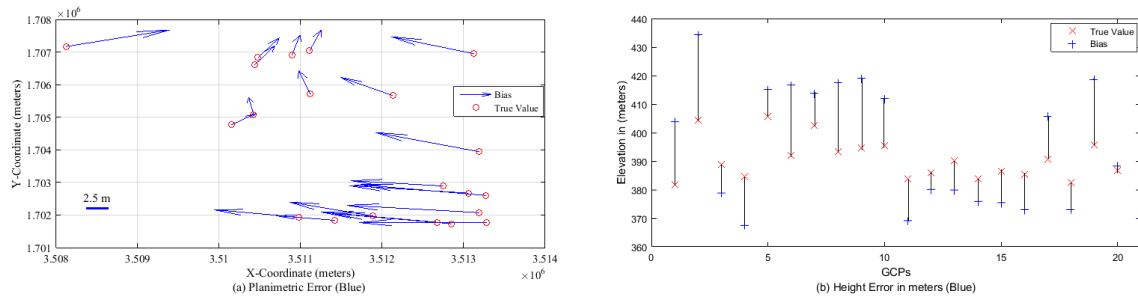


Figure (4-1) Bias Errors of (a) Planimetry and (b) Elevation at 21 ChkPs Based on Vendor-supplied RPCs for IKONOS-2 Scenes.

4.1.2 Accuracy of GeoEye-1

The object coordinates of GeoEye-1 are listed in Table (4-3). The RMS value of differences between known and estimated coordinates were calculated and listed in Table (4-4). Figure (4-2) shows the planimetric and vertical accuracies at ChkPs based on vendor-supplied RPCs for GeoEye-1 stereo-pair imagery.

Table (4-3) Object Coordinates of GeoEye-1

ID	Object Space by GPS			Object Space by RPCs		
	LONG (dd)	LAT (dd)	Height (m)	LONG (dd)	LAT (dd)	Height (m)
1	31.39185966	30.17665119	38.24	31.39187396	30.17662572	37.239
2	31.40306359	30.05203471	189.31	31.40308341	30.05200934	189.617
3	31.32981001	30.10583379	59.51	31.32981483	30.10580537	57.384
4	31.37827559	30.05726897	173.04	31.37829551	30.05723810	171.377
5	31.36148339	30.07988141	112.77	31.36148888	30.07986026	110.934
6	31.33056853	30.06162015	102.65	31.33057339	30.06159505	100.175
7	31.33128727	30.1624715	56.98	31.33128831	30.16244283	55.544
8	31.38056529	30.14859382	35.52	31.38057248	30.14857294	34.140
9	31.36383881	30.17832246	33.19	31.36384427	30.17829794	31.583
10	31.33017332	30.14453731	35.65	31.33017377	30.14451372	33.908
11	31.34573536	30.11101553	60.2	31.34573800	30.11099145	58.330
12	31.3819672	30.09400476	138.08	31.38198137	30.09397933	136.964

Table (4-4) RMS Value of ChkPs Using RPCs Without GCPs for GeoEye-1

Stereo-pair	Object Space (m)		
	ΔX	ΔY	ΔZ
GeoEye-1	1.2	2.7	1.6

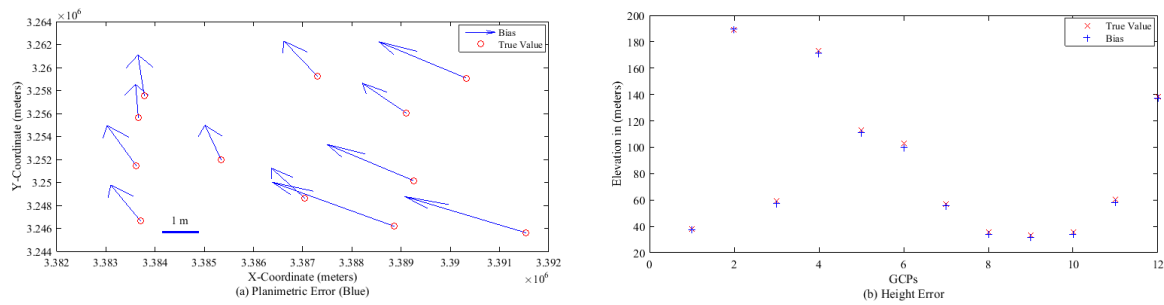


Figure (4-2) Bias Errors of (a) Planimetry and (b) Elevation at 12 ChkPs Based on Vendor-supplied RPCs for GeoEye-1 Scenes.

4.2 Bias-Corrected RPCs

The second experiment was to improve the geo-location accuracy of stereo-pair in the object space based on the bias corrected RPCs with different bias correction models and different control configurations. In this regard, the bias correction parameters were first estimated by using the LSM with the GCPs, and the bias-corrected RPCs were subsequently obtained through the RPC modification. Afterwards, the geo-location accuracies with the refined RPCs were estimated by calculating the ChkPs biases on the ground through space intersection. Detailed discussions on the result of each correction model are given below.

4.2.1 Modelling with One Parameter

As mentioned in subsection 3.7.1, the assessment for orientation using one parameter (A_0 , B_0 , C_0 , and D_0) offers a simple way to improve the geo-location accuracy.

4.2.1.1 Using IKONOS-2 Data

The results in Table (4-5) indicate that when the shift-bias was removed through RPCs modification with only three GCPs, the accuracy of ground point determination was greatly improved from the 7.2 m to 2.3 m in X, 3.1 m to 1.0 m in Y and from 16.7 m to 1.2 m in height. However, additional GCPs contributed to the improvement of the planimetric accuracy. When 17 GCPs were employed, the overall metric potential was 0.7 m in planimetry and about 1.2 m in height. Figure (4-3) is a typical example shows both the planimetric and height error based on 3 GCPs. Under such an observation, the planimetric accuracy of the refined RPC is around one meter when using 5 to 17 GCPs. On the other hand, the vertical accuracy with 3 GCPs was 1.2 m and it remains the same when 17 GCPs were used.

Table (4-5) RMS Value of ChkPs for IKONOS-2 Using One Parameter

No. GCPs/ ChkPs	Object Space (m)		
	ΔX	ΔY	ΔZ
3/18	2.3	1.0	1.2
5/16	0.9	1.0	1.6
7/14	0.8	0.9	1.7
9/12	0.9	1.0	1.8
13/8	0.3	1.0	1.5
15/6	0.3	0.6	1.5
17/4	0.3	0.6	1.2

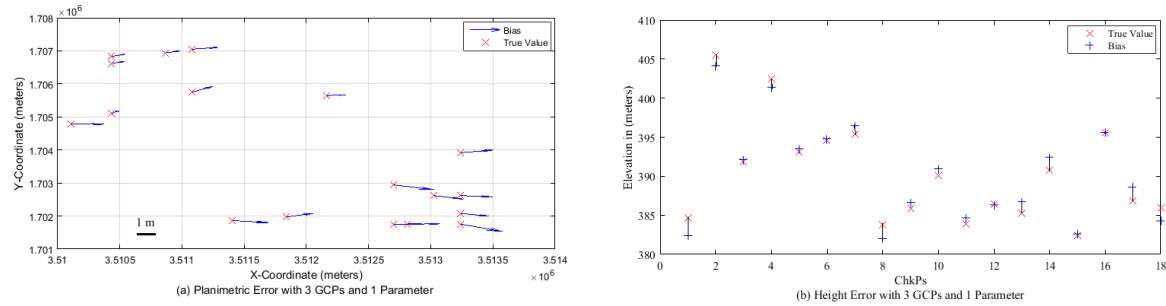


Figure (4-3) Bias Errors of (a) Planimetry and (b) Elevation at ChkPs Using 3 GCPs and One Parameter for IKONOS-2 Imagery.

4.2.1.2 Using GeoEye-1 Data

GeoEye-1 data set was tested with shift parameter by different number of GCPs, planimetric and vertical errors were checked similarly as in the case of IKONOS-2 data set. For the GeoEye-1, 12 GCPs were collected for Cairo region. Table (4-6) and Figure (4-4) shows the results of GeoEye-1 data.

Table (4-6) RMS Value of ChkPs for GeoEye-1 Using One Parameter

No. GCPs/ ChkPs	Object Space (m)		
	ΔX	ΔY	ΔZ
3/9	0.5	0.4	0.6
5/7	0.4	0.3	0.4
7/5	0.5	0.4	0.3

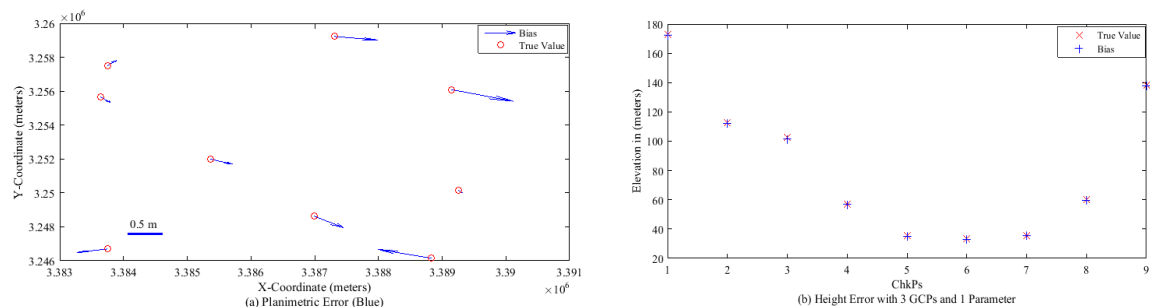


Figure (4-4) Bias Errors of (a) Planimetry and (b) Elevation at ChkPs Using 3 GCPs and One Parameter for GeoEye-1 Imagery.

4.2.2 Modelling with Two Parameters

To further test the effect of the GCP configuration, five GCPs were used to calculate the eight coefficients, A_0 , A_1 , B_0 , B_1 , C_0 , C_1 , D_0 , and D_1 .

4.2.2.1 Using IKONOS-2 Data

From Figure (4-5) and the RMS value on the ChkPs listed in Table (4-7), it is clear that the use of five GCPs could also achieve very good results in bias removing. It is obvious from the table that increasing the number of GCPs improves the results significantly. The RMS values are of the same order of magnitude as in the case of using three GCPs.

Table (4-7) RMS Value of ChkPs for IKONOS-2 Using Two Parameters

No. GCPs/ ChkPs	Object Space (m)		
	ΔX	ΔY	ΔZ
5/16	1.2	1.4	1.4
7/14	0.6	1.3	1.6
9/12	0.7	1.4	1.7
13/8	0.2	1.3	1.3
15/6	0.2	1.1	1.2
17/4	0.2	1.1	0.9

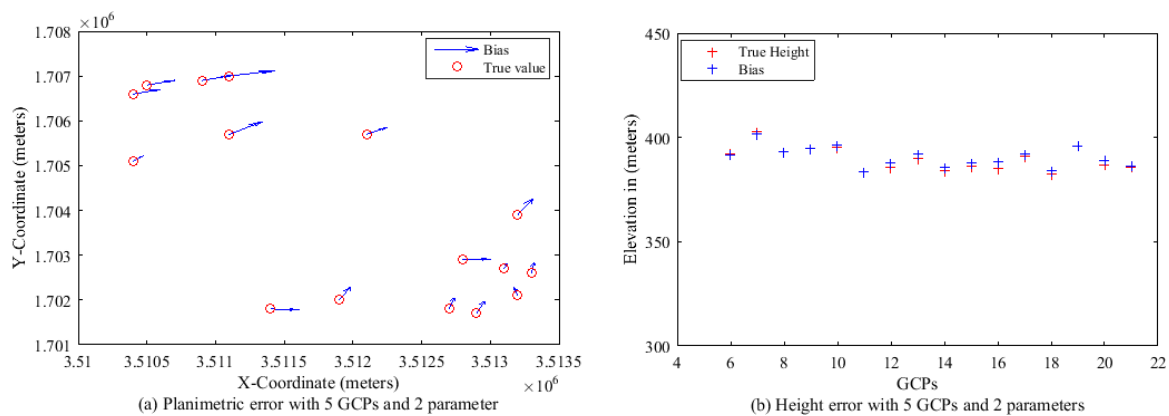


Figure (4-5) Bias Errors in (a) Planimetry and (b) Elevation of ChkPs Using 5 GCPs and Two Parameters for IKONOS-2 Imagery.

4.2.2.2 Using GeoEye-1 Data

GeoEye-1 is again tested using two parameters bias correction model, the results are shown in Table (4-8).

Table (4-8) RMS Value of ChkPs for GeoEye-1 Using Two Parameters

No. GCPs/ ChkPs	Object Space (m)		
	ΔX	ΔY	ΔZ
5/7	0.3	0.4	0.3
7/5	0.3	0.4	0.1

4.2.3 Modelling with Three Parameters

When Modelling with three parameters, 12 coefficients are updated for one image, these are A_0 , A_1 , A_2 , B_0 , B_1 , B_2 , C_0 , C_1 , C_2 , D_0 , D_1 , and D_2 . First, 7 GCPs were used to calculate all the 12 coefficients. These 7 GCPs were selected at the (edges-center-corners) of distributed area.

4.2.3.1 Using IKONOS-2 Data

From error vectors plot shown in Figure (4-6) and the RMS values listed in Table (4-9), the result generated under the control of 7 GCPs differs from the other two experiments mentioned above. This was mainly because there were expect much more significant additional error signals in the vendor-provided RPCs.

Table (4-9) RMS Value of ChkPs for IKONOS-2 Using Three Parameters

No. GCPs/ ChkPs	Object Space (m)		
	ΔX	ΔY	ΔZ
7/14	0.8	3.6	2.5
9/12	0.7	3.9	2.1
13/8	0.5	1.9	1.5
15/6	0.7	2.2	1.2
17/4	0.8	2.6	1.4

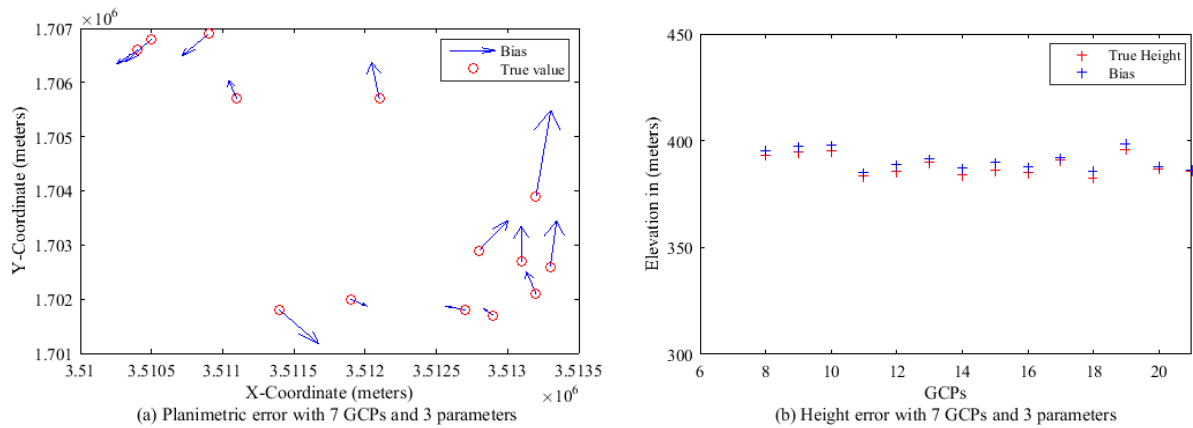


Figure (4-6) Bias Errors in (a) Planimetry and (b) Elevation of ChkPs Using 7 GCPs and Three Parameters for IKONOS-2 Imagery.

4.2.3.2 Using GeoEye-1 Data

Analysis of GeoEye-1 has been shown in Table (4-10), it can be seen that the accuracy has improved. It can be concluded from the results, that the most accurate figures, which can be obtained from stereo GeoEye-1 of around one-pixel (or less) in X, Y, and Z, when modelling with three parameters by 7 or 9 control points.

Table (4-10) RMS Value of ChkPs for GeoEye-1 Using Three Parameters

No. GCPs/ ChkPs	Object Space (m)		
	ΔX	ΔY	ΔZ
7/5	0.1	0.2	0.2
9/3	0.2	0.2	0.5

4.2.4 Modelling with Four Parameters

Four parameters constitute $A_0, A_1, A_2, A_3, B_0, B_1, B_2, B_3, C_0, C_1, C_2, C_3, D_0, D_1, D_2,$ and D_3 coefficients to change for one image, these coefficients require greater number of GCPs to change as the unknowns become more.

4.2.4.1 Using IKONOS-2 Data

From the Figure (4-7) and Table (4-11), the result generated under the control of 9 GCPs is very similar to the previous results with 3 parameters mentioned above. To conclude, the RPCs of IKONOS-2 need different approaches to reduce such biases and to achieve the desired accuracy of less than a pixel.

Table (4-11) RMS Value of ChkPs for IKONOS-2 Using Four Parameters

No. GCPs/ ChkPs	Object Space (m)		
	ΔX	ΔY	ΔZ
9/12	3.3	1.7	2.0
13/8	0.9	1.5	1.4
15/6	0.9	3.1	2.1
17/4	0.5	2.2	1.8

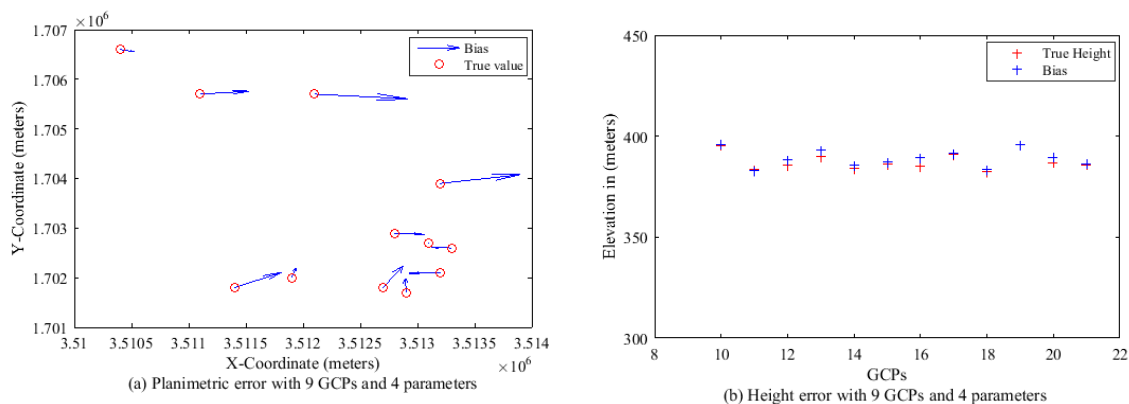


Figure (4-7) Bias Errors in (a) Planimetry and (b) Elevation of ChkPs Using 9 GCPs and Four Parameters for IKONOS-2 Imagery.

4.2.4.2 Using GeoEye-1 Data

Analysis of GeoEye-1 with four parameters has been shown in Table (4-12). In this case, one can observe that GeoEye-1 gives little accuracy as compared to previous results with 1, 2, and 3 parameters which gave sub-pixel accuracy.

Table (4-12) RMS Value of ChkPs for GeoEye-1 Using Four Parameters

No. GCPs/ ChkPs	Object Space (m)		
	ΔX	ΔY	ΔZ
9/3	1.3	0.8	2.5

4.3 Bias-Corrected Image Space

In third experiment, the refined RFM in image space was applied using the IKONOS-2 and GeoEye-1 stereo images.

4.3.1 Using IKONOS-2 Data

Table (4-13) list the RMS value for the 18 ChkPs in the object space, which implement the refined model with polynomial transformation and different numbers of GCPs. Compared with the case without any GCPs, the results are significantly improved. It is clear that, increasing the GCPs from 3 to 17 points improve the accuracy. With a minimum of five GCPs, an accuracy of 0.8 m in X, 1.2 m in Y and 1.3 m in height is achieved. To further test the effect of the GCPs configuration and parameters selection ($A_0 \approx A_5$, $B_0 \approx B_5$), seven GCPs were used to calculate the bias coefficients.

Table (4-13) RMS Value of ChkPs for IKONOS-2 Using Bias-Corrected Image Space

No. GCPs/ ChkPs	Object Space (m)								
	Shift and Scale			First Order			Second Order		
	ΔX	ΔY	ΔZ	ΔX	ΔY	ΔZ	ΔX	ΔY	ΔZ
3/18	2.4	1.0	1.2	---	---	---	---	---	---
5/16	0.9	1.0	1.6	0.8	1.2	1.3	---	---	---
7/14	0.9	0.9	1.7	0.8	1.1	1.5	1.2	1.3	2.1
9/12	1.0	1.0	1.8	0.8	1.2	1.6	1.2	1.5	2.2
13/8	0.3	1.0	1.5	0.2	1.2	1.2	0.4	1.3	1.5
15/6	0.3	0.6	1.5	0.2	1.0	1.2	0.3	1.1	1.3
17/4	0.3	0.6	1.2	0.2	0.9	0.9	0.2	1.2	1.0

4.3.2 Using GeoEye-1 Data

Table (4-14) list the RMS value for the 9 ChkPs in the object space. With a minimum of three GCPs, an accuracy of 0.4 m in X, 0.4 m in Y and 0.7 m in height is reached. By increasing the number of control points sub-meter accuracy is attained.

Table (4-14) RMS Value of ChkPs for GeoEye-1 Using Bias-Corrected Image Space

No. GCPs/ ChkPs	Object Space (m)								
	Shift and Scale			First Order			Second Order		
	ΔX	ΔY	ΔZ	ΔX	ΔY	ΔZ	ΔX	ΔY	ΔZ
3/9	0.5	0.4	0.7	0.4	0.4	0.7	---	---	---
5/7	0.4	0.3	0.4	0.3	0.3	0.6	---	---	---
7/5	0.5	0.4	0.3	0.3	0.4	0.3	0.2	0.3	0.1
9/3	0.1	0.2	0.2	0.2	0.2	0.3	0.2	0.3	0.2

4.4 Bias-Corrected Object Space

In this method, the shift parameters (a_0 , b_0 , c_0) and three additional scale factors (a_1 , b_1 , c_1) have been applied to correct for non-homogeneous scale distortions. Minimum of two GCPs are required. Additional GCPs are then added to improve accuracy.

4.4.1 Using IKONOS-2 Data

Table (4-15) shows improvements in accuracy achieved by the two different models performed in the object space for IKONOS-2 stereo-pair imagery.

The experiment starts with three GCPs and in order to increase redundancy, more GCPs should be used. With five evenly distributed GCPs, the result is improved. The RMS value is 0.9 m in X, 1.3 m in Y and 1.5 m in height. With 17 GCPs, more consistent and better results were obtained. The RMS value of 0.2 m in X, 0.9 m in Y and 0.9 m in height were achieved.

Table (4-15) RMS Value of ChkPs for IKONOS-2 Using Bias-Corrected Object Space

No. GCPs/ ChkPs	Object Space (m)					
	Shift and Scale			First Order		
	ΔX	ΔY	ΔZ	ΔX	ΔY	ΔZ
3/18	1.9	1.0	4.3	---	---	---
5/16	1.8	1.2	3.3	0.9	1.3	1.5
7/14	1.6	1.1	2.7	0.7	1.1	1.5
9/12	1.7	1.2	1.9	0.8	1.2	1.7
13/8	1.5	1.2	2.0	0.5	1.2	1.2
15/6	1.4	0.9	2.1	0.4	1.0	1.2
17/4	1.2	0.9	2.0	0.2	0.9	0.9

4.4.2 Using GeoEye-1 Data

Table (4-16) shows improvements in accuracy achieved by the two different models performed in the object space for GeoEye-1 stereo-pair imagery. With a minimum of three GCPs, the RMS value is 0.5 m in X, 0.4 m in Y and 0.9 m in height.

Table (4-16) RMS Value of ChkPs for GeoEye-1 Using Bias-Corrected Object Space

No. GCPs/ ChkPs	Object Space (m)					
	Shift and Scale			First Order		
	ΔX	ΔY	ΔZ	ΔX	ΔY	ΔZ
3/9	0.5	0.4	0.9	---	---	---
5/7	0.5	0.3	0.5	1.8	1.6	1.6
7/5	0.5	0.4	0.3	0.3	0.2	0.3
9/3	0.2	0.2	0.2	0.1	0.2	0.4

The addition of the second order parameters requires the use of a larger number of GCPs, at least 10 control points. With 11 GCPs, no significant improvements are found in comparison to the other two models. In general, high-order polynomials are very sensitive and require a large number of GCPs. The second order polynomial model does not exhibit convincing advantages over other models.

4.5 3D-Affine Model

When modelling with the 3D first order polynomial model, 8 coefficients change for one image (A_0 , A_1 , A_2 , A_3 , B_0 , B_1 , B_2 , and B_3), which requires a minimum of 4 points for the space resection. Four equations are derived for each GCP with just three unknowns X, Y and Z.

4.5.1 Using IKONOS-2 Data

Table (4-17) summarizes the performances of the polynomial models under different evenly distributed GCP and ChkPs combinations. It can be seen that there is an improvement in the results as the number of GCPs is increased. Also, the results are slightly variant to those obtained by the shift bias correction model in Table (4-5). It can be concluded, the 3D-Affine model is suitable for IKONOS *Reference*-products, which are delivered without the supplied RPCs, and/or for cases where commercial software packages are not available for the users.

Table (4-17) RMS Value of ChkPs for IKONOS-2 Using 3D-Affine Model

No. GCPs/ ChkPs	Object Space (m)					
	First Order			Second Order		
	ΔX	ΔY	ΔZ	ΔX	ΔY	ΔZ
5/16	1.0	1.4	1.5	---	---	---
7/14	0.8	1.2	1.5	3.8	1.7	2.2
9/12	0.8	1.2	1.6	2.7	1.6	2.3
13/8	0.5	1.2	1.3	1.8	1.4	2.0
15/6	0.4	1.0	1.4	1.1	1.6	1.6
17/4	0.2	0.9	1.2	1.0	1.2	1.1

4.5.2 Using GeoEye-1 Data

Table (4-18) lists the results when using the 3D-Affine model for the GeoEye-1 stereo images in the case of 5, 7, and 9 GCPs with different number of ChkPs. It can be seen that increasing the number of GCPs and parameters improves the results significantly.

Table (4-18) RMS Value of ChkPs for GeoEye-1 Using 3D-Affine Model

No. GCPs/ ChkPs	Object Space (m)					
	First Order			Second Order		
	ΔX	ΔY	ΔZ	ΔX	ΔY	ΔZ
5/7	1.7	2.0	1.7	---	---	---
7/5	1.5	0.4	0.3	1.2	0.6	0.5
9/3	1.5	0.4	0.3	0.9	0.4	0.7

4.6 DLT Model

As new sensors become operational with the new high-resolution satellite imagery, their sensor modelling may still not be available immediately. For this reason, during this investigation the capabilities of the existing systems were tested using the DLT model. First, the image space and the object space coordinates are used to calculate the respective DLT model parameter; L_1 , L_2 , L_3 , L_4 , L_5 , L_6 , L_7 , L_8 , L_9 , L_{10} , and L_{11} , described in Appendix (A). This requires a minimum of 6 GCPs for the space resection. After that, check points were measured on each image for assessing the accuracy of the derived DLT parameters.

4.6.1 Using IKONOS-2 Data

Table (4-19) listed the RMS value of the ChkPs for the IKONOS-2 stereo-pair imagery. The RMS values of the ground residuals were 1.8 m in X, 1.5 m in Y, and 2.1 m in height when 7 GCPs were used, an accuracy of 1.2 m in X, 1.0 m in Y, and 1.1 m in height is achieved when using 17 GCPs.

Table (4-19) RMS Value of ChkPs for IKONOS-2 Using DLT Model

No. GCPs/ ChkPs	Object Space (m)		
	ΔX	ΔY	ΔZ
7/14	1.8	1.5	2.1
9/12	1.7	1.7	2.2
13/8	1.6	1.4	1.5
15/6	1.8	1.4	1.4
17/4	1.2	1.0	1.1

4.6.2 Using GeoEye-1 Data

The results of the DLT model for the stereo-pair images are presented in Table (4-20) using 7 and 9 GCPs.

Table (4-20) RMS Value of ChkPs for GeoEye-1 Using DLT Model

No. GCPs/ ChkPs	Object Space (m)		
	ΔX	ΔY	ΔZ
7/5	0.7	1.4	0.4
9/3	0.2	1.6	0.6

4.7 Analysis of the Results

To figure out the accuracy of RFM and RPCs modification requires a combination of coefficients to be tested, which could be eliminated to find the optimum number of GCPs. Consequently, only a few GCPs are needed in the shift-bias in the correction model. This is very important to the end users who need good 3D-reconstruction accuracy but have only small number of GCPs available. To assess the RFM and RPCs refinement, three tests were conducted by modifying a series of parameters with varied number of GCPs, shown in Figures (4-8) and (4-9).

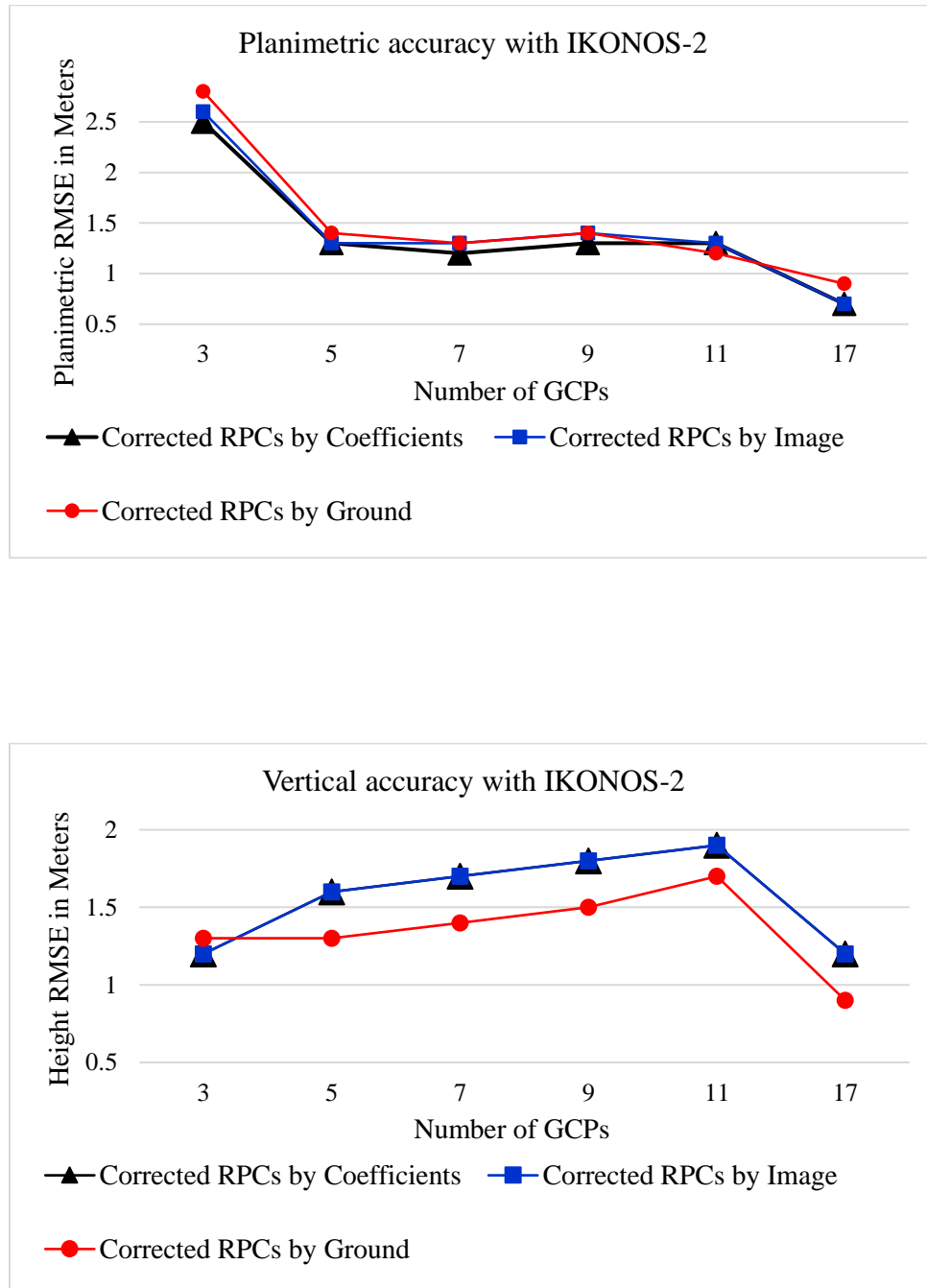


Figure (4-8) Planimetric and Vertical Accuracy of Object Coordinates of IKONOS-2 for RFM and RPCs Modification.

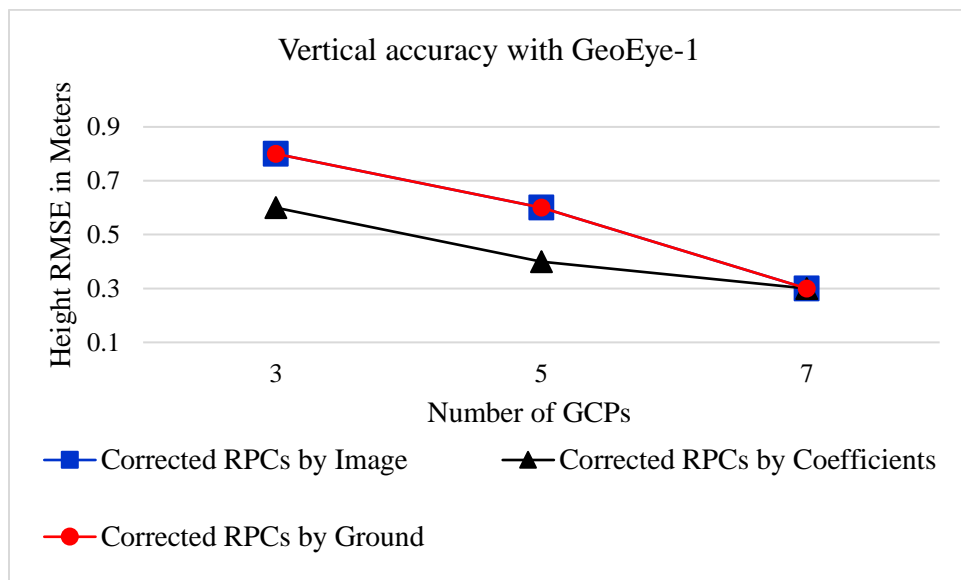
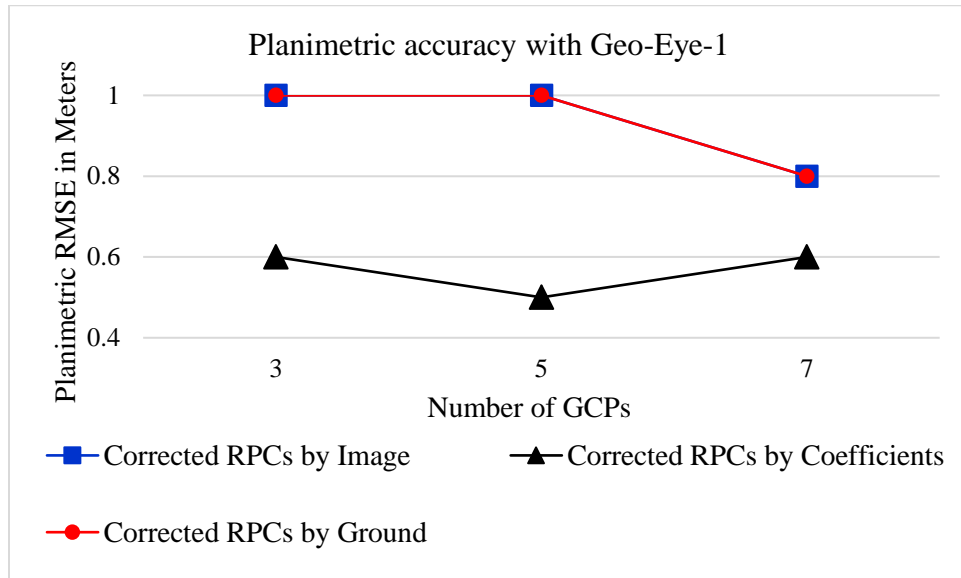


Figure (4-9) Planimetric and Vertical Accuracy of Object Coordinates of GeoEye-1 for RFM and RPCs Modification.

Firstly, the correction model in bias-corrected RPC is executed with one parameter, it accounts only for the removal of shift or bias from the RPCs.

Figure (4-8) shows that the planimetric and vertical accuracies of the refined RFM with a single parameter are accurate and stable. Under such observation, the planimetric accuracy of the refined RFM is around one-meter when using from 5 to 17 GCPs. Also, the vertical accuracy with 3 GCPs was 1.2 m, in comparison to 16 m of height with the original RPCs without any GCPs. Therefore, it can be said that the refinement achieves a significant change in the accuracy with a single parameter for IKONOS-2. Regarding GeoEye-1, Figure (4-9), the accuracy observed was 0.6 m in XY and 0.6 m in Z with one parameter using 3 GCPs wherein the accuracy with raw RPCs was 3.0 m in XY and 1.6 m in Z.

Secondly, in bias-corrected image space, the four coefficients A_0 , A_1 , B_0 , and B_1 are modified for each image. This procedure accounts for the shift and scale bias correction model. Figure (4-8) shows the planimetric and vertical accuracies of the refined RFM. In essence, 1.2 m was the observed vertical accuracy when using 3 and 17 GCPs, which is not quite significant when compared with the results of the bias-corrected RPCs, which modified one parameter giving almost the same accuracy. On the other hand, GeoEye-1 yields 0.7 m with 3 GCPs and 0.2 m with as many as 9 GCPs in height.

Lastly, in the case of bias-corrected object space, the correction model only contains shift and scale, which modifies six coefficients of the RFM for the image, and these are a_0 , b_0 , c_0 , a_1 , b_1 , and c_1 . Figure (4-8) shows that the planimetric and vertical accuracies of the refined RFM with shift and scale parameters. For IKONOS-2, the planimetric accuracy achieved was 2.1 m with 3 GCPs, which increased to 1.5 m with 17 GCPs, and the vertical accuracy with 3 GCPs was 4.3 m, which reduced to 1.9 m with 9 GCPs. In regard to GeoEye-1, the accuracy given almost the same accuracy with bias-corrected image space.

CHAPTER 5

CONCLUSIONS AND RECOMMENDATIONS

In this thesis, a proposed method was developed and applied through a prototype software in a Matlab environment with different correction models which results in reducing the biases in RPCs for stereo-pair of satellite imagery. Section 5.1 gives an outline of the research steps carried out in this thesis. Conclusions are drawn in Section 5.2 based on the attained results.

5.1 Outline

Since the IKONOS-2 and GeoEye-1 satellite imagery vendor, has not released the satellite ephemeris data, no physical mathematical model can be established. Instead, RFM as a generic model is used. This causes a significant problem in the process of geo-positioning from stereo-pair imagery with high precision. In this research, IKONOS-2 *Reference* level product and GeoEye-1 *Geo* level were used for RFM and RPCs improvement. Tasks performed in this process are GCP collection, measurement of the image coordinates, RPCs Extraction, 3D-reconstruction, RPCs modification, and accuracy evaluation. Three mathematical setups were used for performance enhancement of RFM for stereo satellite images utilizing ground control information, namely: 1) Bias-corrected RPCs; 2) Bias-corrected image space; and 3) Bias-corrected object space. The RFM and RPCs are modified using different mathematical setups were then compared, and the

accuracy of modified RFM associated with each version are compared. The three setups were tested and compared with the well-known 3D-Affine and DLT models for stereo-pair imagery. The Least-squares method was applied to implement the different mathematical setups for estimating the correction parameters. GCPs of good quality are mandatory for the RFM enhancement process, less number of GCPs is required in this process than some of the mathematical models such as DLT model. Whereas a one GCP may be sometimes sufficient to reduce the bias in the vendor-supplied RPCs and yield sub-meter level accuracy of 3D geo-location using the RFM. Three GCPs as a minimum were used in this thesis to compensate the bias when using the RFM and a minimum of 7 GCPs is used for the 3D-reconstruction when using the DLT model.

5.2 Conclusions

Physical models are not always available for satellite sensor orientation, especially for images from high-resolution satellites such as IKONOS and GeoEye-1. Unlike the physical model, inexact models such as RFM, DLT, and 3D-Affine need neither the knowledge of the sensor model nor of orbit ephemeris and platform orientation parameters. Applications of these models to stereo images acquired by IKONOS-2 and GeoEye-1 satellites indicate that relatively accurate geo-positioning can be obtained through provision of GCPs. In this thesis, RFM and RPCs enhancement methods are presented and applied on IKONOS-2 and GeoEye-1 stereo images. Based on the

reached results several findings and conclusions can be given as follows:

- The accuracy of the 3D-reconstruction performed using the vendor-supplied RPCs for both IKONOS-2 and GeoEye-1 images are considerably significant and unacceptable for photogrammetric applications. It was found that by utilizing a few number of GCPs, the bias can be improved to one-pixel level of RMSE on the ChkPs.
- The RPCs associated with GeoEye-1 imagery data have better quality and generate less bias compared with imagery data of IKONOS-2.
- Out of the three methods applied in this research, the method for bias-corrected image space is recommended since it is easy to perform and fewer GCPs are required.
- The bias-corrected object space is feasible for RFM refinement in case of using shift and scale, and first order polynomial models.
- Regarding polynomial models used, it was found that the second order polynomial model gives less accuracy than the first order model. With regard to the DLT model, the obtained accuracy figures in X, Y, and Z direction are nearly one-pixel when using large number of control points.

- The results indicate the effectiveness of 3D-Affine and DLT models especially when the RPCs and/or commercial software packages are not available for users.

Recommendations for Future Research

Based on the proposed methodology and the experimental results, some recommendations can be summarized in order to extend the research in the future.

- In the future, it is recommended to test the refined approaches with different terrain, sensors, physical model with available ephemeris parameters and compare them with the RFM.
- Utilizing the vendor-supplied RPCs as the initial values to recalculate the RPCs with the knowledge of large number of GCPs in the iterative least-squares solution.

REFERENCES

Abdel-Aziz, Y.I. and Karara, H. M. (1971) Direct linear Transformation from Comparator Coordinates into Object Space Coordinates in Close-Range Photogrammetry. Proceedings of the Symposium on Close-Range Photogrammetry. Falls Church, VA: American Society of Photogrammetry, pp: 1-18.

Abdel-Aziz, Y.I. (1982) Accuracy of the Normal Case of Close Range Photogrammetry. Photogrammetric Engineering and Remote Sensing, Vol. 48, No. 2, pp: 204-213.

Aguilar, M.A. et al. (2007) Geometric Accuracy Assessment of Quick-Bird Basic Imagery Using Different Operational Approaches. Photogrammetric Engineering & Remote Sensing, Vol. 73, No. 12, December 2007, pp. 1321–1332.

Boccardo, P. et al. (2004) Orthorectification of High Resolution Satellite Images. XXth ISPRS Congress, Technical Commission I. Volume XXXV Part B1, July 12-23, 2004, Istanbul, Turkey.

Chen, L.C., Teo, A.T., and Liu, C.L. (2006) The Geometrical Comparisons of RSM and RFM for FORMOSAT-2 Satellite Images. Photogrammetric Engineering and Remote Sensing, 72 (5), 573-579, December 2007.

Dare, P.M. (2004) Investigation of Geometric Constraints for Matching High-Resolution Satellite Images. The International Archives of the Photogrammetry, Remote Sensing and Spatial Information Sciences, Vol. 35 Part B3, Istanbul, Turkey.

Dave, P., Joshi, R., and Sri, S. (2015) A Survey on Geometric Correction of Satellite Imagery. International Journal of Computer Applications (0975 – 8887) Volume 116 – No. 12, April 2015.

Devangi, T., Amit, V.P., and Patel, M. (2016) A Survey on Geometric Distortion and Correction Methods for Finding Key Points. IJSRD - International Journal for Scientific Research & Development| Vol. 4, Issue 02, 2016 | ISSN: 2321-0613.

Devi, M.R. and Santosh, L.S.B. (2011) Geometric Correction in Recent High-Resolution Satellite Imagery: A Case Study in Coimbatore, Tamilnadu. International Journal of Computer Applications, January-2011, 0975- 8887.

Di, K. et al. (2003) Rational Functions and Potential for Rigorous Sensor Model Recovery. Photogrammetric Engineering & Remote Sensing 69 (1), 33-41.

El-Ashmawy, N. et al. (2005) Comparative Analysis and Evaluation of Various Mathematical Models for Stereo IKONOS Satellite Images. TS 27 – Remote Sensing and Photogrammetry. FIG Working Week 2005 and GSDI-8.

- Finkl, C.W. (2013) Coastal Hazards. Springer, Dordrecht, Netherlands.
- Fraser, C. et al. (1999) Geometric Characteristics of Alternative Triangulation Models for Satellite Imagery. Proceedings of 1999 ASPRS Annual Conference, From Image to Information, Oregon, May 17-21.
- Fraser, C.S., Hanley, H.B., and Yamakawa, T. (2002) 3D Positioning Accuracy of IKONOS Imagery. Photogramm. Rec. 17 (99).
- Fraser, C.S. and Hanley, H.B. (2003) Bias Compensation in Rational Functions for IKONOS Satellite Imagery. Photogrammetric Engineering & Remote Sensing 69 (1), 53-58.
- Fraser, C.S. and Hanley, H.B. (2005) Bias Compensated RPCs for Sensor Orientation of High-Resolution Satellite Imagery. Photogrammetric Engineering & Remote Sensing 71 (8), 909-915.
- Fraser, C.S. et al. (2006) Sensor orientation via RPCs. ISPRS Journal of Photogrammetry and Remote Sensing Volume 60, Issue 3, May 2006, Pages 182-194.
- GeoEye (2009) GeoEye Product Guide. Version 1.0.1.
- Gerlach, F. (2000) Characteristics of Space Imaging's One-Meter Resolution Satellite Imagery Products. International Archives of Photogrammetry and Remote Sensing. Vol. XXXIII, Part B1. Amsterdam 2000.
- Ghilani, C. D. and Wolf, P.R. (2006) Adjustment Computations: Spatial Data Analysis. Fourth Edition John Wiley & Sons, Inc. ISBN: 978-0-471- 69728-2.
- Giannone, F. (2006) A Rigorous Model for High Resolution Satellite Imagery Orientation. Ph.D., University of Rome "La Sapienza" Faculty of Engineering, Rome, 2006.
- Gong, K. and Fritsch, D. (2016) A Detailed Study about Digital Surface Model Generation Using High-Resolution Satellite Stereo Imagery. ISPRS Annals of the Photogrammetry, Remote Sensing and Spatial Information Sciences, Volume III-1.
- Grodecki, J. and Dial, G. (2003) Block Adjustment of High-Resolution Satellite Images Described by Rational Polynomials. Photogrammetric Engineering & Remote Sensing 69 (1), 59-68.
- Grodecki, J. and Dial, G. (2003a) IKONOS Stereo Accuracy without Ground Control. ASPRS Annual Conference Proceedings, Anchorage, Alaska.
- Habib, A. et al. (2007) Comprehensive Analysis of Sensor Modeling Alternatives for High-Resolution Imaging Satellites. Photogrammetric Eng. Remote Sensing 73 (11), 1241-1251.
- Hanley, H.B. and Fraser, C.S. (2004) Sensor Orientation for High-Resolution Satellite Imagery: Further Insights into Bias Compensated RPCs. The International Archives of the Photogrammetry, Remote Sensing and Spatial Information Sciences, Vol. 35 Part B1, Istanbul, Turkey.

- Hosseini, M. (2008) Analysis of Rational Function Dependency to the Height Distribution of Ground Control Points in Geometric Correction of Aerial and Satellite Images. The International Archives of the Photogrammetry, Remote Sensing and Spatial Information Sciences. Vol. XXXVII. Part B1. Beijing 2008.
- Hu, Y., Tao, V.C., and Croitor, A. (2004) Understanding the Rational Function Model: Methods and Applications. The International Archives of the Photogrammetry, Remote Sensing and Spatial Information Sciences.
- Jaber, S.M. (2006) Monitoring Spatial Variations in Soil Organic Carbon Using Remote Sensing. ProQuest Information and Learning Company, USA.
- Karara, H.M. (1985) Close Range Photogrammetry Where Are We and Where Are We Heading. Photogrammetric Engineering and Remote Sensing, Vol. 51, No. 5, pp: 537-544.
- Khorram, S. et al. (2012) Remote Sensing. Springer, New York.
- Kumar, A. (2006) CARTOSAT –1 (IRS –P5) Stereo Data Processing – A Case Study of Dehradun Area, web page accessed on 3rd December 2007.
- Leica Geosystems, (2006) Leica Photogrammetry Suite Project Manager, USA.
- Li, R. (1998) Potential of High-Resolution Satellite Imagery for National Mapping Products. Photogrammetric Engineering & Remote Sensing, 64 (12): 1165-1170.
- Li, R., Zhou, F., Niu, X., and Di, K. (2007) Integration of IKONOS and Quick-Bird Imagery for Geo-Positioning Accuracy Analysis. Photogrammetric Engineering & Remote Sensing, 73(9):1067–1074.
- Mikhail, E.M. and Dracie, G. (1981) Analysis and Adjustment of Survey Measurements. Van Nostrand Reinhold Company, New York.
- Mikhail, E.M., Bethel, J.S., and McGlone, J.C. (2001) Introduction to Modern Photogrammetry. ISBN 0-471-30924-9.
- Moffitt, F.H. and Mikhail, E.M. (1980) Photogrammetry, Third Edition. ISBN 0-700-22517-X.
- Nag, P. and Kudrat, M. (1998) Digital Remote Sensing. Concept Publishing Company, New Delhi, India.
- Novak, K. (1992) Rectification of digital imagery. Photogrammetric Engineering and Remote Sensing, 58(3), pp. 339-344.
- OGC (1999) The Open GIS Abstract Specification-Topic 7: The earth imagery Case. http://portal.opengeospatial.org/files/?artifact_id=7467.
- Poon, J. et al. (2005) Quality Assessment of Digital Surface Models Generated from IKONOS Imagery. Photogrammetric Record 20 (110), 162-171.

- Singh, G., Michel, M., Markus, G., and Shefali, A. (2008) Improved Geometric Modelling of Space Borne Push-Broom Imagery using Modified Rational Polynomial Coefficients and the Impact on DSM Generation. MSc. Thesis, International Institute for Geo-information Science and Earth Observation.
- Tao, C.V. and Hu, Y. (2000) Image Rectification Using a Generic Sensor Model – Rational Function Model. *International Archives of Photogrammetry and Remote Sensing*. Vol. 33, Part B3, pp. 874-881.
- Tao, C.V. and Hu, Y. (2001) A Comprehensive Study of the Rational Function Model for Photogrammetric Processing. *Photogrammetric Engineering & Remote Sensing*. Vol. 67, No. 12, December 2001, pp. 1347-1357.
- Tao, C.V. and Hu, Y. (2002) 3D Reconstruction Methods Based on the Rational Function Model. *Photogrammetric Engineering & Remote Sensing*, Vol. 68, No. 7, July 2002, pp. 705-714.
- Tong, X., Liu, S., and Wengb, Q. (2010) Bias-Corrected Rational Polynomial Coefficients for High Accuracy Geo-positioning of Quick-Bird Stereo Imagery. *ISPRS Journal of Photogrammetry and Remote Sensing* 65: 218-226.
- Toutin, T. (2001) Geometric Processing of IKONOS Geo images with DEM. *Proceedings of the Joint ISPRS Workshop on High Resolution Mapping from Space 2001*, 19— 21 September, Hannover, Germany, CD-ROM, 9 p.
- Toutin, T. (2004) DTM Generation from IKONOS in-track Stereo Images using a 3D Physical Model. *Photogrammetric Engineering & Remote Sensing*, 70 (6): 695— 702.
- Volpe, F. and Rossi, L. (2003) Quick-Bird High Resolution Satellite Data for Urban Applications. 2nd GRSS/ISPRS Joint Workshop on Remote Sensing and Data Fusion over Urban Areas, 22-23 May 2003, Berlin, Germany.
- Wang, Y. (1999) Automated Triangulation of Linear Scanner Imagery. *Joint Workshop of ISPRS WG I/1, I/3 and IV/4, Sensors and Mapping from Space*, Hanover, September, 27-30.
- Wolf, P. and Dewitt, B. A. (2000) *Elements of photogrammetry with Applications in GIS*. Third Edition, McGraw Hill, Boston, Massachusetts, USA.
- Wu, W., Chen, L., and Teo, T. (2008) RFM-Based Block Adjustment for Satellite Images with Weakly Convergent Geometry. M.Sc., Center for Space and Remote Sensing Research, National Center University, China.
- Xiong, Z. and Zhang, Y. (2009) A Generic Method for RPC Refinement Using Ground Control Information. *Journal of the American Society for Photogrammetry and Remote Sensing*. Vol. 75, No. 9, pp. 1083–1092.
- Xu, J.Z., Tao, C.V., and Hu, B. (2004) The Rational Function Model (RFM) in Photogrammetric Mapping: Method and Accuracy. M.Sc., Department of Earth and Space

References

Science & Engineering, Faculty of Graduate Studies, York University, North York, Ontario.

Xu, S., Li, J., and Michael, A. (2005) Automatic Extraction of Digital Elevation Models from IKONOS in-Track Stereo Images. Department of Civil Engineering, Ryerson University.

Xutong, N. et al. (2004) Geometric Modelling and Photogrammetric Processing of High-Resolution Satellite Imagery. Mapping and GIS Laboratory, CEEGS, the Ohio State University. Commission IV, WG IV/7.

Yamakawa, T. and Fraser, C.S. (2004) The Affine Projection Model for Sensor Orientation: Experiences with High-Resolution Satellite Imagery. The International Archives of the Photogrammetry, Remote Sensing and Spatial Information Sciences, Vol. 35 Part B1, Istanbul, Turkey.

Yang, X. (2000) Accuracy of Rational Function Approximation in Photogrammetry. ASPRS Annual Conference, 22-26 May, 11 p.

Yi, C. and Jue, L. (2008) Performing Space Resection Using Total Least Squares. The International Archives of the Photogrammetry, Remote Sensing and Spatial Information Sciences. Vol. XXXVII. Part B3b. Beijing 2008.

Zhang, L., Balz, T., Wei, X., and Liao, M. (2011) Rational Function Modeling for Space-Borne SAR Datasets. ISPRS Journal of Photogrammetry and Remote Sensing 66: 133–145.

<http://www.digitalglobe.com>

<http://www.geoeye.com>

<http://www.spaceimaging.com>

APPENDIX A

Basic Algorithm of Least Squares Adjustment Method Used in the Research

A.1 Parametric Least-Squares Adjustment

A.1.1 Mathematical Model

$$\bar{L} = F(\bar{X}) \quad (A-1)$$

Where

\bar{L} Vector of adjusted observations

\bar{X} Vector of adjusted unknown parameters

F Functional relationship

This model is generally non-linear and must be linearized using Taylor series expansion.

A.1.2 Linearized Observation Equations

$$V = A \Delta X - C \quad (A-2)$$

Where

$$C = L - F(X^0)$$

A.1.3 Normal Equations for the Solution Vector ΔX

Applying the least squares principle $V^T W V = \text{minimum}$, the normal equations for ΔX are obtained as:

$$N \Delta X - M = 0 \quad (A-3)$$

Where

$$N = A^T W A$$

$$M = A^T W C$$

A.1.4 Solution of the System of Normal Equations

$$\Delta X = N^{-1} M \quad (A-4)$$

To overcome the effect of non-linearity in the case of non-linear models, the solution is iterated until pre-specified precision limit is achieved.

A.1.5 Adjusted Values of the Unknown Parameters and Observations

The enhanced values of the unknown parameters are,

$$\bar{X} = X^0 + \Delta X \quad (A-5)$$

The least squares estimated values \hat{V} for the residuals are,

$$V = A \Delta X - C \quad (A-6)$$

The adjusted values of the observed quantities are,

$$\bar{L} = L + V \quad (A-7)$$

A.1.6 Estimated Variance Factor

The variance factor σ_0^2 is computed as:

$$\sigma_0^2 = \frac{V^T P V}{m - n} \quad (A-8)$$

Where m is the number of observations and n is the number of unknown parameters.

A.2 Combined Least-Squares Adjustment

A.2.1 Mathematical Model

$$F(\bar{L}, \bar{X}) = 0 \quad (A-9)$$

A.2.2 Linearized form of the Model

$$BV + A \Delta X = K \quad (\text{A-10})$$

Where B is the coefficient matrix of the observations; A is the coefficient matrix of unknown parameters; and $K = -F(X_0, L)$

A.2.3 Normal Equations for the Solution Vector ΔX

$$N \Delta X - M = 0 \quad (\text{A-11})$$

Where

$$N = A^T W A$$

$$M = A^T W K$$

W is the weight matrix of the equivalent observations

A.2.4 Solution of the System of Normal Equations

$$\Delta X = \left(A^T (BB^T)^{-1} A \right)^{-1} \left(A^T (BB^T)^{-1} K \right) \quad (\text{A-12})$$

The solution is iterated until the required precision is obtained.

A.2.5 Adjusted Values of the Unknown Parameters and Observations

$$\bar{X} = X^0 + \Delta X \quad (\text{A-13})$$

$$V = B^T (BB^T)^{-1} (K - A \Delta X) \quad (\text{A-14})$$

$$\bar{L} = L + V \quad (\text{A-15})$$

A.3 Calibration of DLT Model

The goal of DLT is to determine the actual location of the point (X, Y, Z) based on (x_L, y_L) and (x_R, y_R) . Before this can be done using an object, the system must be calibrated using points of known location.

- Mathematical Model

$$\begin{aligned}
 x &= \frac{L_1 X + L_2 Y + L_3 Z + L_4}{L_9 X + L_{10} Y + L_{11} Z + 1} \\
 y &= \frac{L_5 X + L_6 Y + L_7 Z + L_8}{L_9 X + L_{10} Y + L_{11} Z + 1}
 \end{aligned} \tag{A-16}$$

○ Calibration

Let's assume that the location of the points (X, Y, Z) are known. Given a stereo-pair of high resolution satellite imagery and measuring the image coordinates of affixed control points in each of the two images of the test pair.

$$\begin{aligned}
 x_L &= \frac{L_1 X + L_2 Y + L_3 Z + L_4}{L_9 X + L_{10} Y + L_{11} Z + 1} \\
 y_L &= \frac{L_5 X + L_6 Y + L_7 Z + L_8}{L_9 X + L_{10} Y + L_{11} Z + 1} \\
 x_R &= \frac{R_1 X + R_2 Y + R_3 Z + R_4}{R_9 X + R_{10} Y + R_{11} Z + 1} \\
 y_R &= \frac{R_5 X + R_6 Y + R_7 Z + R_8}{R_9 X + R_{10} Y + R_{11} Z + 1}
 \end{aligned} \tag{A-17}$$

From Equations (A-17), there are seven known ($x_L, y_L, x_R, y_R, X, Y, Z$), 22 unknowns ($L_1 \dots L_{11}$ & $R_1 \dots R_{11}$), and four equations in one calibration point. At least 22 equations will be used to find the 22 unknowns. For the two points in the left image frame, the equations are

$$\begin{aligned}
 x_{L1} &= L_1 X_1 + L_2 Y_1 + L_3 Z_1 + L_4 - x_{L1} L_9 X_1 - x_{L1} L_{10} Y_1 - x_{L1} L_{11} Z_1 \\
 y_{L1} &= L_5 X_1 + L_6 Y_1 + L_7 Z_1 + L_8 - y_{L1} L_9 X_1 - y_{L1} L_{10} Y_1 - y_{L1} L_{11} Z_1 \\
 x_{L2} &= L_1 X_2 + L_2 Y_2 + L_3 Z_2 + L_4 - x_{L2} L_9 X_2 - x_{L2} L_{10} Y_2 - x_{L2} L_{11} Z_2 \\
 y_{L2} &= L_5 X_2 + L_6 Y_2 + L_7 Z_2 + L_8 - y_{L2} L_9 X_2 - y_{L2} L_{10} Y_2 - y_{L2} L_{11} Z_2
 \end{aligned} \tag{A-18}$$

Equations (A-18) can be expressed in a matrix form up to n calibration points as follows:

$$AX = L + V \tag{A-19}$$

[illegible]

The values of $L_1 \dots L_{11}$ are the only unknowns. A similar matrix system involving $x_R, y_R, \text{ and } R_1 \dots R_{11}$ can be written. Equation (A-19) may be solved using least squares technique presented in Section (A.1).

- 3D Point Positioning

In Equations (A-18), after calibration, $L_1 \dots L_{11}, R_1 \dots R_{11}$ are known and x_L, y_L, x_R, y_R , are known by inspecting the images. There are thus three unknowns (X, Y, and Z) and four equations. Rearrange the equations and combining into a matrix system yields;

$$\begin{bmatrix} L_1 - L_9 x_L & L_2 - L_{10} x_L & L_3 - L_{11} x_L \\ L_5 - L_9 y_L & L_6 - L_{10} y_L & L_7 - L_{11} y_L \\ R_1 - R_9 x_R & R_2 - R_{10} x_R & R_3 - R_{11} x_R \\ R_5 - R_9 y_R & R_6 - R_{10} y_R & R_7 - R_{11} y_R \end{bmatrix} \begin{bmatrix} X \\ Y \\ Z \end{bmatrix} = \begin{bmatrix} x_L - L_4 \\ y_L - L_8 \\ x_R - R_4 \\ y_R - R_8 \end{bmatrix}$$

may be solved explicitly for the vector of unknowns (X, Y, Z) , by applying the method of least squares described in Section (A.1).

APPENDIX B

TECHNICAL INFORMATION

B.1 GeoEye-1

Launched on September 6, 2008, GeoEye-1 simultaneously captures image detail up to 0.41-meters for panchromatic images and 1.65-meters for multispectral images. GeoEye-1 orbits the Earth every 98 minutes at an altitude of approximately 681 kilometers or 423 miles. The satellite travels a sun-synchronous orbit, passing the equator at about 10:30 AM local time. GeoEye-1 can collect up to 700,000 square kilometers per day, or over 255 million square kilometers per year.

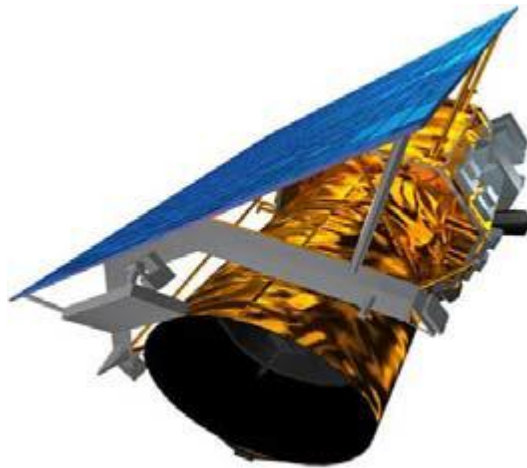


Figure (B-1) GeoEye-1 Satellite

B.1.1 Geo Imagery

Data Source: GeoEye-1 (.50-meter panchromatic; 2-meter multispectral) and IKONOS (1-meter panchromatic; 4-meter multispectral) satellite imagery.

Processing: Radiometric correction, geometric correction, and rectification to a map projection.

Accuracy: .50-meter products have 5-meter circular error at 90% probability (CE90) and 1-meter products have 15-meter (CE90). Both accuracies are exclusive of terrain displacement. Accuracy is defined as the horizontal distance between true position and the position of an image point projected down to true elevation by RPC or rigorous camera model. Geo accuracy is achieved with on-board attitude and ephemeris sensors, and does not require use of ground control points (GCPs).

Image Area: The customer order Area of Interest (AOI) is defined by a geographic rectangle or by a customer-supplied shapefile.

Camera Model: The camera model maps ground coordinates to image coordinates. The camera model is provided in RPC format. RPC camera model data is provided in RPC00B format in NITF files and in text format with GeoTIFF orders. Block adjustment, orthorectification, and other photogrammetric processing can be performed with the RPC camera model.

Target Angles: Sensor target elevation angle from horizon to sensor as seen from the area of interest (AOI). This is typically $> 60^\circ$ but may, with customer consent, be reduced below 60° to facilitate collection. Customers may request collection above 72 degrees for an additional fee. Scan azimuth is typically North-South or East-West, but may be reoriented at GeoEye discretion.

Mosaic: None.

B.1.2 Default Product Parameters

Listed below are the default product parameters. Please consult with a Service Expert should you require different options.

Band Combinations – Red, Green, Blue (pansharpened, true color)

Datum – WGS84

Projection – Universal Transverse Mercator

Units – Meters

Bits – 8 bit

Dynamic range adjustment – on

Media – DVD

Resample method – cubic convolution

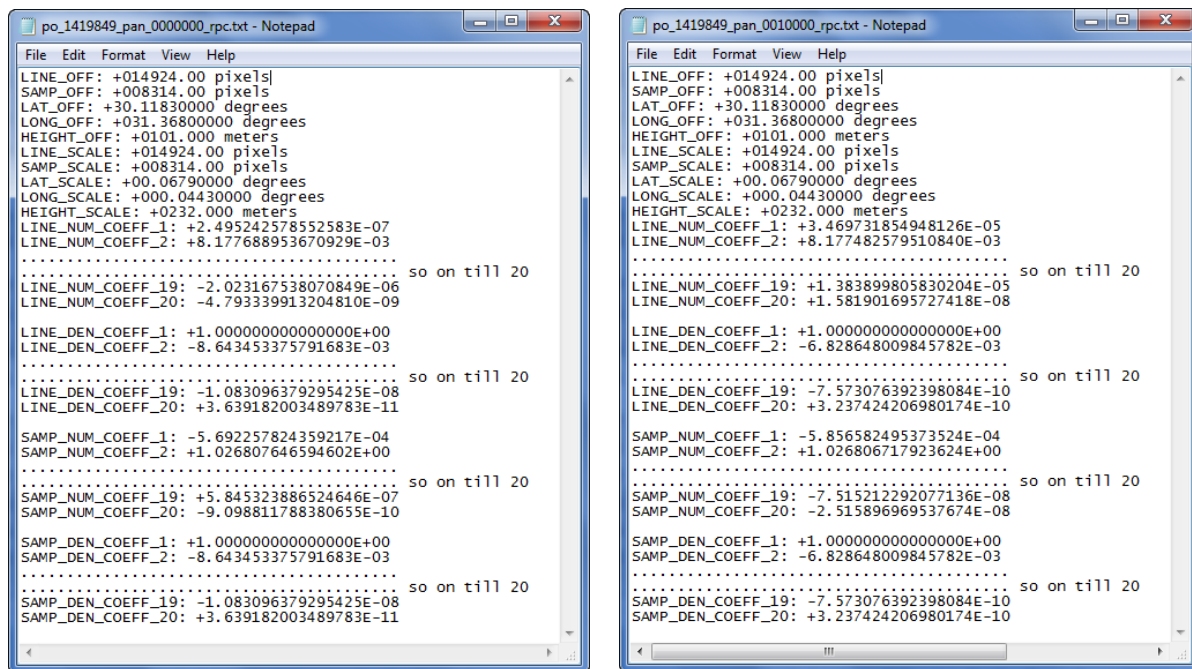
File format – GeoTIFF

License type – single user

Rational Polynomial Coefficient – yes

B.1.3 GeoEye-1 Parameters

The parameters of GeoEye-1 stereo-pair imagery provided by the vendor in the format of “image_name_rpc.txt” as illustrated in Figure (B-2).



(a) Left Scene

(b) Right Scene

Figure (B-2) Sample for Normalized RPCs of GeoEye-1 Imagery.

B.2 IKONOS

Launched in 1999, IKONOS collects .82-meter panchromatic and 3.28-meter multispectral data at a rate of over 240,000 square kilometers per day or over 87 million square kilometers per year. IKONOS orbits the Earth every 98 minutes at an altitude of approximately 681 kilometers or 423 miles. The satellite travels a sun-synchronous orbit, always crossing the equator at about 10:30 AM local time.

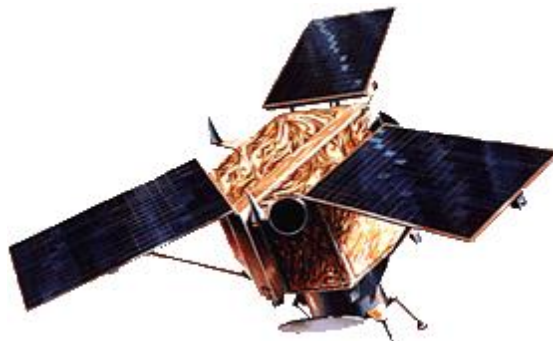


Figure (B-3) IKONOS Satellite

B.2.1 IKONOS-2 Parameters

```

File Edit Format View Help
LINE_OFF: +002946.00 pixels
SAMP_OFF: +002675.00 pixels
LAT_OFF: +15.78280000 degrees
LONG_OFF: +032.50710000 degrees
HEIGHT_OFF: +0394.000 meters
LINE_SCALE: +002947.00 pixels
SAMP_SCALE: +002676.00 pixels
LAT_SCALE: +00.02680000 degrees
LONG_SCALE: +000.02510000 degrees
HEIGHT_SCALE: +0064.000 meters
LINE_NUM_COEFF_1: +1.401552015175975E-03
LINE_NUM_COEFF_2: +2.134825572695891E-03
.....so on till 20
LINE_NUM_COEFF_19: -2.693965190732577E-05
LINE_NUM_COEFF_20: +1.746782340125102E-07

LINE_DEN_COEFF_1: +1.000000000000000E+00
LINE_DEN_COEFF_2: +1.226261670153810E-04
.....so on till 20
LINE_DEN_COEFF_19: +2.533231662606649E-09
LINE_DEN_COEFF_20: -8.214533000037751E-10

SAMP_NUM_COEFF_1: -1.060740377650102E-04
SAMP_NUM_COEFF_2: +1.004654772485838E+00
.....so on till 20
SAMP_NUM_COEFF_19: +2.380782549280767E-07
SAMP_NUM_COEFF_20: +3.822498137225629E-08

SAMP_DEN_COEFF_1: +1.000000000000000E+00
SAMP_DEN_COEFF_2: +1.226261670153810E-04
.....so on till 20
SAMP_DEN_COEFF_19: +2.533231662606649E-09
SAMP_DEN_COEFF_20: -8.214533000037751E-10

```

```

File Edit Format View Help
LINE_OFF: +003002.00 pixels
SAMP_OFF: +002678.00 pixels
LAT_OFF: +15.78230000 degrees
LONG_OFF: +032.50710000 degrees
HEIGHT_OFF: +0394.000 meters
LINE_SCALE: +003002.00 pixels
SAMP_SCALE: +002679.00 pixels
LAT_SCALE: +00.02730000 degrees
LONG_SCALE: +000.02510000 degrees
HEIGHT_SCALE: +0064.000 meters
LINE_NUM_COEFF_1: +1.122308088753380E-03
LINE_NUM_COEFF_2: +2.095901891457477E-03
.....so on till 20
LINE_NUM_COEFF_19: +2.961849651435377E-05
LINE_NUM_COEFF_20: +2.926386550645194E-08

LINE_DEN_COEFF_1: +1.000000000000000E+00
LINE_DEN_COEFF_2: +3.856112611538160E-04
.....so on till 20
LINE_DEN_COEFF_19: -3.990784072479867E-09
LINE_DEN_COEFF_20: +7.519313601230690E-10

SAMP_NUM_COEFF_1: +9.712117649664215E-04
SAMP_NUM_COEFF_2: +1.003532589841644E+00
.....so on till 20
SAMP_NUM_COEFF_19: -1.719503912121135E-07
SAMP_NUM_COEFF_20: -1.073354854626956E-07

SAMP_DEN_COEFF_1: +1.000000000000000E+00
SAMP_DEN_COEFF_2: +3.856112611538160E-04
.....so on till 20
SAMP_DEN_COEFF_19: -3.990784072479867E-09
SAMP_DEN_COEFF_20: +7.519313601230690E-10

```

(a) Left Scene

(b) Right Scene

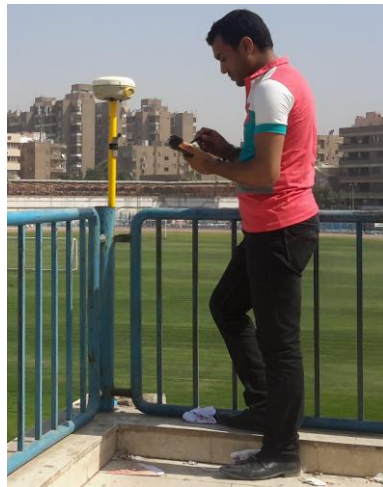
Figure (B-4) Sample for Normalized RPCs of IKONOS-2 provided by the vendor.

B.3 Detailed Descriptions of the Points

One sheet per GCP is presented in the following. Each sheet includes:


- The point identification number,
- Measurement date, time, and the method (RTK, Static),
- Geographical coordinates and ellipsoidal height values,
- The instrument id,
- Number of GPS satellites observed,
- The surveyors' names,
- An overview image of each point (snapshots are taken from Google Earth).

Point ID: 03	Date: 22-05-2017	No. of Sat.: 21	Surveyor:
30 06 21.02 N	Inst. No.: 5147477050	PDOP: 2.4	
31 19 47.32 E	Ant. No.: 47477050	Obs. Start: 10:12:12 AM	Tamer Saleh Karim Atef
h: 59.510 m	Trimble (R8)	Obs. End: 07:11:22 PM	
El Nasr Sporting Club			




Point ID: 08	Date: 10-06-2017	No. of Sat.: 15	Surveyor:
30 08 54.94 N	Inst. No.: 5147477050	GPS RTK	
31 22 50.04 E	Ant. No.: 47477050	Obs. Time: 05:00 AM	Tamer Saleh Soudi El-Masry
h: 35.52 m	Trimble (R8)	PDOP: 3.1	

El-Marj





Point ID: 01	Date: 14-06-2017	No. of Sat.: 19	Surveyor: Tamer Saleh Soudi El-Masry
30 10 35.94 N	Inst. No.: 5147477050	GPS RTK	
31 23 30.69 E	Ant. No.: 47477050	Obs. Time: 05:00 AM	
h: 38.24 m	Trimble (R8)	PDOP: 2.7	
El-Salam			



APPENDIX C

MATHEMATICAL FORMULATION OF THE PROPOSED ALGORITHM

Matlab Code for 3D-reconstruction Using RFM

```
% 3D RECONSTRUCTION USING RFM
format short g
clc; clear all;
% LOAD GCPS & ICS AND POLYNOMIAL COEFFICIENTS
Obs = load('E:\Tamer\IK\WGS84_Obse.txt');
MIC_L = load('E:\Tamer\IK\MIC_L.txt');
MIC_R = load('E:\Tamer\IK\MIC_R.txt');
C = load('E:\Tamer\IK\Coeff.txt');
N = length(Obs);
% NORMALIZATION OF GROUND CONTROL POINTS
for i = 1 : N;
XL(i)=(Obs(i,2)-long_offL)/long_scaL;
YL(i)=(Obs(i,3)-lat_offL)/lat_scaL;
ZL(i)=(Obs(i,4)-H_offL)/H_scaL;
XR(i)=(Obs(i,2)-long_offR)/long_scaR;
YR(i)=(Obs(i,3)-lat_offR)/lat_scaR;
ZR(i)=(Obs(i,4)-H_offR)/H_scaR;
xnL(i)=(MIC_L(i,2)-(sample_offL))/(sample_scaL);
ynL(i)=(MIC_L(i,3)-(line_offL))/(line_scaL);
xnR(i)=(MIC_R(i,2)-(sample_offR))/(sample_scaR);
ynR(i)=(MIC_R(i,3)-(line_offR))/(line_scaR);
end
% THE POLYNOMIAL FORM IS AS FOLLOW
for i = 1 : N;
F1(i) = ((C(2,1)-(ynL(i)*C(2,2)))*(XL(i)))+(C(3,1)-(ynL(i)*C(3,2)))*(YL(i)))+(C(4,1)-(ynL(i)*C(4,2)))*(ZL(i)))+(C(5,1)-(ynL(i)*C(5,2)))*(XL(i)*YL(i)))+(C(6,1)-(ynL(i)*C(6,2)))*(XL(i)*ZL(i)))+(C(7,1)-(ynL(i)*C(7,2)))*(YL(i)*ZL(i)))+(C(8,1)-(ynL(i)*C(8,2)))*(XL(i)*XL(i)))+(C(9,1)-(ynL(i)*C(9,2)))*(YL(i)*YL(i)))+(C(10,1)-(ynL(i)*C(10,2)))*(ZL(i)*ZL(i)))+(C(11,1)-(ynL(i)*C(11,2)))*(XL(i)*YL(i)*ZL(i)))+(C(12,1)-(ynL(i)*C(12,2)))*(XL(i)*XL(i)*XL(i)))+(C(13,1)-(ynL(i)*C(13,2)))*(XL(i)*YL(i)*YL(i)))+(C(14,1)-(ynL(i)*C(14,2)))*(XL(i)*ZL(i)*ZL(i)))+(C(15,1)-(ynL(i)*C(15,2)))*(YL(i)*XL(i)*XL(i)))+(C(16,1)-(ynL(i)*C(16,2)))*(YL(i)*YL(i)*YL(i)))+(C(17,1)-(ynL(i)*C(17,2)))*(YL(i)*ZL(i)*ZL(i)))+(C(18,1)-(ynL(i)*C(18,2)))*(XL(i)*XL(i)*ZL(i)))+(C(19,1)-(ynL(i)*C(19,2)))*(YL(i)*YL(i)*ZL(i)))+(C(20,1)-(ynL(i)*C(20,2)))*(ZL(i)*ZL(i)*ZL(i));
F2(i) = ((C(2,3)-(xnL(i)*C(2,4)))*(XL(i)))+(C(3,3)-(xnL(i)*C(3,4)))*(YL(i)))+(C(4,3)-(xnL(i)*C(4,4)))*(ZL(i)))+(C(5,3)-(xnL(i)*C(5,4)))*(XL(i)*YL(i)))+(C(6,3)-(xnL(i)*C(6,4)))*(XL(i)*ZL(i)))+(C(7,3)-(xnL(i)*C(7,4)))*(YL(i)*ZL(i)))+(C(8,3)-(xnL(i)*C(8,4)))*(XL(i)*XL(i)))+(C(9,3)-(xnL(i)*C(9,4)))*(YL(i)*YL(i)))+(C(10,3)-(xnL(i)*C(10,4)))*(ZL(i)*ZL(i)))+(C(11,3)-(xnL(i)*C(11,4)))*(XL(i)*YL(i)*ZL(i)))+(C(12,3)-(xnL(i)*C(12,4)))*(XL(i)*XL(i)*XL(i)))+(C(13,3)-(xnL(i)*C(13,4)))*(XL(i)*YL(i)*YL(i)))+(C(14,3)-(xnL(i)*C(14,4)))*(XL(i)*ZL(i)*ZL(i)))+(C(15,3)-(xnL(i)*C(15,4)))*(YL(i)*XL(i)*XL(i)))+(C(16,3)-(xnL(i)*C(16,4)))*(YL(i)*YL(i)*YL(i)))+(C(17,3)-(xnL(i)*C(17,4)))*(YL(i)*ZL(i)*ZL(i)))+(C(18,3)-(xnL(i)*C(18,4)))*(XL(i)*XL(i)*ZL(i)))+(C(19,3)-(xnL(i)*C(19,4)))*(YL(i)*YL(i)*ZL(i)))+(C(20,3)-(xnL(i)*C(20,4)))*(ZL(i)*ZL(i)*ZL(i));
F3(i) = ((C(2,5)-(ynR(i)*C(2,6)))*(XR(i)))+(C(3,5)-(ynR(i)*C(3,6)))*(YR(i)))+(C(4,5)-(ynR(i)*C(4,6)))*(ZR(i)))+(C(5,5)-(ynR(i)*C(5,6)))*(XR(i)*YR(i)))+(C(6,5)-(ynR(i)*C(6,6)))*(XR(i)*ZR(i)))+(C(7,5)-(ynR(i)*C(7,6)))*(YR(i)*ZR(i)))+(C(8,5)-(ynR(i)*C(8,6)))*(XR(i)*XR(i)))+(C(9,5)-(ynR(i)*C(9,6)))*(YR(i)*YR(i)))+(C(10,5)-
```

```

(ynR(i)*C(10,6))* (ZR(i)*ZR(i)))+( (C(11,5)-(ynR(i)*C(11,6)))*(XR(i)*YR(i)*ZR(i)))+( (C(12,5)-
(ynR(i)*C(12,6)))*(XR(i)*XR(i)*XR(i)))+( (C(13,5)-
(ynR(i)*C(13,6)))*(XR(i)*YR(i)*YR(i)))+( (C(14,5)-
(ynR(i)*C(14,6)))*(XR(i)*ZR(i)*ZR(i)))+( (C(15,5)-
(ynR(i)*C(15,6)))*(YR(i)*XR(i)*XR(i)))+( (C(16,5)-
(ynR(i)*C(16,6)))*(YR(i)*YR(i)*YR(i)))+( (C(17,5)-
(ynR(i)*C(17,6)))*(YR(i)*ZR(i)*ZR(i)))+( (C(18,5)-
(ynR(i)*C(18,6)))*(XR(i)*XR(i)*ZR(i)))+( (C(19,5)-
(ynR(i)*C(19,6)))*(YR(i)*YR(i)*ZR(i)))+( (C(20,5)-(ynR(i)*C(20,6)))*(ZR(i)*ZR(i)*ZR(i)));
F4(i) = ((C(2,7)-(xnR(i)*C(2,8)))*(XR(i)))+( (C(3,7)-(xnR(i)*C(3,8)))*(YR(i)))+( (C(4,7)-
(xnR(i)*C(4,8)))*(ZR(i)))+( (C(5,7)-(xnR(i)*C(5,8)))*(XR(i)*YR(i)))+( (C(6,7)-
(xnR(i)*C(6,8)))*(XR(i)*ZR(i)))+( (C(7,7)-(xnR(i)*C(7,8)))*(YR(i)*ZR(i)))+( (C(8,7)-
(xnR(i)*C(8,8)))*(XR(i)*XR(i)))+( (C(9,7)-(xnR(i)*C(9,8)))*(YR(i)*YR(i)))+( (C(10,7)-
(xnR(i)*C(10,8)))*(ZR(i)*ZR(i)))+( (C(11,7)-(xnR(i)*C(11,8)))*(XR(i)*YR(i)*ZR(i)))+( (C(12,7)-
(xnR(i)*C(12,8)))*(XR(i)*XR(i)*XR(i)))+( (C(13,7)-
(xnR(i)*C(13,8)))*(XR(i)*YR(i)*YR(i)))+( (C(14,7)-
(xnR(i)*C(14,8)))*(XR(i)*ZR(i)*ZR(i)))+( (C(15,7)-
(xnR(i)*C(15,8)))*(YR(i)*XR(i)*XR(i)))+( (C(16,7)-
(xnR(i)*C(16,8)))*(YR(i)*YR(i)*YR(i)))+( (C(17,7)-
(xnR(i)*C(17,8)))*(YR(i)*ZR(i)*ZR(i)))+( (C(18,7)-
(xnR(i)*C(18,8)))*(XR(i)*XR(i)*ZR(i)))+( (C(19,7)-
(xnR(i)*C(19,8)))*(YR(i)*YR(i)*ZR(i)))+( (C(20,7)-(xnR(i)*C(20,8)))*(ZR(i)*ZR(i)*ZR(i)));
end
for i = 1 : N;
% PARTIAL DERIVATIVES F1,F2, F3, F4 W.R.T. X, Y, Z
F1_X(i) = ((C(2,1)-(ynL(i))*C(2,2)))+( ((C(5,1)-(ynL(i))*C(5,2)))*(YL(i)))+( ((C(6,1)-
(ynL(i))*C(6,2)))*(ZL(i)))+( (2*(C(8,1)-(ynL(i))*C(8,2)))*(XL(i)))+( ((C(11,1)-
(ynL(i))*C(11,2)))*(YL(i)*ZL(i)))+( (3*(C(12,1)-
(ynL(i))*C(12,2)))*(XL(i)*XL(i)))+( ((C(13,1)-
(ynL(i))*C(13,2)))*(YL(i)*YL(i)))+( ((C(14,1)-
(ynL(i))*C(14,2)))*(ZL(i)*ZL(i)))+( (2*(C(15,1)-
(ynL(i))*C(15,2)))*(XL(i)*YL(i)))+( (2*(C(18,1)-(ynL(i))*C(18,2)))*(XL(i)*ZL(i)));
F1_Y(i) = ((C(3,1)-(ynL(i))*C(3,2)))+( ((C(5,1)-(ynL(i))*C(5,2)))*(XL(i)))+( ((C(7,1)-
(ynL(i))*C(7,2)))*(ZL(i)))+( (2*(C(9,1)-(ynL(i))*C(9,2)))*(YL(i)))+( ((C(11,1)-
(ynL(i))*C(11,2)))*(XL(i)*ZL(i)))+( (2*(C(13,1)-
(ynL(i))*C(13,2)))*(XL(i)*YL(i)))+( ((C(15,1)-
(ynL(i))*C(15,2)))*(XL(i)*XL(i)))+( (3*(C(16,1)-
(ynL(i))*C(16,2)))*(YL(i)*YL(i)))+( ((C(17,1)-
(ynL(i))*C(17,2)))*(ZL(i)*ZL(i)))+( (2*(C(19,1)-(ynL(i))*C(19,2)))*(YL(i)*ZL(i)));
F1_Z(i) = ((C(4,1)-(ynL(i))*C(4,2)))+( ((C(6,1)-(ynL(i))*C(6,2)))*(XL(i)))+( ((C(7,1)-
(ynL(i))*C(7,2)))*(YL(i)))+( (2*(C(10,1)-(ynL(i))*C(10,2)))*(ZL(i)))+( ((C(11,1)-
(ynL(i))*C(11,2)))*(XL(i)*YL(i)))+( (2*(C(14,1)-
(ynL(i))*C(14,2)))*(XL(i)*ZL(i)))+( (2*(C(17,1)-
(ynL(i))*C(17,2)))*(YL(i)*ZL(i)))+( ((C(18,1)-
(ynL(i))*C(18,2)))*(XL(i)*XL(i)))+( ((C(19,1)-
(ynL(i))*C(19,2)))*(YL(i)*YL(i)))+( (3*(C(20,1)-(ynL(i))*C(20,2)))*(ZL(i)*ZL(i)));
F2_X(i) = ((C(2,3)-(xnL(i))*C(2,4)))+( ((C(5,3)-(xnL(i))*C(5,4)))*(YL(i)))+( ((C(6,3)-
(xnL(i))*C(6,4)))*(ZL(i)))+( (2*(C(8,3)-(xnL(i))*C(8,4)))*(XL(i)))+( ((C(11,3)-
(xnL(i))*C(11,4)))*(YL(i)*ZL(i)))+( (3*(C(12,3)-
(xnL(i))*C(12,4)))*(XL(i)*XL(i)))+( ((C(13,3)-
(xnL(i))*C(13,4)))*(YL(i)*YL(i)))+( ((C(14,3)-
(xnL(i))*C(14,4)))*(ZL(i)*ZL(i)))+( (2*(C(15,3)-
(xnL(i))*C(15,4)))*(XL(i)*YL(i)))+( (2*(C(18,3)-(xnL(i))*C(18,4)))*(XL(i)*ZL(i)));
F2_Y(i) = ((C(3,3)-(xnL(i))*C(3,4)))+( ((C(5,3)-(xnL(i))*C(5,4)))*(XL(i)))+( ((C(7,3)-
(xnL(i))*C(7,4)))*(ZL(i)))+( (2*(C(9,3)-(xnL(i))*C(9,4)))*(YL(i)))+( ((C(11,3)-
(xnL(i))*C(11,4)))*(XL(i)*ZL(i)))+( (2*(C(13,3)-
(xnL(i))*C(13,4)))*(XL(i)*YL(i)))+( ((C(15,3)-
(xnL(i))*C(15,4)))*(XL(i)*XL(i)))+( (3*(C(16,3)-
(xnL(i))*C(16,4)))*(YL(i)*YL(i)))+( ((C(17,3)-
(xnL(i))*C(17,4)))*(ZL(i)*ZL(i)))+( (2*(C(19,3)-(xnL(i))*C(19,4)))*(YL(i)*ZL(i)));
F2_Z(i) = ((C(4,3)-(xnL(i))*C(4,4)))+( ((C(6,3)-(xnL(i))*C(6,4)))*(XL(i)))+( ((C(7,3)-
(xnL(i))*C(7,4)))*(YL(i)))+( (2*(C(10,3)-(xnL(i))*C(10,4)))*(ZL(i)))+( ((C(11,3)-
(xnL(i))*C(11,4)))*(XL(i)*YL(i)))+( (2*(C(14,3)-
(xnL(i))*C(14,4)))*(XL(i)*ZL(i)))+( (2*(C(17,3)-
(xnL(i))*C(17,4)))*(YL(i)*ZL(i)))+( ((C(18,3)-
(xnL(i))*C(18,4)))*(XL(i)*XL(i)))+( ((C(19,3)-
(xnL(i))*C(19,4)))*(YL(i)*YL(i)))+( (3*(C(20,3)-(xnL(i))*C(20,4)))*(ZL(i)*ZL(i)));
F3_X(i) = ((C(2,5)-(ynR(i))*C(2,6)))+( ((C(5,5)-(ynR(i))*C(5,6)))*(YR(i)))+( ((C(6,5)-
(ynR(i))*C(6,6)))*(ZR(i)))+( (2*(C(8,5)-(ynR(i))*C(8,6)))*(XR(i)))+( ((C(11,5)-
(ynR(i))*C(11,6)))*(YR(i)*ZR(i)))+( (3*(C(12,5)-
(ynR(i))*C(12,6)))*(XR(i)*XR(i)))+( ((C(13,5)-

```

```

((ynR(i))*C(13,6))* (YR(i)*YR(i)))+( ((C(14,5)-
((ynR(i))*C(14,6))* (ZR(i)*ZR(i)))+( (2*(C(15,5)-
((ynR(i))*C(15,6))* (XR(i)*YR(i)))+( (2*(C(18,5)-((ynR(i))*C(18,6))* (XR(i)*ZR(i))));

F3_Y(i) = ((C(3,5)-((ynR(i))*C(3,6)))+( ((C(5,5)-((ynR(i))*C(5,6)))* (XR(i)))+( ((C(7,5)-
((ynR(i))*C(7,6)))* (ZR(i)))+( (2*(C(9,5)-((ynR(i))*C(9,6))* (YR(i)))+( ((C(11,5)-
((ynR(i))*C(11,6))* (XR(i)*ZR(i)))+( (2*(C(13,5)-
((ynR(i))*C(13,6))* (XR(i)*YR(i)))+( ((C(15,5)-
((ynR(i))*C(15,6))* (XR(i)*XR(i)))+( (3*(C(16,5)-
((ynR(i))*C(16,6))* (YR(i)*YR(i)))+( ((C(17,5)-
((ynR(i))*C(17,6))* (ZR(i)*ZR(i)))+( (2*(C(19,5)-((ynR(i))*C(19,6))* (YR(i)*ZR(i))));
F3_Z(i) = ((C(4,5)-((ynR(i))*C(4,6)))+( ((C(6,5)-((ynR(i))*C(6,6))* (XR(i)))+( ((C(7,5)-
((ynR(i))*C(7,6)))* (YR(i)))+( (2*(C(10,5)-((ynR(i))*C(10,6))* (ZR(i)))+( ((C(11,5)-
((ynR(i))*C(11,6))* (XR(i)*YR(i)))+( (2*(C(14,5)-
((ynR(i))*C(14,6))* (XR(i)*ZR(i)))+( (2*(C(17,5)-
((ynR(i))*C(17,6))* (YR(i)*ZR(i)))+( ((C(18,5)-
((ynR(i))*C(18,6))* (XR(i)*XR(i)))+( ((C(19,5)-
((ynR(i))*C(19,6))* (YR(i)*YR(i)))+( (3*(C(20,5)-((ynR(i))*C(20,6))* (ZR(i)*ZR(i))));
F4_X(i) = ((C(2,7)-((xnR(i))*C(2,8)))+( ((C(5,7)-((xnR(i))*C(5,8))* (YR(i)))+( ((C(6,7)-
((xnR(i))*C(6,8))* (ZR(i)))+( (2*(C(8,7)-((xnR(i))*C(8,8))* (XR(i)))+( ((C(11,7)-
((xnR(i))*C(11,8))* (YR(i)*ZR(i)))+( (3*(C(12,7)-
((xnR(i))*C(12,8))* (XR(i)*XR(i)))+( ((C(13,7)-
((xnR(i))*C(13,8))* (YR(i)*YR(i)))+( ((C(14,7)-
((xnR(i))*C(14,8))* (ZR(i)*ZR(i)))+( (2*(C(15,7)-
((xnR(i))*C(15,8))* (XR(i)*YR(i)))+( (2*(C(18,7)-((xnR(i))*C(18,8))* (XR(i)*ZR(i))));
F4_Y(i) = ((C(3,7)-((xnR(i))*C(3,8)))+( ((C(5,7)-((xnR(i))*C(5,8))* (XR(i)))+( ((C(7,7)-
((xnR(i))*C(7,8))* (ZR(i)))+( (2*(C(9,7)-((xnR(i))*C(9,8))* (YR(i)))+( ((C(11,7)-
((xnR(i))*C(11,8))* (XR(i)*ZR(i)))+( (2*(C(13,7)-
((xnR(i))*C(13,8))* (XR(i)*YR(i)))+( ((C(15,7)-
((xnR(i))*C(15,8))* (XR(i)*XR(i)))+( (3*(C(16,7)-
((xnR(i))*C(16,8))* (YR(i)*YR(i)))+( ((C(17,7)-
((xnR(i))*C(17,8))* (ZR(i)*ZR(i)))+( (2*(C(19,7)-((xnR(i))*C(19,8))* (YR(i)*ZR(i))));
F4_Z(i) = ((C(4,7)-((xnR(i))*C(4,8)))+( ((C(6,7)-((xnR(i))*C(6,8))* (XR(i)))+( ((C(7,7)-
((xnR(i))*C(7,8))* (YR(i)))+( (2*(C(10,7)-((xnR(i))*C(10,8))* (ZR(i)))+( ((C(11,7)-
((xnR(i))*C(11,8))* (XR(i)*YR(i)))+( (2*(C(14,7)-
((xnR(i))*C(14,8))* (XR(i)*ZR(i)))+( (2*(C(17,7)-
((xnR(i))*C(17,8))* (YR(i)*ZR(i)))+( ((C(18,7)-
((xnR(i))*C(18,8))* (XR(i)*XR(i)))+( ((C(19,7)-
((xnR(i))*C(19,8))* (YR(i)*YR(i)))+( (3*(C(20,7)-((xnR(i))*C(20,8))* (ZR(i)*ZR(i))));
end
% STRUCTURE OF B MATRIX (JACOBIAN MATRIX)
r = 4*N-3*N;
B = zeros(4*N,3*N);
K = zeros(4*N,1);
a = 1;
for i = 1 : 4 : 4*N
    a = a;
    B(i:i+3,i:i+2) = [F1_X(a) F1_Y(a) F1_Z(a);
                      F2_X(a) F2_Y(a) F2_Z(a);
                      F3_X(a) F3_Y(a) F3_Z(a);
                      F4_X(a) F4_Y(a) F4_Z(a)];
    K(i:i+3,1) = [(ynL(a)-C(1,1))-F1(a);
                  (xnL(a)-C(1,3))-F2(a);
                  (ynR(a)-C(1,5))-F3(a);
                  (xnR(a)-C(1,7))-F4(a)];
    a = a+1;
end
f = 4 : 4 : (4*N - 1);
B(:,f) = [];
K(:,1+(4*N):4:4) = [];
DX = (inv(B'*B))*(B'*K);
Vs = B*DX - K;
dx = DX(1:3:end);
dy = DX(2:3:end);
dz = DX(3:3:end);
dxyz = [dx dy dz];
% ENHANCED COORDINATES
for i = 1 : N;

```

```

X_GPS(i) = Obs(i,2);
Y_GPS(i) = Obs(i,3);
Z_GPS(i) = Obs(i,4);
XL_Enh(i)= XL(i)+dx(i);
YL_Enh(i)= YL(i)+dy(i);
ZL_Enh(i)= ZL(i)+dz(i);
XR_Enh(i)= XR(i)+dx(i);
YR_Enh(i)= YR(i)+dy(i);
ZR_Enh(i)= ZR(i)+dz(i);
XL_act(i)=(XL_Enh(i)*(long_scaL))+long_offL;
YL_act(i)=(YL_Enh(i)*(lat_scaL))+lat_offL;
ZL_act(i)=(ZL_Enh(i)*(H_scaL))+H_offL;
XR_act(i)=(XR_Enh(i)*(long_scaR))+long_offR;
YR_act(i)=(YR_Enh(i)*(lat_scaR))+lat_offR;
ZR_act(i)=(ZR_Enh(i)*(H_scaR))+H_offR;
X_act(i)= (XL_act(i) + XR_act(i))/2;
Y_act(i)= (YL_act(i) + YR_act(i))/2;
Z_act(i)= (ZL_act(i) + ZR_act(i))/2;
residual_X(i) = (X_GPS(i)-X_act(i));
residual_Y(i) = (Y_GPS(i)-Y_act(i));
residual_Z(i) = (Z_GPS(i)-Z_act(i));
end
X_Ref = X_act';
Y_Ref = Y_act';
Z_Ref = Z_act';
XYZ = [X_Ref Y_Ref Z_Ref];
rX = residual_X';
rY = residual_Y';
rZ = residual_Z';
residuals = [rX rY rZ];
RMSE_X = (sqrt(sum(rX'*rX)/N))*60*60*30;
RMSE_Y = (sqrt(sum(rY'*rY)/N))*60*60*30;
RMSE_Z = sqrt(sum(rZ'*rZ)/N);
RMSE_XYZ = [RMSE_X RMSE_Y RMSE_Z]
figure;
plot(Z_GPS','r+');hold on;
plot(Z_Ref,'b+');hold on;
xlabel 'GCPs', ylabel 'Elevation in (meters)';
legend('true value','Bias');
sX = std(rX)*60*60*30;
sY = std(rY)*60*60*30;
sZ = std(rZ);
stan_de = [sX sY sZ];
X_G = X_GPS'*60*60*30;
Y_G = Y_GPS'*60*60*30;
figure;
quiver(X_G,Y_G,(rX*60*60*30),(rY*60*60*30),'b','LineWidth',1,'AutoScaleFactor',1);
hold on; plot(X_G, Y_G,'ro');hold off;
xlabel 'X-Coordinate (meters)', ylabel 'Y-Coordinate (meters)';
legend('Bias','true value');

```

Table (C-1) Results of the Positioning Accuracy Based on the Three Approaches with Two Bias Correction Models for the IKONOS-2 Case

Scheme	Bias-Correction Models	No. of GCPs/ChkPs	RMS Value of ChkPs Differences on the Ground (Meters)		
			ΔX	ΔY	ΔZ
Direct	None	0/21	7.2	3.1	16.7
Bias-Corrected RPCs	Shift and Scale	5/16	1.2	1.4	1.4
		7/14	0.6	1.3	1.6
		9/12	0.7	1.4	1.7
		13/8	0.2	1.3	1.3
		15/6	0.2	1.1	1.2
		17/4	0.2	1.1	0.9
	First Order	9/12	3.3	1.7	2.0
		13/8	0.9	1.5	1.4
		15/6	0.9	3.1	2.1
		17/4	0.5	2.2	1.8
Bias-Corrected Image Space	Shift and Scale	3/18	2.4	1.0	1.2
		5/16	0.9	1.0	1.6
		7/14	0.9	0.9	1.7
		9/12	1.0	1.0	1.8
		13/8	0.3	1.0	1.5
		15/6	0.3	0.6	1.5
		17/4	0.3	0.6	1.2
	First Order	5/16	0.8	1.2	1.3
		7/14	0.8	1.1	1.5
		9/12	0.8	1.2	1.6
		13/8	0.2	1.2	1.2
		15/6	0.2	1.0	1.2
		17/4	0.2	0.9	0.9
Bias-Corrected Object Space	Shift and Scale	3/18	1.9	1.0	4.3
		5/16	1.8	1.2	3.3
		7/14	1.6	1.1	2.7
		9/12	1.7	1.2	1.9
		13/8	1.5	1.2	2.0
		15/6	1.4	0.9	2.1
		17/4	1.2	0.9	2.0
	First Order	5/16	0.9	1.3	1.5
		7/14	0.7	1.1	1.5
		9/12	0.8	1.2	1.7
		13/8	0.5	1.2	1.2
		15/6	0.4	1.0	1.2
		17/4	0.2	0.9	0.9

Table (C-2) Results of the Positioning Accuracy Based on the Three Approaches with Two Bias Correction Models for the GeoEye-1 Case

Scheme	Bias-Correction Models	No. of GCPs/ChkPs	RMS Value of ChkPs Differences on the Ground (Meters)		
			ΔX	ΔY	ΔZ
Direct	None	0/12	1.2	2.7	1.6
Bias-Corrected RPCs	Shift and Scale	5/7	0.3	0.4	0.3
		7/5	0.3	0.4	0.1
	First Order	5/7	0.1	0.2	0.2
		7/5	0.2	0.2	0.5
Bias-Corrected Image Space	Shift and Scale	3/9	0.5	0.4	0.7
		5/7	0.4	0.3	0.4
		7/5	0.5	0.4	0.3
		9/3	0.1	0.2	0.2
	First Order	5/7	0.3	0.3	0.6
		7/5	0.3	0.4	0.3
Bias-Corrected Object Space	Shift and Scale	9/3	0.2	0.2	0.3
	Shift and Scale	3/9	0.5	0.4	0.9
		5/7	0.5	0.3	0.5
		7/5	0.5	0.4	0.3
		9/3	0.2	0.2	0.2
	First Order	7/5	0.3	0.2	0.3
		9/3	0.1	0.2	0.4